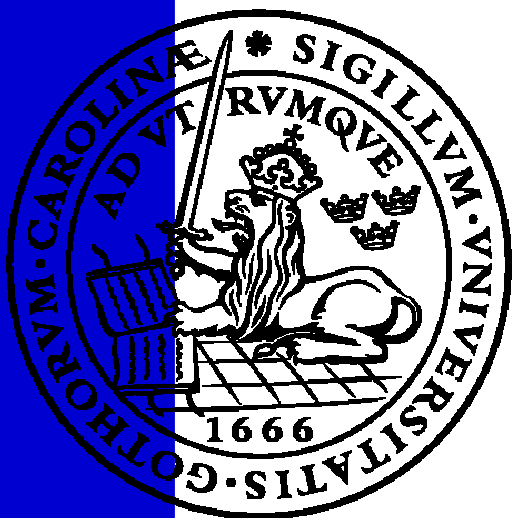


The Mirror Nuclei ^{61}Ga and ^{61}Zn

Lise-Lotte Andersson

Licentiate Thesis
2006



Department of Physics
Division of Nuclear Physics
Lund University
LUNFD6/(NFFR-3100)/1-69/(2006)

Contents

Introduction	3
1 Experimental Details	5
1.1 Fusion Evaporation Reactions	6
1.2 γ Detection	6
1.2.1 CLARION	6
1.2.2 GAMMASPHERE	7
1.3 Neutron Detection	8
1.4 Charged Particle Detection	8
1.4.1 LuWUSiA	8
1.4.2 Microball	9
1.5 Recoil Separators	10
1.5.1 Recoil Mass Separator	10
1.5.2 Fragment Mass Analyser	11
1.6 Ionisation Chamber	11
2 Data Handling	13
2.1 Data Format	13
2.2 Handling of the γ rays	15
2.3 Neutron Handling	15
2.3.1 Neutron- γ Separation	16
2.3.2 Two-Neutron Event Suppression	16
2.3.3 Neutron Identification Efficiency	18
2.4 Charged Particle Handling	19
2.4.1 Proton - α Separation	19
2.5 A/Q Separation	20
2.6 Ion Chamber Calibrations	20
3 Data Analysis	25
3.1 Recoil - γ Analysis	25
3.2 Recoil - $\gamma\gamma$ Analysis	26
3.3 The ^{61}Ga Nucleus	26
3.4 The ^{61}Zn Nucleus	26
3.4.1 Specific Transitions	30
3.4.2 Superdeformed Band	37
3.5 Angular Distribution Corrections	38

4	Theoretical Background	41
4.1	The Shell Model	41
4.1.1	Electromagnetic Transitions	44
4.1.2	Two-state Mixing	46
4.2	Shell-Model Calculations Using the Code ANTOINE	46
4.2.1	The GXPF1 and GXPF1A Interactions	47
4.2.2	The “ $f_{5/2}pg_{9/2}$ ” Interaction	47
4.2.3	The KB3G Interaction	47
4.3	Mirror Nuclei	48
5	Interpretation	51
5.1	The Shell Model Calculations	51
5.1.1	The ^{61}Zn Nucleus	51
5.1.2	The ^{61}Ga Nucleus	55
5.2	Electromagnetic Decay Properties	55
5.3	Mirror Energy Differences	60
5.4	Prompt Proton Decay	62
6	Conclusions and Outlook	63
	Acknowledgements	65
	References	67

Introduction

Even though the thought of the atom was already founded some 400 years before the birth of Christ it took a long time before the structure of the atom, and hence also the existence of the nucleus, was revealed. The electron was first discovered in 1874 and not until 1897 it was found by Joseph John Thomson that the electron in fact was a subatomic particle. Around the same time Wilhelm Conrad Röntgen discovered the phenomenon of X-rays. Both discoveries indicated for the first time an internal structure of the, up to then indivisible, atom. As the English gentleman J. J. Thomson was he explained the phenomenon by comparing with something he could relate to – a plum pudding. The plum pudding model, founded in 1904, describes the atom as a “pudding” of positive charge in which the electrons are placed, much like the raisins in the traditional Christmas desert.

Another hint of subatomic structure came from Paris, where Antoine Henri Becquerel, together with Marie and Pierre Curie was working on another type of radiation. Eventually this radiation was identified as spontaneous radioactivity.

This means that in the start of the 20th century – just over 100 years ago – nothing was yet known about atomic nuclei. In fact it would take another ten years before Ernest Rutherford concluded his famous gold foil experiment. The conclusion was that instead of the positively charged pudding the atom must contain a very small dense object with positive charge at the centre of the atom. This model was further developed by Niels Bohr a few years later to include specific orbits – or energy states – of the electrons.

So in 1911 the atomic nucleus was born. The idea was that the positively charged nucleus would balance with, or cancel out, the negatively charged electrons so that the total charge was zero. Simultaneously the number of protons and hence also electrons could vary to compose different kinds of atoms. This model was accepted and lived to the 1930's. However, in 1932 neutron radiation was found by Walther Bothe, Herbert Becker, and Irène (Marie and Pierre Curie's daughter) and Frédéric Joliot-Curie. In the same year it was suggested that the nucleus in fact consisted of both protons and neutrons. Two years later Hideki Yukawa presented the idea of the strong force to explain how the nucleus is held together in spite of the repulsive Coulomb force between the protons.

The work on induced radioactivity from Irène and Frédéric Joliot-Curie was continued by Lise Meitner, Robert Otto Frisch and Otto Hahn during the late 1930's. In 1938 this research led to the discovery of nuclear fission. Early it was understood that this reaction could lead to the release of large amounts of energy – for better and for worse. This led to the start of the Manhattan project to build a nuclear bomb in the U. S. The laboratory in Oak Ridge, Tennessee, was actually built in the course of

this project to produce the specific nuclear material for the bombs. Around the same time, in 1942, the first self-sustaining nuclear reaction was accomplished providing the possibility of producing nuclear power. A number of people was involved in this project, among others Enrico Fermi, Leona Woods Marshall Libby, and Leo Szilard. Many of them were also involved in the Manhattan project.

In 1948 a new contribution to the structure of atomic nuclei was added when Maria Göppert-Mayer (and later also J. Hans D. Jensen) suggested the nuclear shell model, in which the nucleons are arranged into specific energy states much like the electrons in the atom. Maria Göppert-Mayer also introduced the much important concept of spin-orbit coupling, which made it possible to reproduce the shell structure as seen experimentally.

The introduction of the shell model brought nuclear research to the modern model of the atomic nucleus. Everyday research in the Nuclear Structure Group at Lund University – and throughout the world – is to a large extent built on this model. Furthermore, research is still today working on identifying and explaining the energy states of different nuclei. For example, this thesis deals with the task of finding the level energies and explain the energy difference between the two nuclei ${}^{61}_{30}\text{Zn}_{31}$ and ${}^{61}_{31}\text{Ga}_{30}$. This research was started in the summer of 2003 when I became a Master student in the Nuclear Structure Group. My first experiment was carried out just a couple of weeks later at the Oak Ridge National Laboratory in Tennessee. Detailed information about the analysis of the ${}^{61}_{31}\text{Ga}_{30}$ nucleus can be found in my Master Thesis [1]. The fundamental facts are, however, also described in this licentiate thesis. One major conclusion from this experiment is a possible prompt proton decay in the ${}^{61}_{31}\text{Ga}_{30}$ nucleus. The analysis resulted in a paper published in Physical Review C in the course of my PhD studies and will in this thesis be referred to as “Paper I” [2]. The Oak Ridge data set was also used in the analysis of excited states in ${}^{61}_{30}\text{Zn}_{31}$.

Additional to the Oak Ridge experiment I am involved in the analysis of an experiment carried out at the Argonne National Laboratory, Illinois. The experiments shared similar set-ups (described in parallel in Chapter 1) but the Argonne experiment involved the locally developed charged particle detector; the Lund and Washington University Silicon Array, Lu-WU-SiA.

The handling of the Oak Ridge and Argonne data sets, especially the parts that I have been involved in, are described in Chapter 2. Chapter 3 on the other hand deals with the analysis of the Oak Ridge data set. Since the Argonne data is yet at the stage of data handling no analysis nor results will be reported from it. The analysis of ${}^{61}_{31}\text{Ga}_{30}$ is, as mentioned above reported in Ref. [1] and in Paper I. This means that Chapter 3 primarily involves details about the analysis of ${}^{61}_{30}\text{Zn}_{31}$. The results and interpretation of this analysis can be found in Chapter 5 and are also published in European Physical Journal A, which will be referred to as “Paper II” [3] in the following.

To interpret the experimental results naturally some theoretical knowledge is acquired, for example, about the above mentioned nuclear shell model. This model, and some theory behind the large-scale shell-model calculations that I have used in this analysis are presented in Chapter 4 to provide the reader with some necessary facts. Chapter 6 concerns conclusions from my analysis and an outlook of what is planned for the future.

Chapter 1

Experimental Details

Two different experiments will be presented in this chapter. One of them was conducted in August 2003 at the Oak Ridge National Laboratory (ORNL), Tennessee, U.S.A. The second experiment, from Argonne National Laboratory (ANL), Illinois, U.S.A was carried out in April 2004. The two experiments have a similar set-up and will be described in parallel.

Excited states in neutron-deficient nuclei are in both experiments produced in a so called fusion-evaporation reaction (Sec. 1.1). The γ rays, emitted at the target position, are detected in an array of germanium detectors (Sec. 1.2) placed around the target position. A set of auxiliary detectors were used around the target in the ANL experiment (Sec. 1.3 and Sec. 1.4). From the target chamber the recoiling nuclei will enter a separator, which parts the residues depending on their mass-to-charge ratio (Sec. 1.5). The final part in the experimental set-ups is an Ionisation Chamber which detects Z , the proton number of the recoils (Sec. 1.6). Below follows a short description of the two experiments.

Experimental description Oak Ridge

In the Oak Ridge experiment a ^{40}Ca beam at 104 MeV and a ^{24}Mg target foil was used to produce the compound nucleus ^{64}Ge . The target foil had a thickness of 0.3 mg/cm^2 and was to 99.92% isotropically enriched. The experimental setup comprised the Ge-detector Array CLARION (CLOver Array for Radioactive ION beams, Sec. 1.2.1) to detect γ rays emitted at the target position. The recoils then move through a Recoil Mass Separator (Sec. 1.5.1) and are finally deposited in an ionisation chamber (Sec. 1.6).

Experimental description Argonne

The target consisted of 0.2 mg/cm^2 ^{28}Si evaporated onto a 0.9 mg/cm^2 ^{181}Ta foil and the beam of ^{36}Ar at an energy of 142 MeV. The γ rays emitted from the residues are detected in Ge-detectors placed in the GAMMASPHERE (Sec. 1.2.2). In the set-up for this experiment 30 neutron detectors replaced the Ge-detectors in the most forward direction - forming the so-called Neutron Shell (Sec. 1.3). The Neutron Shell can detect neutrons emitted at the target position. The emitted charged particles can instead be detected using the charged particle detector array, Lu-Wu-SiA, (Sec. 1.4.1) from Lund University. This array and the two last rings of the Microball detector (Sec. 1.4.2) were placed around the target inside the target

chamber. To identify weak reaction channels the Fragment Mass Analyser, FMA, (Sec. 1.5.2), placed in close connection to GAMMASPHERE, was used. The residues which are produced at the target position will, after emitting the γ rays, move into this part of the detector system. At the end of the FMA is the focal plane and an ionisation chamber (Sec. 1.6).

1.1 Fusion Evaporation Reactions

The process of fusion evaporation is in principle quite simple, and is illustrated in Fig. 1.1. The beam nuclei hit the nuclei in the target foil with a large amount of energy. In this process the two nuclei can, with a large probability, fuse and form a so called compound nucleus. In both experiments this compound was a ^{64}Ge nucleus.

The compound nucleus is highly excited and therefore not very stable. By emitting – or evaporating – light particles such as α particles, protons, or neutrons, the nucleus will lose a lot of its energy. When the residue is not energetic enough to emit more particles it will instead continue by sending out γ rays before finally ending up in its ground state. The process is very fast; within 10^{-9} seconds the particles and light quanta have been emitted and the residual nucleus has reached its ground state. The species of the residue – or recoiling nuclei – naturally depends on the number and type of evaporated particles. This in turn depends on the energy of the system and on the proton and neutron number of the selected target and beam nuclei.

When talking about fusion evaporation reactions one often uses the word “channel” as referring to a certain combination of evaporated particles. For example, from the compound nucleus $^{64}_{32}\text{Ge}_{32}$, the residual nuclei $^{61}_{29}\text{Cu}_{32}$, $^{61}_{30}\text{Zn}_{31}$, and $^{61}_{31}\text{Ga}_{30}$ are formed via the so called $3p$, $2p1n$, and $1p2n$ channel, respectively.

1.2 γ Detection

The emitted γ rays are detected by high-purity Ge detectors placed close to and around the target position. It is important to aim for an efficient detection for a wide spread of energies. Germanium detectors are chosen for their high energy resolution, although they are fairly expensive and have a somewhat bulky set-up when including the necessary cooling devices.

1.2.1 CLARION

The CLover Array for Radioactive IONS – CLARION – is the Germanium array at the Oak Ridge National Laboratory. The array consists of eleven Ge clover detectors placed in a three ring construction covering some 3π solid angle around the target position. The three rings are placed at 90° , 132° , and 154° relative to the beam axis. The nomination “clover” originates from the construction of four almost square Ge crystals forming a larger square shape. An advantage with this construction is the separate output signals from the four crystals resulting in a more refined Doppler correction, because the detection angle can be more precisely

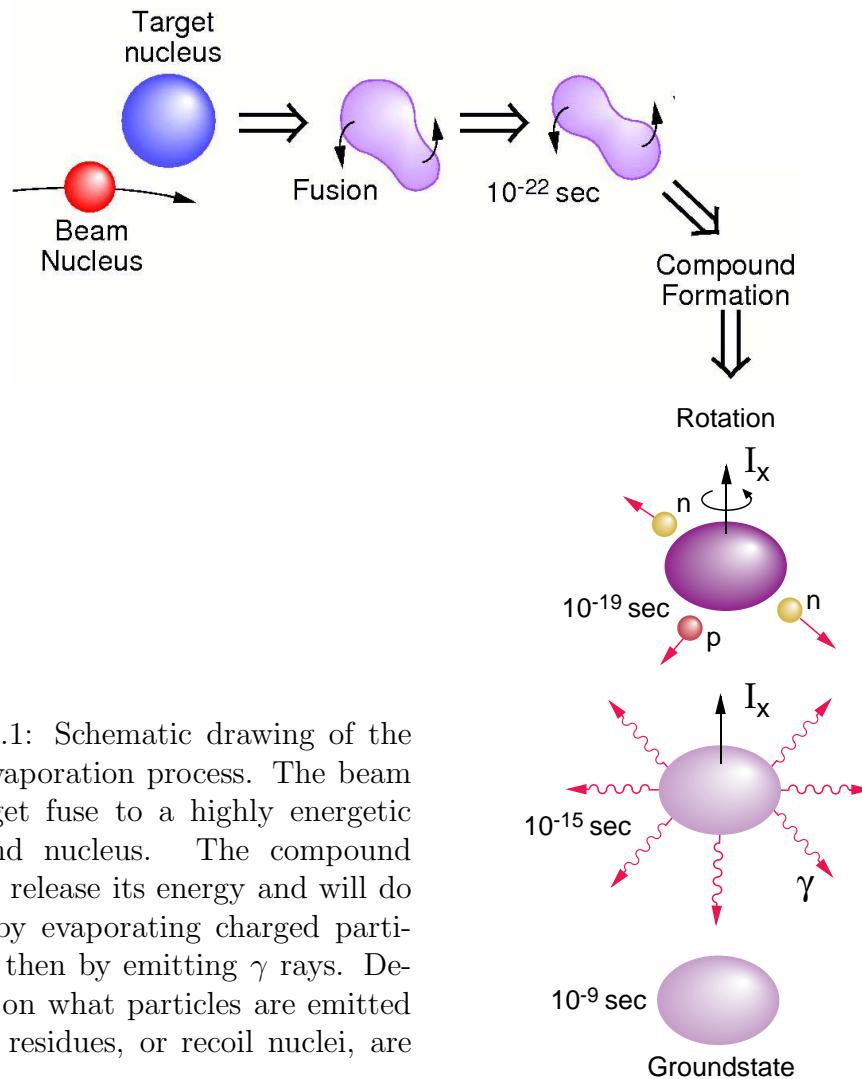


Figure 1.1: Schematic drawing of the fusion evaporation process. The beam and target fuse to a highly energetic compound nucleus. The compound wants to release its energy and will do so first by evaporating charged particles and then by emitting γ rays. Depending on what particles are emitted different residues, or recoil nuclei, are obtained.

determined. To further enhance the precision of determining the detection angle the clover detector is electrically segmented into three parts. Details about the construction of CLARION can be found in Refs. [4] and [5].

Each clover detector has a BGO shield. The BGO, or Bismuth-Germanate, provides the possibility of Compton suppression. Since a γ ray should leave all of its energy in the Ge crystal we want to reject the events in which the γ ray scatters out of the Ge detector. The BGO material is very dense and can therefore easily absorb such γ photons.

1.2.2 GAMMASPHERE

The γ detection device at ANL is called GAMMASPHERE [6]. It is a large array comprising up to 110 High-Purity Germanium (HP-Ge) detectors each of which is provided with a BGO shield for Compton suppression.

The Ge detectors in the array are, similarly to CLARION, placed in a 17 ring construction. The positions of the rings vary between 17.3° up to 162.7° and the number of detectors per ring is either five or ten. If using all the Ge detectors

a full 4π coverage is achieved. However, it is possible to replace up to 30 of the most forward Ge-BGO modules with neutron detectors. The neutron detectors will then replace the five most forward rings (angular position between 17.3° and 58.3°) leaving angle 69.8° and upward to be covered with Ge detectors. This exchange was done for the current experiment. Furthermore this set-up involved a removal of two more HP-Ge detectors to allow the cables from the charged particle detector Lu-WU-SiA to be extracted from the target chamber.

Finally one of the detectors was not working during the experiment resulting in totally 77 Ge detectors for the Argonne experiment.

1.3 Neutron Detection

The Neutron Shell [7] consists of 30 neutron detectors which replace an equal amount of Ge detectors at the five most forward rings in GAMMASPHERE, see Fig. 1.2. The neutron detectors are liquid scintillators with high neutron efficiency. The liquid scintillators also make it possible to distinguish between neutron and γ rays by using pulse-shape discrimination and time-of-flight.

When detecting neutrons in a liquid scintillator the neutron needs to transfer energy to a proton that can ionise and excite the scintillator material. The X rays emitted in the de-excitation can then be detected. Obviously γ rays can also cause excitations in the neutron detectors. To prevent low-energy γ rays from entering the detectors an 8 mm thick lead absorber is placed in front of the detector. The lead plate stops some, but not all, incidenting γ rays. An incoming γ ray will, however, transfer its energy via interactions with the electrons of the scintillator material. The different interaction processes, with different energy loss per unit length, result in different pulse shapes for neutrons and protons, respectively.

1.4 Charged Particle Detection

The charged particle detection at ANL is done with the Lu-Wu-SiA array. The construction of the array allows no particle detection at backward angles (i.e. angles $\geq 120^\circ$). Due to the reaction used for this experiment with heavier beam than target nuclei we do not expect a large fraction of the particles to be evaporated at the, in the laboratory frame, large backward angles. However, to detect the particles actually emitted in this direction two rings of the Microball detector were used [8].

1.4.1 LuWUSiA

Lu-Wu-SiA is an array of eight $\Delta E - E$ telescope Silicon detectors, each of which consists of a 16 strip $\sim 65 \mu\text{m}$ thin ΔE and a 32 strip $\sim 1 \text{ mm}$ thick E detector. In the E detector the strips are electronically coupled two by two. Furthermore, the strip segmentation is in one detector placed horizontally and in the other vertically. This will result in a 256 pixel segmentation for each telescope, i.e. 2048 pixels in total. The large pixellation will allow for determination of precise angular distributions of the emitted particles.

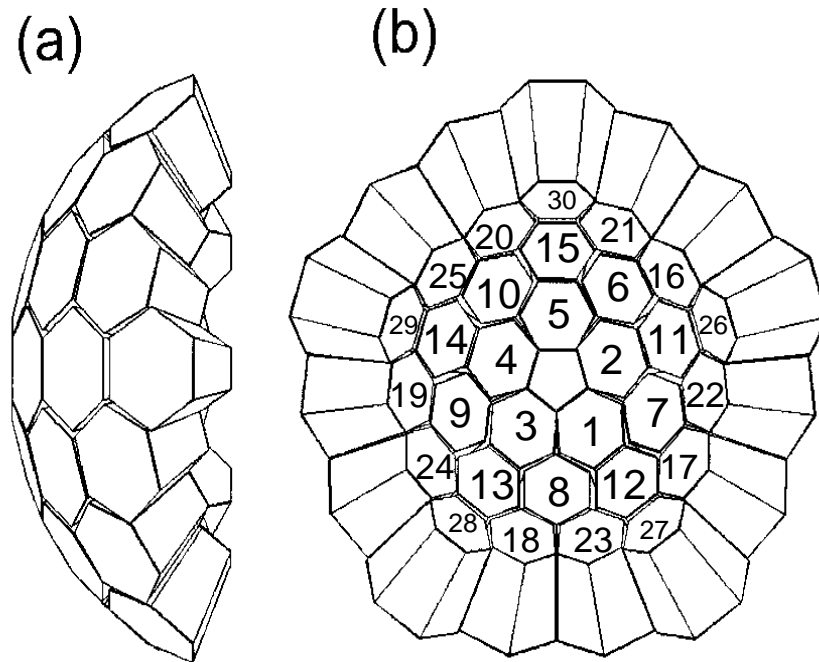


Figure 1.2: The Neutron Shell from the side (a) and from the target position (b). The position of the detectors as they are numbered in the data stream are marked out. The figure is taken from [9].

Lu-Wu-SiA detects both protons and α particles. The two are identified and eventually separated due to their different ionising power in the ΔE and the E detector, respectively.

Four of the eight telescopes are placed as a box around target, and four are placed as a wall at forward angles. This covers $\sim 3\pi$ of the solid angle around the target.

In Fig. 1.3 a sketch of the set-up is shown. The ΔE detectors of the box and wall are marked out in pink while the E detectors are marked in green. For more information about Lu-Wu-SiA see Ref. [10].

1.4.2 Microball

To detect charged particles emitted at very large backward angles the two “last” rings of Microball [8] are used. These are parted in eight sections each. The positions of the two rings are 135° and 159° .

Microball, which is an array of CsI(Tl) detectors, provides the possibility of pulse shape discrimination based on the fact that different particles have different ionising power, i.e. different dE/dx behaviour. In CsI(Tl) detectors the overall decay time of α -particles is $0.425 \mu\text{s}$, the corresponding number for protons is $0.519 \mu\text{s}$ [11]. Figure 1.4 illustrates the light output as a function of time. In the figure also the gates giving the energy signal and Particle IDentification (PID) signal are illustrated. More details about the identification and separation of α -particles and protons can be found in Sec. 2.4.

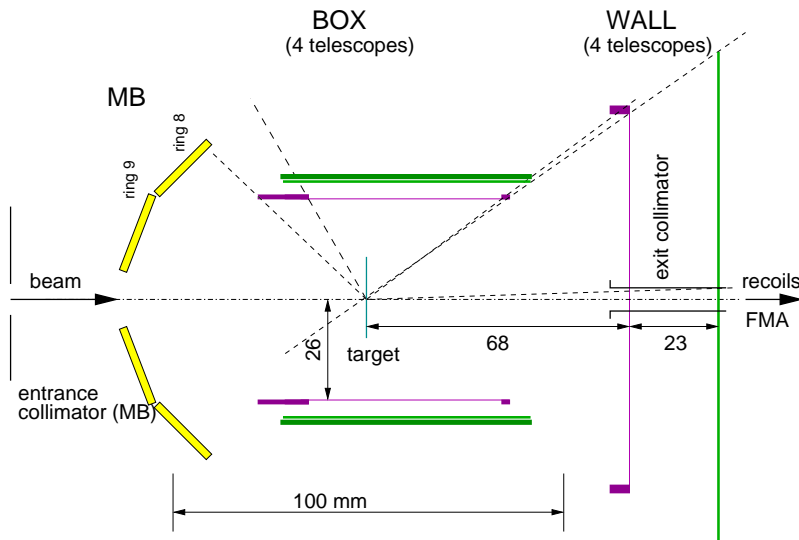


Figure 1.3: Schematic drawing of the set-up of charged particle detectors. The beam incidents from the left to hit the target at the very centre of the set-up. Placed around the target are four $\Delta E - E$ telescope Silicon detectors forming a “box”. In the forward angles are another four $\Delta E - E$ telescope Silicon detectors placed side by side like a “wall”. In the backward angles two rings of Microball are used.

1.5 Recoil Separators

1.5.1 Recoil Mass Separator

The Recoil Mass Separator, RMS, at the Oak Ridge National Laboratory is placed in close connection to the CLARION Ge array. The construction of the RMS allows first separation in momentum, P/Q , where Q denotes the charge state of the nucleus, i.e. the number of stripped electrons. This separation allows beam rejection. The recoils are then refocused followed by a new separation, this time according to their mass-to-charge ratio, A/Q . At the very end of the RMS is the Ionisation Chamber. The recoils be stopped in here and their relative horizontal position will be determined via a position sensitive grid.

The set-up with the RMS placed in close connection with CLARION is very convenient as it allows for correlations between γ rays detected in CLARION with the nucleus emitting the radiation. One problem, however, is the limited acceptance of the RMS. In order for the recoils to fly through the full length of the apparatus, and not get stuck on the way, certain restrictions are required in energy and mass-to-charge ratio. The limited acceptance is due to the strength of the magnetic and electric fields which will steer the recoils too much, or too little, depending on the velocity and charge of the nuclei. The A/Q can vary $\pm 4.9\%$ and the energy may vary $\pm 10\%$. In addition, the angular acceptance is 30 mrad in the horizontal and 110 mrad in the vertical direction [5].

The construction of the RMS can be seen in panel (a) of Fig. 1.5. Here D denotes the magnetic dipoles, Q the quadrupoles, S the sextupoles, and E the electrostatic

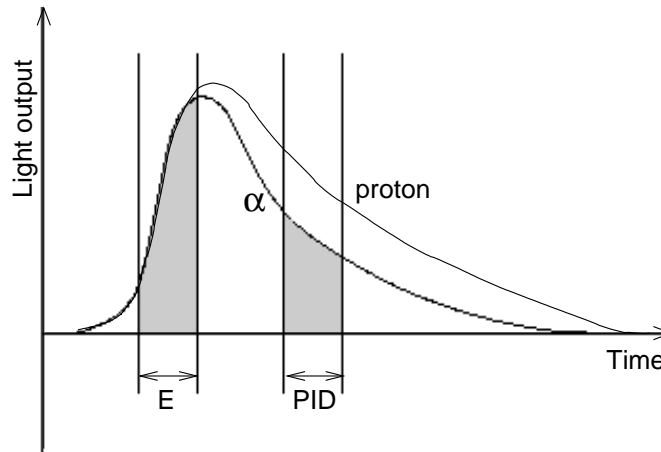


Figure 1.4: Schematic drawing of pulse shapes of protons and α particles in the CsI(Tl) elements in Microball. Particle IDentification, PID, and Energy, E, signals from the data stream are illustrated.

dipoles. More information about the RMS can be found in Ref. [1].

1.5.2 Fragment Mass Analyser

The Fragment Mass Analyser, FMA, has a similar construction as the RMS, as can be seen in panel (b) of Fig. 1.5. In the figure the FMA starts behind the target (TGT), then follow magnetic quadrupoles (Q), electrostatic dipoles (ED), and a magnetic dipole (MD), positioned according to Fig. 1.5. Finally the recoils hit the detector at the end (DET). This detector is the ionisation chamber which is preceded by the focal plane where a multi-wired proportional counter, PPAC, is placed. The PPAC gives an X and a Y position for the particles which pass through it. The position information is found by using a delay line. When hitting the PPAC the particle will generate four electrical signals. These define different directions; up/down and left/right. The time difference between receiving the signals will give the position information. The PPAC also provides an energy loss signal, which will give information about the recoils in the same manner as the energy loss signals in the Ionisation Chamber.

Also the FMA is limited in acceptance. The A/Q value may here vary with $\pm 3.5\%$ and the energy with $\pm 20\%$. The angular acceptance is 45 mrad in both horizontal and vertical direction [12].

1.6 Ionisation Chamber

An Ionisation Chamber (IC) is used in both experimental set-ups and works very similar in both experiments.

The IC is placed at the very end of the FMA and the RMS. It is used for identification of the incidenting recoils. To identify them we take advantage of the fact that the anode inside the IC is split into three sections. In the case of the Argonne (Oak Ridge) experiment the sections are 50 (50), 50 (50) and 20 (202) mm

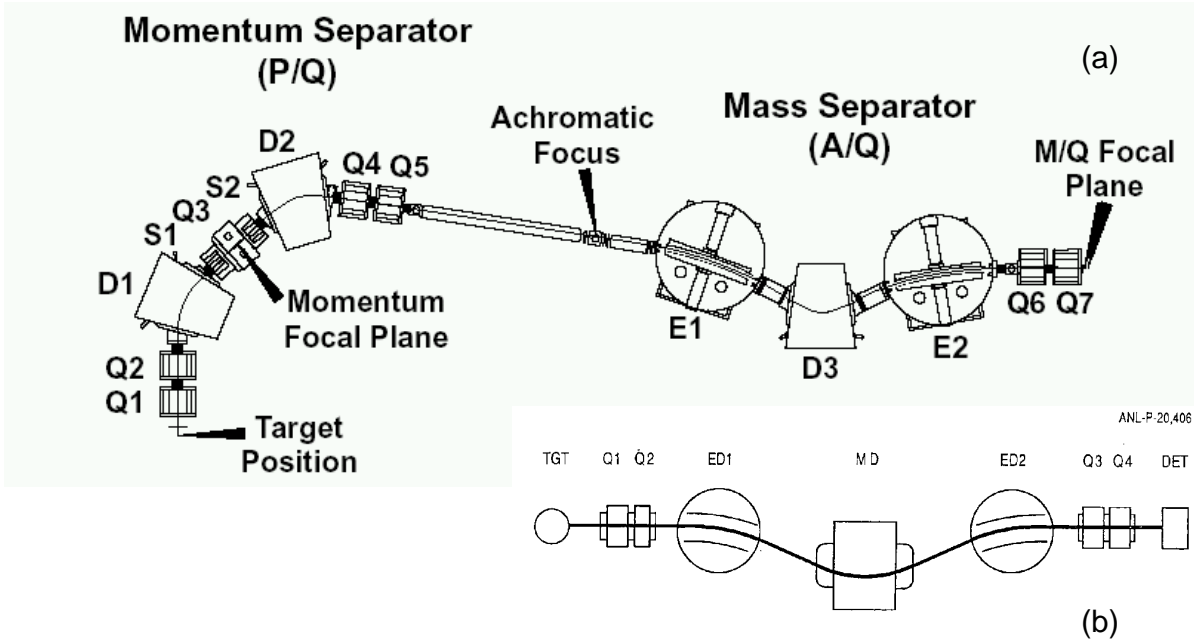


Figure 1.5: Schematic view of the RMS (a) and the FMA (b). The RMS consists of two parts, the first part separates the recoils in momentum-to-charge ratio and the second part separates in mass-to-charge ratio. In the case of the FMA only separation in mass-to-charge ratio takes place. As can be seen the construction of the FMA and the last part of the RMS identical. See text for details. The figures are taken from Ref. [13, 14]

long, respectively. The segmentation makes it possible to identify the Z of the incoming recoil.

According to the Bethe-Bloch formula the energy loss is dependent on Z and inversely dependent on the energy of the recoils. The energy dependence can be corrected for (see Sec. 2.6) and the energy loss will hence then only depend on the number of protons in the nucleus. The energy loss in each section or a combination of more than one energy loss can then be used to identify the Z of the recoils.

In the case of the Oak Ridge set-up the A/Q position is measured inside the IC by a position sensitive grid. The position is derived via the time difference between receiving a signal on the left and right hand side of the IC. The method is very similar as for the case of the PPAC in the ANL set-up, described above.

Chapter 2

Data Handling

The data handling from the Oak Ridge experiment is described in great detail in Ref. [1] and Ref. [4]. Hence, I will instead concentrate on the analysis of the Argonne experiment in this chapter. In particular the parts that I have dealt with will be described.

2.1 Data Format

The data taken at the ANL is written in hexadecimal (hex) format. This means in words with four hex-digits in each. A section of the data stream is given in Fig. 2.1. The `ffff` word marks the separation of events and the following ten words marks the event header.

Here follows an example of how the header is structured:

The first word is in the form `80xx`. The number `xx` indicates the total number of words in the written event. In the example in Fig. 2.1 the number is `9c` which means $9 \cdot 16^1 + c \cdot 16^0 = 9 \cdot 16 + 12 \cdot 1 = 156$ words. This number includes the `80xx` and the event separator.

Second word: The two last digits give the number of “clean Ge” counts. Clean means that only the Ge detectors have fired and none of their surrounding BGOs. In this case we have three clean Ge hits.

Third word: The two first digits give the number of “dirty Ge”, i. e. the number of events with a signal from a Ge detector and simultaneously a signal from any of its surrounding BGOs. In this example there are no “dirty Ge”. The last two digits give the number of clean BGO, in this case seven hits.

The fourth to sixth word provides the trigger time.

The seventh and eighth word are connected to the time signals. One word is the time difference between the main trigger and the so called usec clock (the time scale of the latter depends on the trigger times). The other word is stopped by the radio frequency time.

The ninth word gives the sum of the low resolution Ge energies.

The tenth word gives the sum of BGO energies.

After the ten header words the data is written; first clean Ge events (six words each), then dirty Ge events (eight words each), followed by clean BGO events (three words each). The clean and dirty Ge include, for example, information about the

0354620	7eb1	ffff	809c	7003	0007	0178	3748	7a96	6 words
0354640	015e	0697	00d2	019a	9d54	0b59	0305	0f91	14 words
0354660	0630	01e7	0159	03bc	0000	0f9e	0643	00a0	22 words
0354700	012f	048e	0000	0f98	098a	00c5	1834	07d6	..
0354720	00fd	9048	07e1	0275	024a	07d6	0105	064e	..
0354740	07d7	0152	205c	07c1	001c	022b	07cd	003e	..
0354760	284b	07bd	004e	ff00	0068	8518	002f	0724	
0355000	16fa	2516	3347	578a	8719	00df	093f	1149	
0355020	2383	323a	4143	623b	712f	8b21	0000	0000	
0355040	0000	0000	2000	d200	0000	0020	5084	0000	
0355060	0000	0000	0000	8a31	0000	0000	0000	0000	
0355100	0000	0000	3008	3012	c155	d014	0000	0000	
0355120	0000	0000	8843	6c14	8844	2b68	984c	1801	
0355140	5002	62e8	9051	5001	5802	b852	0805	3001	
0355160	3804	4003	5004	680a	7004	9853	1003	5801	..
0355200	6805	b055	0809	1012	1816	2028	4022	4801	..
0355220	c056	0004	1009	1808	200f	4804	5804	7006	..
0355240	780a	9057	100e	5803	8058	06f0	0ed4	16ab	142 words
0355260	1eae	214f	2ec0	36dc	3ec8	46e8	4e8f	56a9	150 words
0355300	5e87	66c1	6efc	76d6	7eb1	ffff	80bc	7002	156 words

Figure 2.1: Example of the data stream as it is written in 32-bit data words. To the right the accumulated number of words in the event is given. Words that are discussed in the text are marked.

detector number, γ -ray energy, and segmented Germanium detector energy. Additionally the dirty Ge events include information about BGO time and energy. The clean BGO events include information about detector id, and give a time signal and energy information of the γ ray.

If any external data (often referred to as FERA data) is desired this follows after the `ff00` separator. The first word after this separator indicates the total number of FERA words, not including the word giving the information. In the current example 104 FERA words are included. The information of the FERA is written in no specific order and the number of words required to store the data varies. The first FERA word contains two different identification numbers. The value of the first identification lead to different parts of the set-up such as the Si detectors, the Microball, the Neutron Shell or the FMA (which includes the ionisation chamber and focal plane). The value of the second identification leads to specific signals from this part of the set-up. For example, if the first ID says the data belongs to the FMA the second ID might indicate that the data is the energy loss in the first part of the IC or the x -position in the focal plane and so on. Similarly if the first ID says “Neutron Shell” the second ID might give energy, or time-of-flight. By using the two ID:s (sometimes only the first ID is required) of the first word of each signal the important data from each event can be identified and read into the sorting program.

2.2 Handling of the γ rays

For the γ data the following steps were carried out [15]:

- **Energy Calibration**

The Ge detectors were calibrated using two different γ ray sources; ^{152}Eu and ^{56}Co . Six transitions from each source were used in the calibration with energies ranging from around 122 up to 3253 keV. For this experiment also the BGO detectors were calibrated using the ^{56}Co source which alone has peaks at energies ranging between roughly 847 up to 3253 keV.

- **Time Alignment**

The beam at the ATLAS facility at the ANL is pulsed. The pulsing provides a natural reference to measure the time against. The time signal in turn provides the possibility to connect the detected γ rays in GAMMASPHERE with the detection of recoils in the IC. For this correlation all time signals needs to be aligned. The time is also used in the pulse shape analysis from the detectors in the Neutron Shell.

- **Doppler Correction**

When the recoiling nuclei emit γ rays the energies will be Doppler shifted. The impact of this Doppler shift and broadening depends on two parameters; the velocity of the recoils and the detector position, θ . Around $\theta = 90^\circ$ the impact will be very small and then the effect will increase towards $\theta = 180^\circ$, as the detected energy is dependent on $\cos \theta$. For this experiment a second order Doppler correction was carried out, according to:

$$E_\gamma = E_{\gamma 0} \left(1 + \frac{v}{c} \cos \theta + \left(\frac{v}{c} \right)^2 (\cos^2 \theta - 0.5) \right), \quad (2.1)$$

where E_γ is the detected γ -ray energy and $E_{\gamma 0}$ is the emitted energy. The average velocity of the recoils was 4.63% of the speed of light. This velocity is measured as an average of all the recoils which end up at the focal plane of the FMA.

- **Angular Correction**

The given angle position of a Ge detector is not very exact. In fact the emit-tance angle may vary up to 15° within the crystal size. To decrease the effect of this inexact angle an angular correction was carried out. This type of correc-tion is, however, only possible if the Ge detector is segmented, i.e. electrically separated in two halves. The output signal, which corresponds to the deposited energy, can then be related to one of the two halves resulting in a finer angle determination. In the case of Compton scattering the γ ray is assumed to have emitted the largest amount of energy in the first interaction.

2.3 Neutron Handling

For each hit in a neutron detector four incoming signals are received: One energy with low and one with high amplifier gain (to get a good separation at high and low

energy, respectively), tail energy, and time-of-flight. The total energy is determined by integrating the particle's signal over a fixed time window, the tail energy is determined by doing the same but instead using a delayed time window (cf. Fig. 1.4). Hence the tail energy will give an indication of the pulse shape which can be used to separate neutrons and γ rays. For a given energy, E , the tail energy is larger for neutrons than for γ -rays.

2.3.1 Neutron- γ Separation

The four output signals; energy low (E_l), energy high (E_h), tail energy (E_t), and time-of-flight (TOF), can be used in various ways to separate the γ rays from the neutrons. This separation is mainly done by putting gates in four different spectra. The ratio between the tail energy and the low gain energy, here referred to as R , can be used to enhance the separation.

The four spectra that are used in this analysis are illustrated in Fig. 2.2. The left-hand side of the figure, panels 1A, 2A, 3A, and 4A, illustrates the initial spectra. The gates are also marked out here. Two gates are used in each spectrum (except for spectrum 4A); one for γ rays, marked with dashed lines, and one for neutrons, marked with solid lines. On the right-hand side of the figure, panel 1B, 2B, 3B, and 4B, the same spectra are incremented again but with gating restrictions. Panel 1B is incremented under the restrictions that the neutron gates in 2A and 3A are valid. In the spectrum in panel 3A the high amplifier gain is used. This means only signals with a low energy signal will be well separated using this spectrum. The gate is hence only used if the energy is below a determined value. In a similar way must the neutron gates in 1A and 3A be valid for the spectrum in panel 2B to be incremented, and so on. The gate in panel 4A is different from the rest as it is only used to make a good separation of neutrons with a high energy. Panel 4B is hence only incremented under the restriction of a valid gate from 1A and at the same time the gate in 2A.

To fit the gates so that they include as many neutrons as possible and at the same time not include any γ rays can be hard. The gates are changed iteratively to increase the efficiency and make the identification as clean as possible. In order for a neutron to be identified it has to fulfil the gate in 1A, 2A, and 4A simultaneously. Furthermore the neutron must have an energy above the determined value or be included in the gate in 3A. The use of both gate 3A and 4A is necessary to properly separate both high and low energetic neutrons. The plot in 3B illustrates this by the small inclusion of γ rays at low energy and time of flight.

2.3.2 Two-Neutron Event Suppression

Ideally an incoming neutron will hit and leave all its energy in one neutron detector. In practice there is, however, a possibility of the neutron to be scattered from one detector to another. In the data stream such an event will not be easily distinguishable from two separate incidenting neutrons leaving energy in two detectors. However, in the case of scattering into another detector one may assume that the two firing detectors are placed next to each other. Hence it is possible to suppress

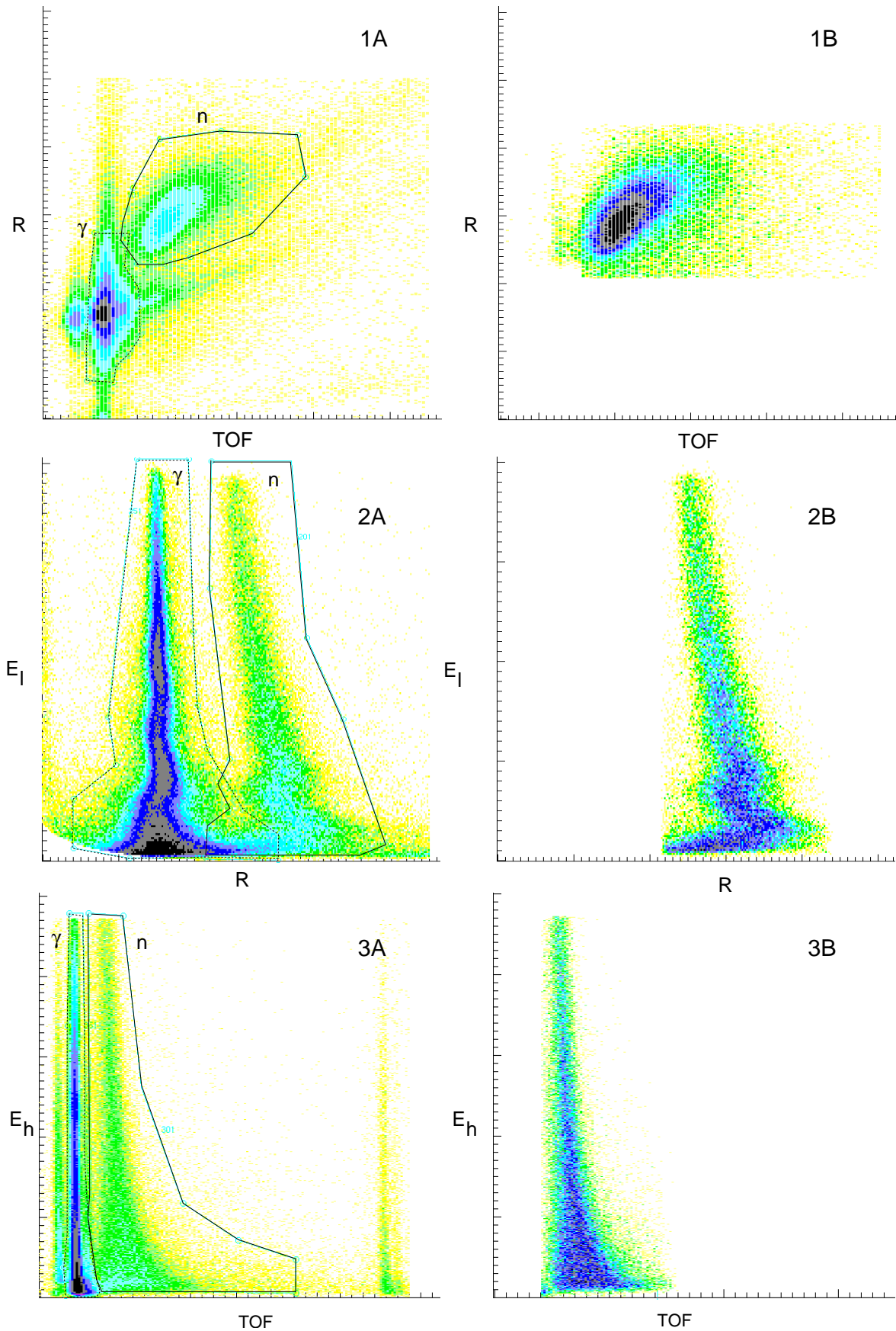


Figure 2.2: Figure illustrating the plots used to separate out neutrons from γ -rays. On the left-hand side the plots are shown with the selected gates pointed out. Solid lines correspond to neutron gates and dashed lines to γ gates. On the right-hand side the same spectra are shown again but this time the events are restricted. See text for details.

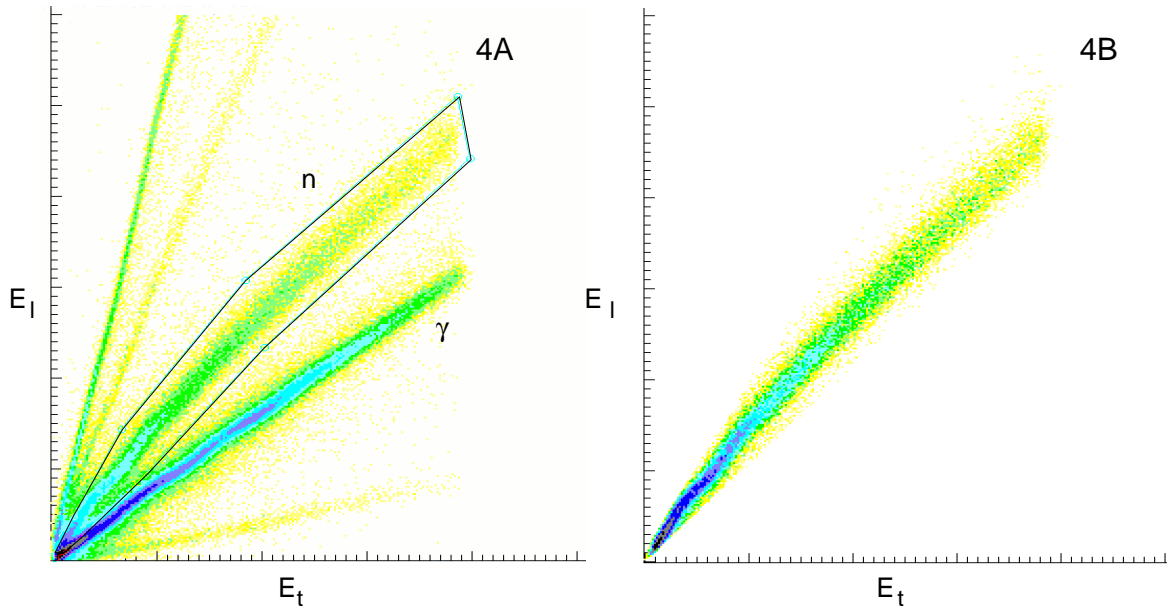


Figure 2.2: Continued

such events by assuming that all two-neutron events in two adjacent detectors in fact originate from only one scattered neutron. Figure 1.2 illustrates the relative position of the neutron detectors. This suppression may, however, also cause the rejection of real two-neutron events.

2.3.3 Neutron Identification Efficiency

One obviously wants the efficiency of the neutron detection to be 100%. Of course, in practice this is not possible partly due to the intrinsic efficiency of the neutron detectors and partly due to the fact that the Neutron Shell with its 30 detectors only covers $\sim 28\%$ of GAMMASPHERE's 4π geometry. One can estimate the neutron efficiency by measuring the intensities of a selected γ ray (originating from a recoil that has evaporated at least one neutron) in a spectrum gated on events with no neutrons detected and compare it to the intensity measured in a spectrum gated on events with one or more neutrons detected. Using ϵ_n to demote the neutron detection efficiency one gets:

$$R = \frac{I(\text{no neutrons})}{I(\text{one or more neutrons})} = \frac{1 - \epsilon_n}{\epsilon_n} \quad (2.2)$$

Rearranging this expression makes it possible to calculate ϵ_n as:

$$\epsilon_n = \frac{1}{1 + R} \quad (2.3)$$

In this case I have chosen to look at a γ -ray transition of ${}^{60}_{29}\text{Cu}_{31}$ which has been created by the evaporation of three protons and one neutron. This isotope has a transition of 454 keV which is both strong and not contaminated by other energetically close transitions. Using this transition a neutron efficiency of $\epsilon_n=0.32(3)$ is obtained. However, in the current experiment we have chosen only to include data

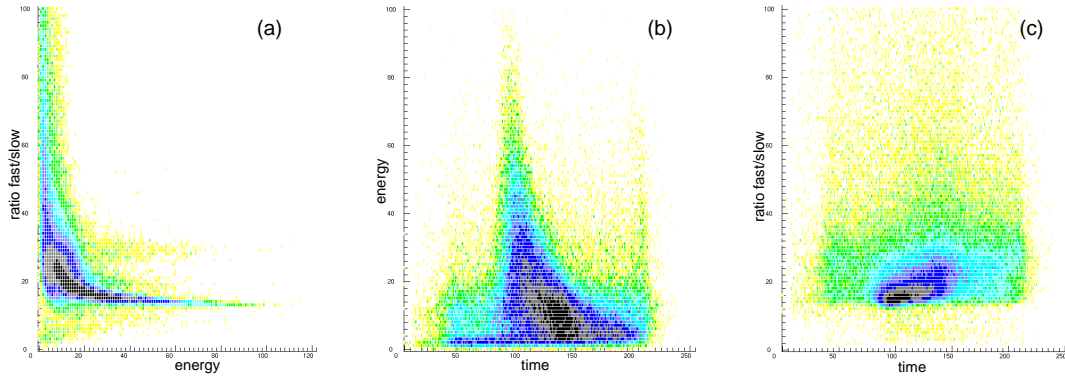


Figure 2.3: Figure illustrating the plots used to separate protons and α particles using the Microball signals.

if either four γ rays or three γ rays and one neutron was detected in coincidence. This means that the true efficiency has to be obtained under the condition of four or more γ -rays in coincidence as the discrimination is not perfect. Considering this the true neutron efficiency can be calculated. Using the same transition again the efficiency is obtained as $\epsilon_n=0.25(4)$.

2.4 Charged Particle Handling

For charged particle detection the locally developed Lu-WU-SiA in combination with the two most backward rings of Microball was used. The data handling of the Lu-WU-SiA detected particles are described in Ref. [10] whereas the separation and identification of the charged particles detected by Microball is described in the following section.

2.4.1 Proton - α Separation

The two included rings from Microball are in this setup used to detect protons and α -particles emitted at the very backwards angles (the rings are placed at 135° and 159°). The signals from the detectors are time, energy, and particle identification. The two latter are sometimes referred to as a early (fast) and late (slow) signal, respectively. Both signals are hence related to the pulse shape of the incidenting particle.

The three signals can be used to iteratively separate the protons and α particles in a manner very similar to what was done for γ rays and neutrons in Sec. 2.3.1. The procedure is further described in Ref. [16]. The three un-gated plots can be seen in Fig. 2.3. Comparing the plots in Fig. 2.3 with the gated plots, Fig. 3.4 in Ref. [16] one can see the effect of the absorber foils and the position of the rings at large backward angles which stops virtually all α particles to hit the detectors. Instead of the distinct α signals seen in Ref. [16] it is here very hard to identify any α particles.

2.5 A/Q Separation

The FMA and RMS both have the same function in the experimental set-up: they separate different species of recoils from each other. In both cases this is done via magnetic and electric fields. However, the species cannot be completely separated from each other as the separation is built on the mass number and charge state, the mass-to-charge ratio, A/Q . The charge state, Q , refers to the number of electrons removed from the atom in the target chamber. For example, this separation means that in the Oak Ridge experiment the RMS will not be able to separate between $^{61}_{29}\text{Cu}$, $^{61}_{30}\text{Zn}$, and $^{61}_{31}\text{Ga}$ nuclei. All three will end up at the same point in the focal plane. To separate recoils with the same A/Q ratio but different proton number, Z , from each other the information from the Ionisation Chamber is required, Sec. 1.6 and Sec. 2.6.

In Fig. 2.4 the relative position of recoils with different A/Q values measured at the focal plane of the FMA is illustrated. The corresponding figure for the RMS can be found in Ref. [1], Fig. 1. 5. Note that the $A = 63$ recoils are not included in the lower plot as the beam energy is too high for only one-particle evaporation.

2.6 Ion Chamber Calibrations

In order to get as good Z -resolution as possible different combinations of the energy loss in the different parts of the IC were investigated. The traditional usage of either dE1 vs dE1+dE2+dE3 or dE1+dE2 vs dE1+dE2+dE3 was already in the Oak Ridge experiment compared with other combinations to find the optimum Z -resolution. The analysis is however repeated for the ANL experiment to assure optimal resolution.

The energy loss in the IC depends on several quantities according to the Bethe-Block formula. This formula describes how much energy a particle loses per unit length when propagating through a medium:

$$-\frac{dE}{dx} \simeq C \frac{Z}{A} \frac{z^2}{\beta^2} \left[\ln \left(\frac{D\gamma^4 v^2 \beta^2}{I^2} \right) - 2\beta^2 \right], \quad (2.4)$$

where C and D are constants with values independent on the incidenting particle. Z is the proton and A is the mass number for the recoil, respectively. The charge of the incidenting particle is denoted z , $\beta = v/c$, and $\gamma = 1/(1 - \beta^2)^{1/2}$. I is the so called mean excitation potential, a difficult quantity to estimate but a semi-empirical formula for $Z \geq 13$ is $I/Z = 9.76 + 58.8Z^{-1.19}$ eV. This means that the Bethe-Block formula depends on Z , A , v , and z (related to Z and Q). Looking at one specific area on the focal plane, i.e. on recoils with the same A/Q ratio generally means that both A and Q are identical for the recoils. Hence, Eq. 2.4 depends on the proton number, Z , and the velocity, v , of the recoil. The latter dependence is undesirable and we want to correct for this. A very detailed description of how this ‘‘calibration’’ is made can be found in Ref. [1]. In principle the correction is based on the fact that the velocity will affect the energy of the recoiling nuclei. One can plot the total energy deposited in the IC on the x axis and the energy loss in the PPAC, one of the anode segments or an energy loss function of two or more of energy losses on

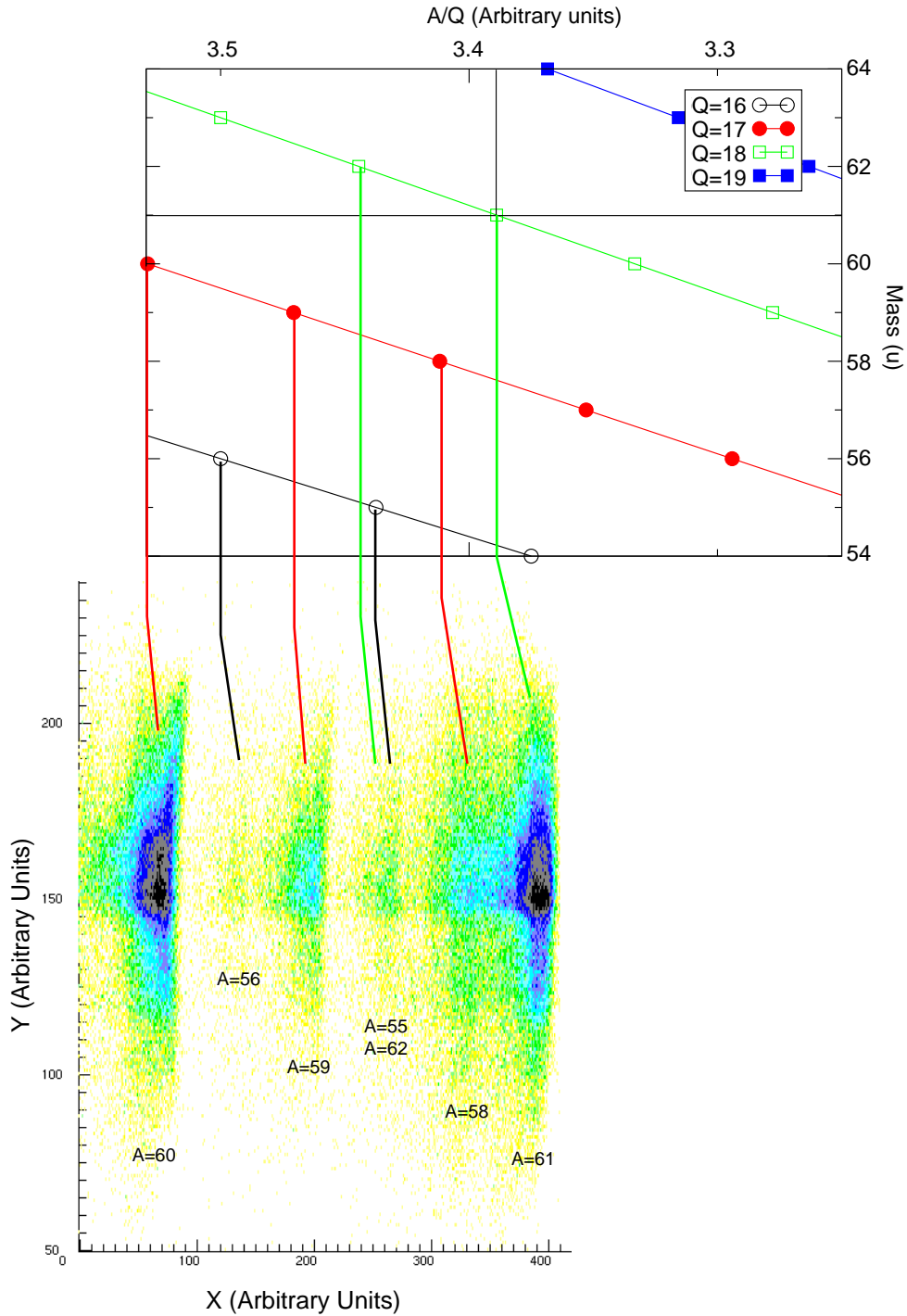


Figure 2.4: The relative position of the recoils – caused by the different A/Q values – in the focal plane of the FMA. (Top) The recoil masses plotted as a function of A/Q . The relative position of the different masses are obtained via the mass-to-charge ratio. The plot includes the full acceptance of the FMA when centring on $A = 61$, $Q = 18$ (indicated by solid lines). (Bottom) The relative position in of the recoils as measured in the focal plane of the FMA. The setting of the FMA allowed only recoils from a selected part of the focal plane to be included. Lines connecting the upper and lower part illustrates how the theoretical plot and the experimentally obtained positions are connected.

the y axis. Trying different combinations results in the conclusion that the best Z separation is obtained for an energy loss function according to:

$$R_{13} = \frac{\Delta E_1}{\Delta E_3}, \quad (2.5)$$

where the R_{13} notation is in line with Paper I and Paper II. This notation will also be used in the following.

The optimisation of the Z separation is built on two parameters. The separation between the peaks and the full width at half maximum, FWHM, of the peaks, the two parameters can be combined into a ratio and the resulting figure can then be compared to obtain the best separation.

Figure 2.5 illustrates a few examples of the obtained Z resolution from ANL when using different combinations of the energy losses. The traditionally used $dE1$ vs $dE1+dE2+dE3$ is illustrated in panel (a). Looking at Fig. 2.5 one can see that the obtained peaks have a relatively small FWHM but the separation between the two isotopes is not very good. To the right side the peaks have a tail. This may cause problems when trying to separate the different species from each other. In panel (b) $dE1/dE2$ vs $dE1+dE2+dE3$ is illustrated. The peaks have here a larger separation than in the case from panel (a) but the FWHM is a lot larger. Finally one looks at panel (c). The peaks are here more separated than for the previous mentioned cases and even though the FWHM is larger than in panel (a) there is no tail to take into account. In fact, panel (c) shows the best Z separation obtained in the analysis of both experiments.

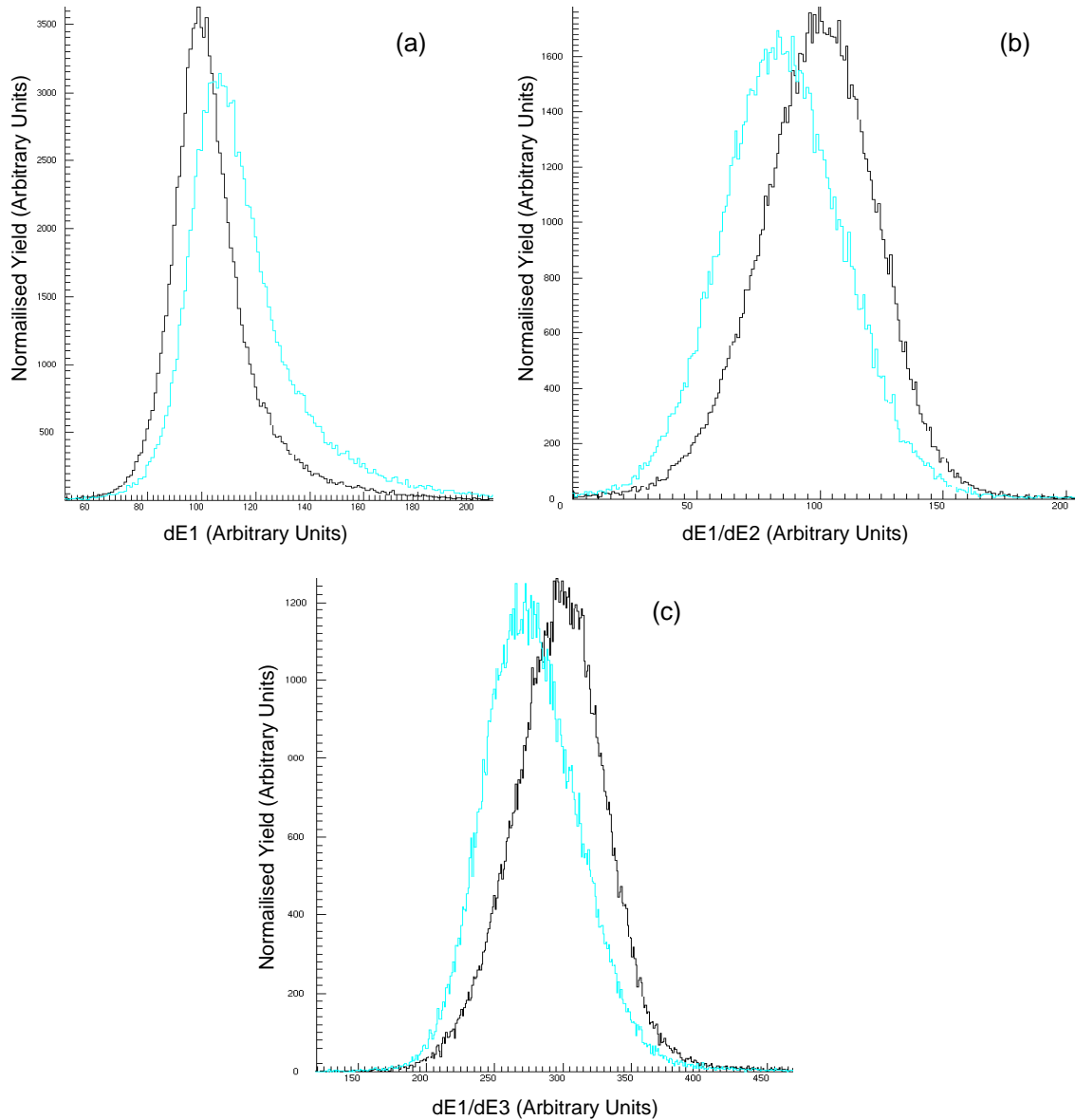


Figure 2.5: Z separation in the Ionisation Chamber. The plotted examples are from $A = 60$. Blue spectra correspond to $^{60}_{28}\text{Ni}$ and black spectra to $^{60}_{29}\text{Cu}$. Panel (a) illustrates the separation obtained when using only the energy loss in the first part of the IC, $dE1$. Panel (b) uses a ratio between the energy loss in the first and second part of the IC, $dE1/dE2$. Panel (c) shows the separation obtained if using the ratio between the first and third part of the IC, $dE1/dE3$. This is the best Z separation obtained in the analysis. See text for details.

Chapter 3

Data Analysis

The data analysis described in this chapter has been carried out for the Oak Ridge data set. In principle the same type of steps can be taken when analysing the GAMMASPHERE data but as the data handling for the experiment is not finished yet there are no results from this experiment at the present moment.

3.1 Recoil - γ Analysis

Due to the experimental set-up it is possible to make correlations between the γ rays emitted at the target position and the recoiling nuclei detected in the focal plane and stopped in the IC. This correlation allows for a recoil- γ analysis which requires a recoil- γ matrix. The matrix is a 2D plot where the γ -ray energy is plotted on the x -axis and the, from Sec. 2.6 determined, optimal energy loss combination, R_{13} is plotted on the y -axis.

The matrix can selectively be projected onto either axis providing a possibility to select what recoil to focus on by limiting the desired values of the R_{13} parameter. The matrix also makes it possible to determine the proton number, Z , of the recoils which has emitted a certain, selected γ ray. This is done by selecting the γ -ray energy and project the recoils which has emitted this ray onto the opposite axis. An example of a recoil- γ matrix can be seen in Fig. 3. 1 in Ref. [1]. The same reference and Paper I include examples of projections of the matrix onto both axes.

The recoil- γ matrix is very handy when, as often is the case, looking for γ -ray transitions from weak channels from the fusion evaporation reaction. The only problem is that not all recoils are able to enter the recoil separator due to the acceptance angle. Also some of the recoils may not travel through the separator successfully. For example in the case of the GAMMASPHERE experiment only around 0.5 % of the events have a valid FMA signal. (Another solution on how to select out weak channels is by instead using detectors around the target position inside the Germanium array. These detectors would then be able to detect the evaporated particles. In the case of the GAMMASPHERE experiment such detectors were incorporated in the experimental set-up. LUSiA and parts of Microball detected the charged particles, and the evaporated neutrons were detected by the neutron shell.)

The recoil- γ analysis is used for identifying (and in some cases determine intensities of) transitions in a selected nuclear species.

3.2 Recoil - $\gamma\gamma$ Analysis

When transitions in a specific nucleus have been identified it is possible to extend the analysis with the use of a recoil- $\gamma\gamma$ matrix. The matrix should involve only γ -rays emitted by recoils with a certain mass-to-charge ratio and with a restricted value of the R_{13} parameter to make the analysis as clean as possible.

The matrix itself has the γ -ray energies plotted on both the x and the y axis. This construction allows an analysis of γ -rays emitted in a sequence. Selecting a certain γ -ray energy and projecting it out onto one axis in practise means picking out the recoils that have emitted this γ quanta and looking at all other γ rays these recoils have emitted at practically the same time ($\Delta t \sim 20$ ns). Knowing this one can create a level scheme for the nucleus of interest. The recoil- $\gamma\gamma$ analysis can also help identifying and determine intensities of weaker transitions.

3.3 The ^{61}Ga Nucleus

An example of how to create a level scheme using the recoil- γ and recoil- $\gamma\gamma$ matrices can be found in Chapter 3 in Ref. [1]. The interesting channel was here ^{61}Ga , a very weak channel which makes the analysis fairly short due to the low number of found γ rays. The resulting level scheme can be found in Fig. 3.1.



Figure 3.1: Level scheme for ^{61}Ga . Relative thickness of the transitions corresponds to the relative intensities. The transitions and levels are marked with energies in keV. Furthermore the levels are marked with spin and parity assignments. Details about how the level scheme was derived and how the spin and parities were determined can be found in Ref. [1] and in Paper I. Dashed lines indicate tentative levels and transitions.

3.4 The ^{61}Zn Nucleus

In order to properly investigate symmetries in mirror nuclei (see Sec. 4.3) the analysis of ^{61}Ga is not sufficient but needs to be complemented by a thorough examination

Table 3.1: The average angle for the three rings corresponds to a few different detector positions. The numbers in the brackets indicated how many Ge crystals are placed at this specific angle.

Average Angle	Detector Position
90°	84° (10), 96° (10)
132°	124° (3), 128° (3), 135° (3), 139° (3)
154°	148° (4), 160° (4)

of the level scheme of ^{61}Zn . Using the experimental data from the Oak Ridge experiment one can further extend the already existing level scheme.

Using the recoil- γ analysis described in the start of this chapter a number of transitions have been found for ^{61}Zn . By including only mass $A = 61$ nuclei and limiting the value of R_{13} to correspond to the peak position of the ^{61}Zn recoil an almost clean ^{61}Zn spectrum can be obtained. The final contaminants (originating from ^{61}Cu) can be removed by performing fractional subtraction with an almost clean ^{61}Cu spectrum. The final spectrum is used for identification of γ rays in ^{61}Zn . The strong transitions can without any difficulties be identified, and even the intensities can be well determined from this spectrum. To determine the same parameters for the weak transitions the analysis requires a recoil- $\gamma\gamma$ matrix.

The matrix can hence be used to identify and determine intensities of weak transitions or transitions which are energetically hard to separate in the recoil- γ matrix. Furthermore it can be used to find coincidences to build the level scheme. The coincidence analysis is described in more detail in Paper II. The final result can be seen in Fig. 3.2. The levels are marked out in the figure with energy and spin-parity assignment. The γ rays are also illustrated with the relative thickness corresponding to the relative intensities as they are found in the experiment.

To determine the spin assignments an investigation of the multiplicities has to be carried out. To do so a clean ^{61}Zn spectrum has been obtained for all of the three rings at which the Ge-detectors are placed, 90°, 132° and 154°. The ratios of the intensities measured in these spectra are used in this investigation. It is natural to expect different ratios between the intensities measured in the detectors at 154° and 90° for different multiplicities due to the different angular distribution. Figure 3.3 illustrates the angular distribution for pure transitions with $\Delta I = 0, 1, \text{ and } 2$, respectively. When looking at the plot it is important to keep in mind that the angle of the three rings is just an average angle. In reality, the detectors are placed at slightly different angles (see Table 3.1).

The five detectors at 90° hence are placed with 10 crystals each (remember that one clover detector corresponds to four crystals) at 84° and 96°. Looking at Fig. 3.3 it is obvious that the intensities measured at 90° will be slightly different to those measured at 84° and 96° as they are placed symmetrically around the extreme value at 90°. However, measuring the intensities at 154° will indeed be an average of the intensities at 148° and 160° as there is no extreme value in between. Therefore, in the analysis of the multiplicities we are talking about the intensity ratio between the intensities measured at 154° and 96° (or 84°). The ratio is hence defined as:

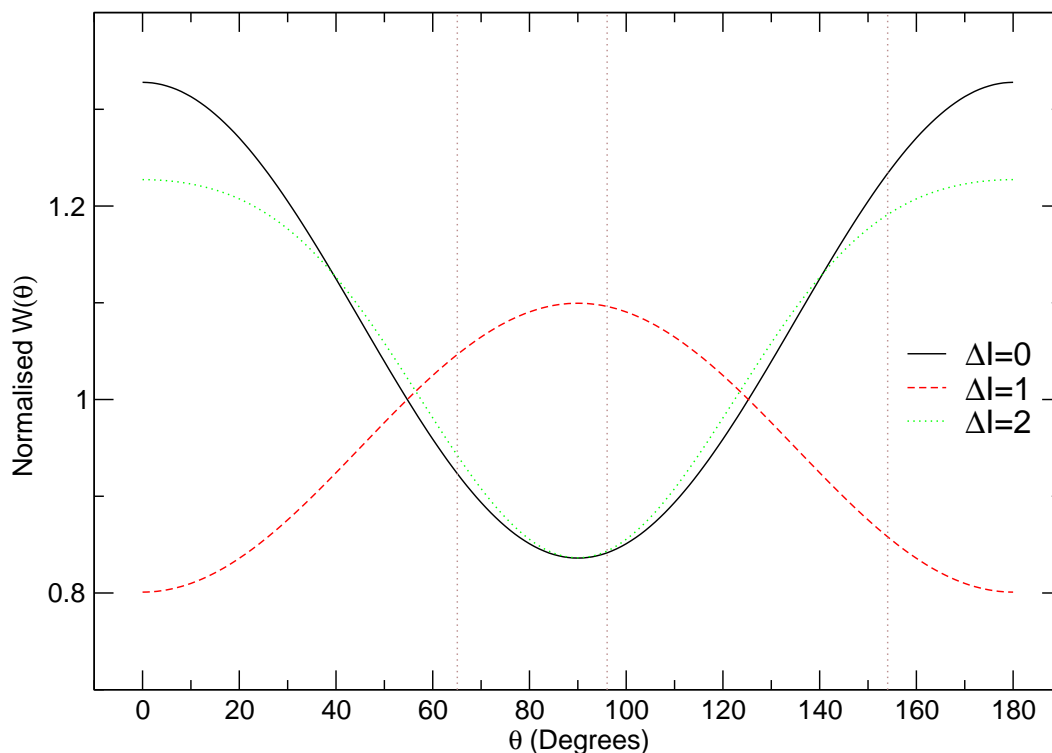


Figure 3.3: Illustration of how calculated angular distributions vary with the angle (i.e. detector position). The calculation is carried out for $I_i=19/2$ and an excitation energy of 5.5 MeV. Note the convergence for $\Delta I = 0, 1$ and 2 at $\theta \sim 55^\circ$. Two of the vertical lines represent the detector positions at 96° and 154° . The last vertical line represents the average angle of all the detectors; $\bar{\theta}=65^\circ$. More details about the latter are given in Sec. 3.5.

$$R_{154-96} = \frac{I(\text{measured in ring at } 154^\circ)}{I(\text{measured in ring at } 96^\circ)}. \quad (3.1)$$

Using this the multiplicities of the transitions can be proposed. For $\Delta I = 0, 2$ a R_{154-96} value of $\sim 1.5-1.8$ is expected, while for $\Delta I = 1$ R_{154-96} should be around $0.7-0.8$. The results are included in Table 1 in Paper II.

The R_{154-96} ratio should be more and more pronounced, or characteristic, with increasing excitation energy. This is because all compound nuclei are fully aligned. When emitting particles this alignment becomes less pronounced, as is the case the more γ -rays that are emitted. This means that the recoiling nuclei will go from being oriented in the same direction in space to being more and more “displaced”. No matter the orientation if the nuclei the angular distribution will be the same seen from the nucleus, seen from the detectors this is however not the case. If plotting the R_{154-96} value against the excitation energy this trend can be seen quite easily. Figure 3.4 illustrates this, here previously identified transitions, [17] and [18], are illustrated in black ($\Delta I = 1$), or green ($\Delta I = 2$). The transitions found this analysis are also indicated coloured red ($\Delta I = 1$), or blue ($\Delta I = 2$). The dotted lines are drawn to illustrate the general trend. The value of the intensity ratio may in some transitions be contaminated by strong energetically close lying levels – often referred

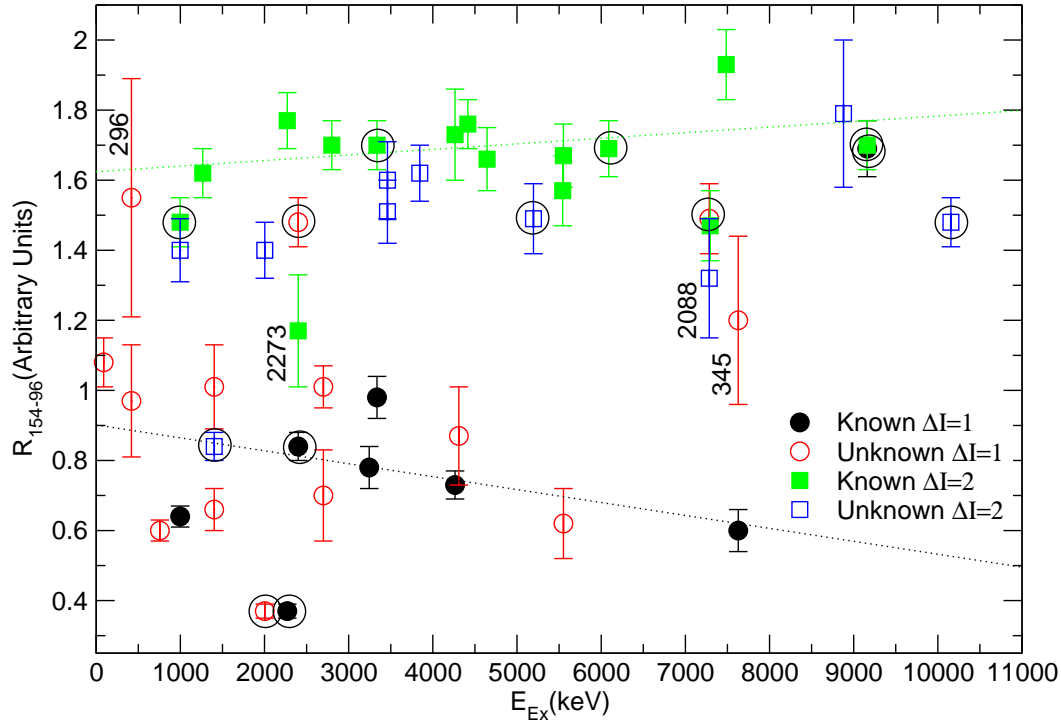


Figure 3.4: The R_{154-96} ratio for the different γ rays are plotted as a function of the excitation energy, E_{ex} . Known transitions are referred to as transitions listed in either Ref. [17] or Ref. [18]. The values of the R_{154-96} ratio become more pronounced at higher excitation energies. Circled symbols indicate doublet nature (cf. table 1, Paper II). See text for details.

to as doublets. The ratio then obviously does not get very reliable, and transitions for which this happens are encircled in Fig. 3.4. These transitions can naturally end up in the wrong position in the plot, not illustrating the general trend. Apart from these transitions there are a few transitions that do not fit into the general trend.

Naively one could interpret the low-spin states in an extreme single particle model. Here it is interesting to see that the 296 keV transition transition, similar to the 124 keV transition, moves between levels with $\Delta\ell = 2$ but both transitions are $\Delta I = 1$. This indicates an expected $E2/M1$ mixing. Also note that the 296 keV level moves between a level of lower to higher spins ($3/2 \rightarrow 5/2$). This is also affecting the angular distributions and may cause the position in the plot.

Note that the ground state transition is not included in the plot in Fig. 3.4 as it is treated in a special manner (see Sec. 3.4.1 and Paper I).

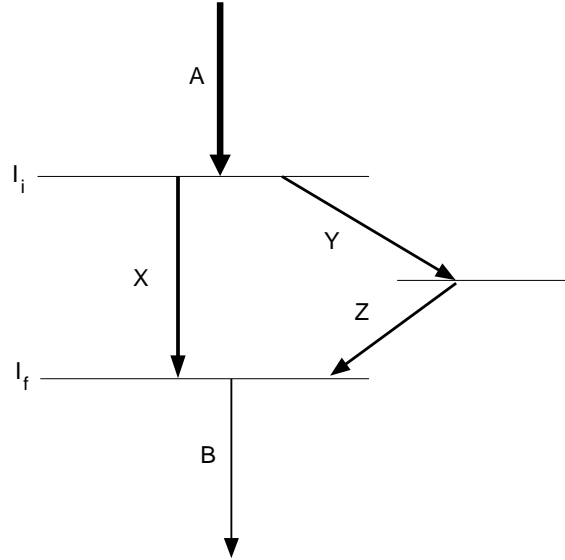
3.4.1 Specific Transitions

The energetically close transitions

There are several transitions at about the same energy. One example is the 1531, 1532, and 1538 keV transitions. Obviously this will cause difficulties when determining energy, intensity, and multipolarity of the transitions. Below follows a general way to determine the properties.

To determine energy is the easiest of the three. By gating at various transitions around the desired one, here referred to as X, one can try to eliminate γ -rays in coincidence with other transitions placed energetically close to X. To get a reliable final result it can even be useful to make a number of measurements and draw a conclusion from that.

Figure 3.5: Example of required transitions for determining relative intensities in a level scheme. To determine the intensity of the $I_i \rightarrow I_f$ transition X we need either (i) one transition going into level I_f and one decaying out from ditto, indicated as Z and B, or (ii) one transition decaying into level I_i and one decaying out of ditto, indicated as A and Y. The intensity of all four transitions A, Y or B, Z have to be well known.



To determine intensities is harder. If transition X is the transition from level I_i to level I_f determining the relative intensity requires two other well known transitions in the vicinity of transition X. The two transitions either should be placed like transition A, Y in Fig. 3.5, or like transition B, Z, i.e. one decaying into and one decaying out from the same level as transition X. The well known transition (A or B) can then be used to compare intensities in the projections of the $\gamma\gamma$ matrix. The intensities measured in the cut should be compared between the unknown transition X and the known transition (Y or Z) and using this the desired intensity can be determined and recalculated into a value relative to the strongest transition, in this case the 124 keV ground state transition. Table 1, Paper II provides the results. Some of the transitions are difficult to determine due to their doublet nature. These are marked out in the table to indicate that the energies, intensities and multipole ratios may be affected by another energetically close transition (where the procedure described above cannot be applied).

The only γ -energies that were not possible to separate are the two 1675 keV transitions placed in the same sequence. The energy of these has instead been determined from the level energies, with uncertainties resulting from all the other transitions in that sequence.

124 keV transition

One transition which causes particular difficulties is the strongest transition, from the first excited to the ground state, at 124 keV. There are two main transitions going into the 124 keV level: the 873 keV transition with a relative intensity of about 73 units and the 1141 keV transition at a relative intensity of 83 units. Totally the

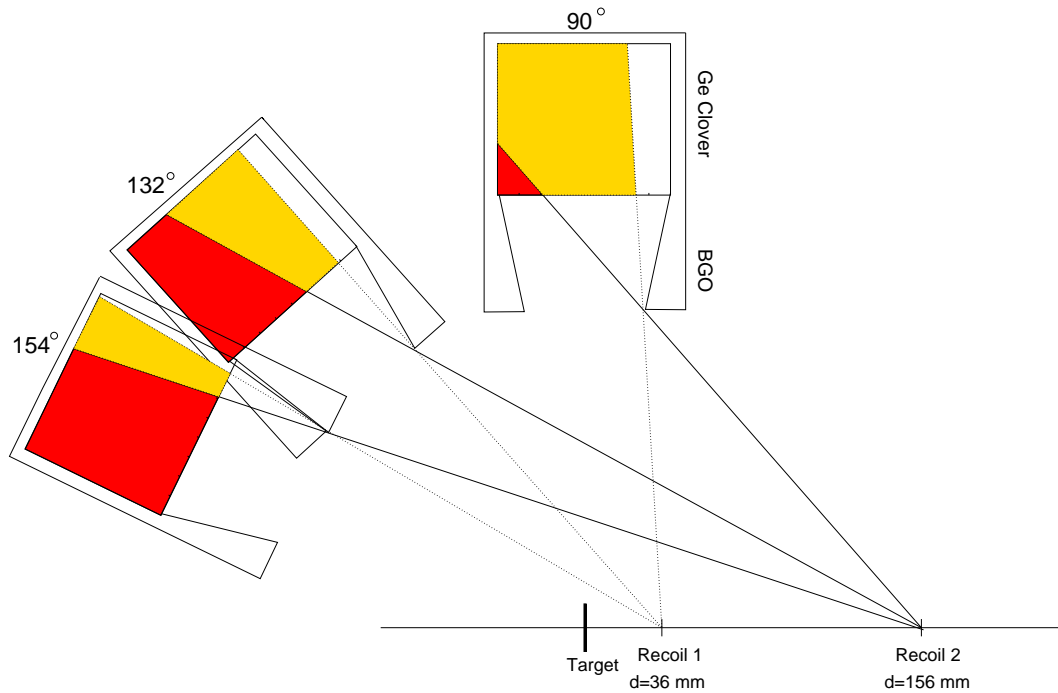


Figure 3.6: Sketch of the experimental setup with one detector in each of the three detector rings drawn out. Two positions of a flying recoil are illustrated. Emitting a γ ray from position 1 means that the white parts of the detector volumes are impossible to hit due to shadowing. In the case of recoil 2 the white and the yellow parts are impossible to hit. See text for further details.

relative intensity into the 124 keV $5/2^-$ level is hence about 159 units. But the decay out is only 100 units. This calls for an explanation of where 1/3 of the incoming intensity disappears.

One explanation is the competition between γ decay and internal conversion. Another possible explanation is that the 124 keV level has a substantial life time. The latter would cause it to be able to fly out of reach of the Ge-detectors before the γ ray was actually sent out. The information about the experimental set-up can be used to count backwards; if we only see 2/3 of the total decay in, how long will the lifetime have to be in order to account for this?

Figure 3.6 shows a sketch of the set-up around the target position. The three detector rings are illustrated in two dimensions with only one detector from each ring. Looking at the figure it is important to keep in mind that the positions of the detectors in the ring are in fact not the real position angle but rather an average of the positions of the detectors in a ring. Figure 3.6 illustrates a recoil in two positions; 1 and 2. Moving away from the target position means that a larger and larger part of the detectors will be shadowed the further away from the target the recoil moves. In position 1 the white areas (in three dimensions these are volumes) of the Ge crystals are shadowed. When the recoils fly further away from the target, position 2, the white *and* the yellow areas are shadowed. The detectors are in this estimate actually assumed to be positioned at 90° , 132° and 154° . Furthermore the recoils are assumed to fly on a straight line. The latter is true for the recoils that are able to enter the recoil or mass separator.

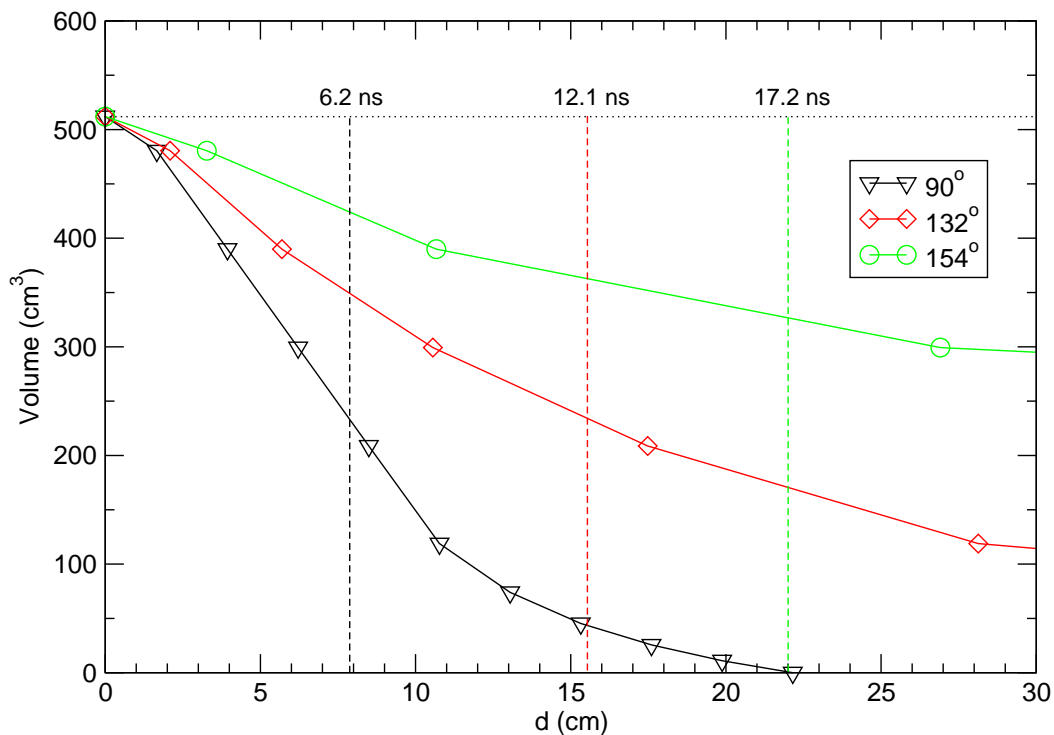


Figure 3.7: Plotting the volume of the “accessible” part of the Ge detectors as a function of distance, d , from the target is the first step in the lifetime estimate. The area under each of the three graphs are approximated with a square – the particle is either in reach or out of reach of the detectors. For 6.2 ns are the particles within reach of the detectors at 90° . The corresponding times for the detectors at 132° (154°) are 12.1 ns (17.2 ns). See text for details.

In Fig. 3.7 the volume of the detectors that still are within reach for the γ rays are plotted as a function of the distance, d , from the target. Obviously the volume will differ with the position of the detector which results in three plots, one for each ring. Here we make an approximation. The area under the graphs are approximated with a square – either the γ ray is within reach of the detectors or it is not. For the detectors at 90° the recoils are no longer within reach after 7.9 cm. Using this distance, and the velocity of the recoils being 4.26 % of the speed of light, means that after 6.2 ns the recoils will no longer be able to reach the detector. With a total of 5, 3, and 2 detectors at ring 90° , 132° 154° this means that the total time that the recoils are within reach of the Ge-array is:

$$\langle t \rangle = \frac{5 * 6.2 + 3 * 12.1 + 2 * 17.2}{(5 + 3 + 2)} = 10.2 \text{ [ns]} \quad (3.2)$$

Using the common formula

$$N = N_0 e^{-\frac{t}{\tau}}, \quad (3.3)$$

where N is the number of non-decayed recoils (i.e. the “missing” intensity when decaying out from the level), which will be denoted $N_{non-decayed}$ in the following. N_0 is the total number of particles (i.e. the amount of total γ -ray intensity into the

level) and t is the time the recoils still are within reach of the detector. We do not know the lifetime, τ , of the level but it can be calculated if knowing the observed decay in and decay out from the $5/2^-$ level. The sum $N_0 = N_{non-decayed} + N_{decayed}$ can be used when rewriting Eq. 3.3 as:

$$1 - \frac{N_{decayed}}{N_0} = \exp^{-\frac{t}{\tau}}, \quad (3.4)$$

Plotting $N_{decayed}/N_0$ versus τ for the different rings plus an average of all the detectors results in the plot in Fig. 3.8. The lifetime can here be determined using the experimentally measured $N_{decayed}/N_0 = N_{decay\ out}/N_{decay\ in}$. In order to obtain a reasonable lifetime for the level the internal conversion factor must also come into play. This factor depends on what type of multipole the transition is. Plotting the intensity ratio for the 124 keV transition in the two rings, R_{154-96} , versus the $E2/M1$ mixing ratio results in Fig. 3.9. The experimentally obtained value $R_{154-96} = 0.91$ for this $\Delta I = 1$ transition hence indicates either a pure dipole or a pure quadrupole character.

In Fig. 3.8 the dashed lines illustrate how the experimentally obtained ratios give $\tau = 15, 22$, and 10 ns for detectors placed at $132^\circ, 152^\circ$, and an average of all the detectors, respectively. These lifetimes are obtained assuming we have a pure dipole transition, where the internal conversion is very small, namely $\sim 4\%$. The lifetime obtained for the detector ring at 90° , $\tau = 4$, is small in comparison to the other lifetimes. One possible explanation is that the detectors at 90° will not give an entirely reliable ratio as the target is placed directly underneath them. This may result in a “shadowing” of these detectors even if the recoil emits γ rays at the target position, which is not the case for the other detectors.

It seems reasonable to use the lifetime of 10 ns obtained for a pure dipole transition for the average of all the detectors. If instead assuming a pure quadrupole transition the internal conversion contribution is larger, around 30% , resulting in $\tau \sim 6$ ns as an average for all detectors.

Looking back at the first step in this approximation, the detectors will be more and more shadowed the further from the target position the recoil travels, Fig. 3.6 and the plot Fig 3.7. Hence it is obvious that, depending on what value of τ we choose, we have to correct the values of the experimentally obtained ratio. The correction factor for each ring can be calculated using Eq. 3.4, using τ as determined above and t , the time when γ rays still can hit the detectors in that particular ring, as determined in Fig 3.7. The correction factors are determined as 1.2 (2.2) for detectors at 154° (96°) in case of a dipole transition. The corresponding numbers for a quadrupole transition will be 1.1 (1.6). The corrected R_{154-96} value then becomes about 0.5 (dipole) or 0.6 (quadrupole). Using an average of there we get $R_{154-96} = 55$ and $\tau \approx 8$ resulting in a final mixing of $\delta(E2/M1) \approx 1$.

The double doublet; 1403 and 997 keV

Two transitions of 1403 keV and two of 997 keV have been experimentally observed in this analysis. The four transitions can be seen in Fig. 3.2 and in Fig. 3.10. Starting from the $9/2^+$ level at 2400 keV the nucleus can either decay via emitting a 1403 keV followed by a 997 keV γ ray or inversely emitting first a 997 keV followed by a 1403 keV γ ray. Since the two different decay possibilities are strongly linked it is

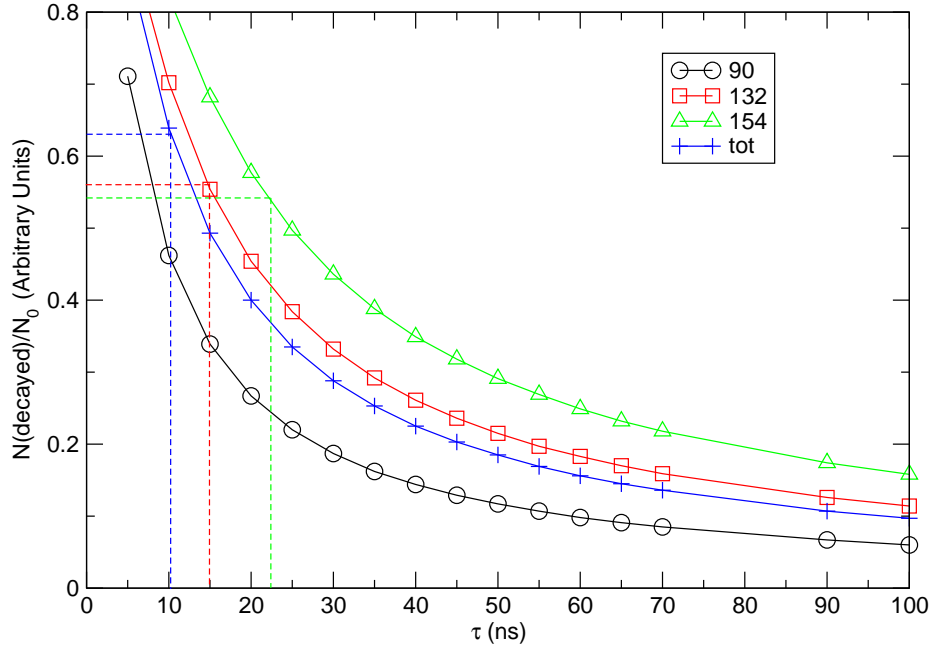


Figure 3.8: The ratio between decay out and decay in of the $5/2^-$ level plotted as a function of the lifetime, τ . The dashed lines indicates the experimentally obtained values, i.e. no internal conversion included, of decay in and out for two of the detector rings. Red marks the detectors at 132° and green at 154° . The corresponding value for the detectors at 90° is not indicated. See text for details. The blue line illustrates the total for all the detectors resulting in a lifetime of around 10 ns, if assuming a pure dipole transition.

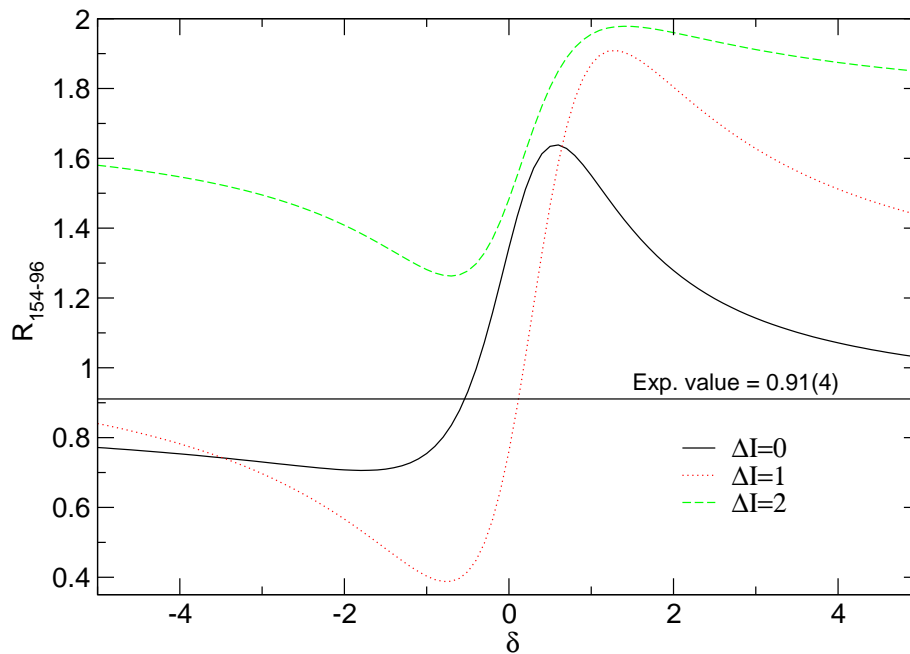


Figure 3.9: The intensity ratio R_{154-96} plotted as a function of δ , the multipole mixing ratio. The 124 keV transition is a $\Delta I = 1$ transition so the experimental value of $0.91(4)$ should be compared to the red curve in the plot. The horizontal line indicates that the mixing is either so that the transition is a pure dipole ($\delta \sim 0$), or a pure quadrupole ($|\delta| \gg 0$). The value on δ will affect the internal conversion factor and, hence, in turn the lifetime of the state.

hard to determine the intensities of the four transitions. This is further complicated by the fact that the 1403 \rightarrow 997 keV transition goes between yrast states which makes it really strong in comparison to the much weaker 997 \rightarrow 1403 keV transitions which has an intermediate state of yrare nature.

Due to the fact that the yrast transitions are so strong it may be hard to see any indication at all of the yrare transitions. However, there are other ways to determine their existence. In this case we can select out two transitions to help the analysis; the 1273 keV $11/2^- \rightarrow 7/2^-$ and the well determined yrast 1403 keV $9/2^+ \rightarrow 7/2^-$ transition. By comparing the ratio between the intensities of the 873 keV and the 997 keV transitions in the two cuts we can determine whether there is a yrare decay route present at all. If the ratio is the same in the two cuts there is no contributing 1403 keV yrare transition. If the ratios are not the same this indicates a yrare transition at 1403 keV which of course will be contaminating the selected yrast transition. This would result in a larger intensity of the 997 keV transition, originating from the $9/2^+ \rightarrow 7/2^-$ transition in coincidence with the 1403 keV transition. This relation is also what can be seen when performing the investigation. However, it is important to keep in mind that the analysis is further complicated by the energetically close 994 and 1396 keV transitions higher up in the level scheme.

So the existence of the double doublet is determined but now the relative intensities should be determined. The main problem is that all four transitions originate from the 2400 keV $9/2^+$ level. Gating on high energies will include both the yrast and yrare 997 and 1403 keV transitions. Instead we try to approach the problem from another direction.

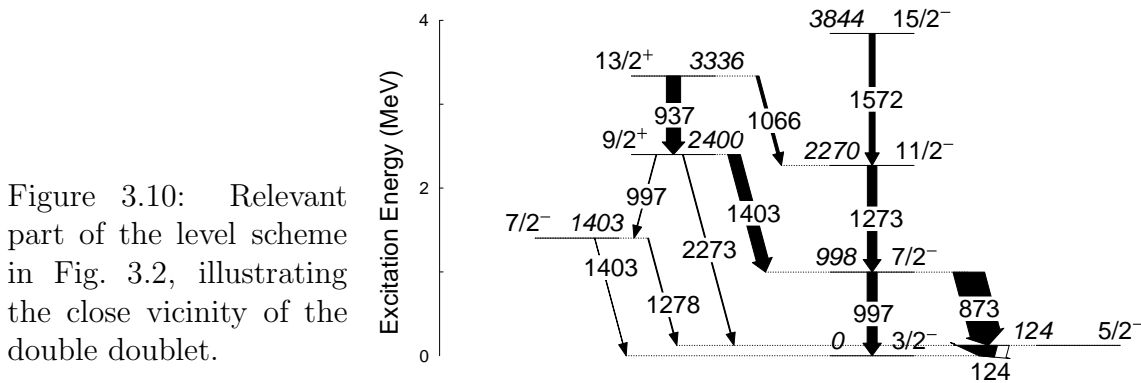


Figure 3.10: Relevant part of the level scheme in Fig. 3.2, illustrating the close vicinity of the double doublet.

Using the 1273 keV or the 1572 keV transition the branching ratio of the transitions decaying out from the 998 keV energy level can be determined. The relative intensity of the 997 keV and the 873 keV transition has here been established to 0.36(8). This information can be combined with the information of the intensity of the 873 keV transition of 72.9(22) to obtain the intensity of the yrast $7/2^- \rightarrow 3/2^-$ ground state transition. This results in the intensity listed in Table 1 in Paper II. The intensity of the yrare 997 keV transition can not be determined in this manner due to the yrast level of the same energy and the 994 keV, $31/2^- \rightarrow 27/2^-$, transition.

The analysis of the Oak Ridge experiment would end here as it is not possible to fully determine the intensities of all four transitions with the information in this data set. However, it is possible to estimate the intensities if using information from

a GAMMASPHERE experiment. This experiment involved a ^{28}Si target and a ^{40}Ca beam at 125 MeV. In this experiment ^{61}Zn was populated at lower energies, suppressing the problem with interfering γ -ray transitions between higher lying levels such as the 994 and 1396 keV transitions. The data set also provides the unique possibility of gating on the 124 keV γ -ray and simultaneously on another γ -ray transition. We can here compare the probability of decaying via the $1403 \rightarrow 873 \rightarrow 124$ keV transitions with the total probability of emitting a 1403 keV γ -ray, independent of decay route. It turns out that 64(4)% of the 1403 keV γ -rays originate from this decay route. By using the branching ratio between the 997 keV and the 873 keV transitions one can find that 24(5)% of the emitted 1403 keV γ -rays originates from the $1403 \rightarrow 997$ keV decay pattern. Hence the 1403 keV yrare transition will end up with an intensity of 12(7)% of the total intensity of the 1403 keV transitions. The resulting intensities can be found in Table 1 in Paper II.

Determining the intensities of the yrare 997 keV transitions is also done using the GAMMASPHERE data set. In the Oak Ridge data the 997 keV transition has been determined to have an intensity of 27(6) units. This intensity is almost equal to the total intensity of the two 997 keV transitions as found in the experiment. This complicates the determination of the 997 keV yrare transition. The GAMMASPHERE data set can, however, be used again. It indicates the yrare 997 and 1403 keV transitions to be about equally intense. This indication is used to set the relative intensity of this transition to 5(3), as listed in Table 1, Paper II.

3.4.2 Superdeformed Band

The experimentally determined spin and parity assignments are indicated in Fig. 3.2 and listed in Table 1 in Paper II. These assignments are in some cases supported by the assignments in Ref. [18]. However, the assignments are not in line with the tentative assignments of the levels in the superdeformed (SD) band in Ref. [19].

According to the analysis made by C. -H. Yu *et al.* the superdeformed band will decay via two transitions into the normally deformed level scheme. The two transitions decay into the 6090 and the 7629 keV levels, as seen in Fig. 3.2. These levels are assigned spin and parity $21/2^+$ and $23/2^-$, respectively. Assuming the SD band is correctly identified, i.e. that the lowest state in the band – the band head – in fact is placed at 11367 keV these assignments will affect the spin and parity assignments in the band. The transitions in the SD band from Ref. [19] are all of $E2$ character. This means that if the band head were assigned spin and parity I^π then the level at 12799 keV would have an assignment according to $(I + 2)^\pi$. This leads us to two transitions connecting the super and normally deformed level schemes;

$$I^\pi \rightarrow 21/2^+, \text{ and} \quad (3.5)$$

$$(I + 2)^\pi \rightarrow 23/2^-. \quad (3.6)$$

Due to the difference in parity one can determine the spin and parity of the levels in the SD band. The assignments will be based on the fact that the $M2$ transitions are not very strong at all. One would therefore expect $I^\pi = 23/2^-$ and $(I + 2)^\pi$ will

hence equal to $27/2^-$ which would mean that the two connecting transitions would be of $E1$ and $E2$ character, respectively. This spin-parity assignment is different to the tentative assignment in Ref. [19]. The modification also changes the positive, $\alpha = +1/2$, signature of the SD band, as found in Ref. [19], to become negative, $\alpha = -1/2$. This will in turn affect the discussion concerning the configuration of the SD band made in the same reference.

3.5 Angular Distribution Corrections

The positioning of the Ge detectors is vital for a correct relative intensity of the $\Delta I = 0$, $\Delta I = 1$, and the $\Delta I = 2$ transitions. In this experiment a total of ten Ge-detectors have been used. Five of these were placed at 96° , three at 132° , and two at 154° . This gives a mean angle, $\bar{\theta}$, of 65° . However, looking in Fig. 3.3 one can see that at 65° the relative intensity of $\Delta I = 0, 2$ and $\Delta I = 1$ transitions are not equal. The figure instead shows that the intensity of $\Delta I = 1$ transitions will be more efficiently detected than $\Delta I = 0$ or $\Delta I = 2$ transitions. An ideal angle for the relative intensity of the transitions to be equal is 55° , or 125° as can be seen in Fig. 3.3. The uneven detection of $\Delta I = 0$, $\Delta I = 1$, and the $\Delta I = 2$ transitions needs to be corrected for. The correction simply consists of determining a factor by which the intensities can be scaled to get a appropriate relative intensity.

Figure 3.3 illustrates the almost identical behaviour of $\Delta I = 0$ and $\Delta I = 2$ angular distributions at 65° . This means that these two types of transitions can be corrected using the same correction factor. To determine the correction factors some knowledge about the angular distribution, $W(\theta)$ is required.

The angular distribution formula can experimentally be fitted to:

$$W(\theta) = 1 + q_2 a_2 P_2(\cos \theta) + q_4 a_4 P_4(\cos \theta) \quad (3.7)$$

where q_2 and q_4 are two parameters which account of the finite opening angle of the detectors. P_2 and P_4 are given by

$$P_2(\cos\theta) = 0.5(3 \cos^2 \theta - 1) \quad (3.8)$$

$$P_4(\cos\theta) = 0.125(35 \cos^4 \theta - 30 \cos^2 \theta + 3) \quad (3.9)$$

and

$$a_k = \alpha_k A_k^{max}. \quad (3.10)$$

a_k denotes the angular distribution coefficients and α_k are the spin alignment coefficients. α_2 can be expressed by an empirical parametrisation, which depends on the excitation energy of the initial level, E_x , (this is also illustrated in Fig. 3.4) according to

$$\alpha_2 = 0.55 + 0.02 \cdot E_x. \quad (3.11)$$

The excitation energy is given in MeV. Furthermore, for each value of α_2 there is a corresponding value of α_4 and the angular distribution coefficient is given by A_k^{max} if the spins are completely aligned. More information can be obtained from Ref. [20].

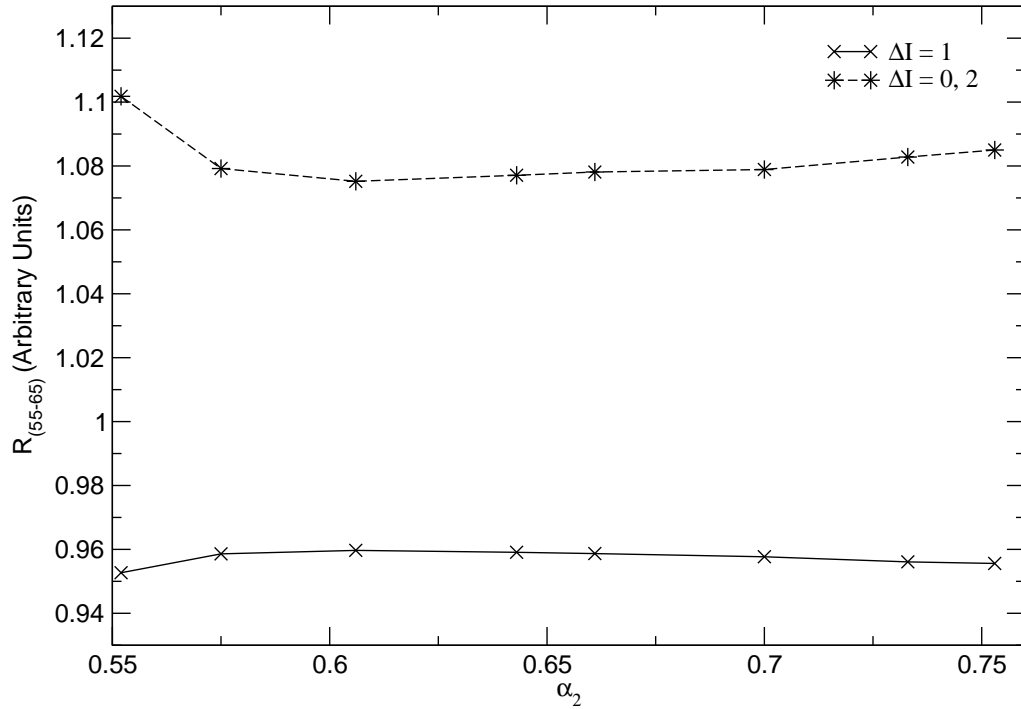


Figure 3.11: From this plot the correction factors for the transitions of different ΔI can be obtained. The value for $\Delta I = 1$ was here determined as 0.95(2) and for $\Delta I=0, 2$ the factor was 1.09(2). See text for details.

The correction factor should in principle be dependent on the excitation energy of the level as the angular distribution is dependent on α_2 . To see how strong this dependence is the plot in Fig. 3.11 was made. Here the intensity ratio between detectors placed at the ideal 55° compared to the real position at 65° , R_{55-65} , is plotted versus α_2 . As can be seen in the figure the dependence is not very strong and as an average it was determined to use only one correction factor for all the levels, independent of excitation energy. The correction factors have been determined to 0.95(2) for $\Delta I = 1$ and 1.09(2) for $\Delta I = 0$ and $\Delta I = 2$.

Chapter 4

Theoretical Background

This chapter deals with the theoretical background required to interpret and predict the experimental data. Section 4.1 introduces the shell model and in Sec. 4.2 the shell model calculations using the code ANTOINE are explained as well as different interactions used for calculations in this report. In this chapter and in Chapter 5 low spin states will refer to states with an angular momentum of $19/2$ or below and, consequently, high spin states will refer to all states with an angular momentum above $19/2$.

4.1 The Shell Model

The nuclear shell model attempts to explain the behaviour of nuclei in a similar manner as the Bohr model does for atoms. The thought is simply to arrange the nucleons, i.e. the protons and neutrons, into a shell structure consisting of major shells and, within these, minor shells – so-called subshells or orbitals. The shells closer to the centre of the nucleus are often referred to as the “inner” shells, these are lower in energy than the outer and hence, in a non-excited state, the nucleons fill the inner shells first. Similarly to the atomic model, the nucleons in a filled shell or orbital are not as likely to get excited as the nucleons in an unfilled shell, the latter are often referred to as valence nucleons, which in many low-energy cases determine the behaviour of the nucleus.

Experimentally the shell model is supported in several ways. One example is rapid changes in separation energy at certain number of neutrons and protons. These rapid changes occur at $N = Z = 2, 8, 20, 28, 50, 82, \dots$ for spherical nuclei close to stability. The numbers are often referred to as the “magic numbers” and are interpreted as the number of nucleons required to fill a major shell.

Inside the nucleus two forces dominate: the attractive strong force between the nucleons and the repelling Coulomb force between the protons. The strong force is (luckily) very strong at short distances and keeps the nucleus bound together. In order for the nucleons to co-exist inside the nucleus the Pauli Principle has to be fulfilled. The principle tells us that two identical particles inside the same nucleus cannot have the same quantum numbers. Firstly, as the neutrons and protons are separated by their difference in charge, they do not occupy the “same” orbitals – i.e. one can think of the neutrons and protons separately when filling the different shells inside the nucleus. This means that both types of nucleons can reach a magic

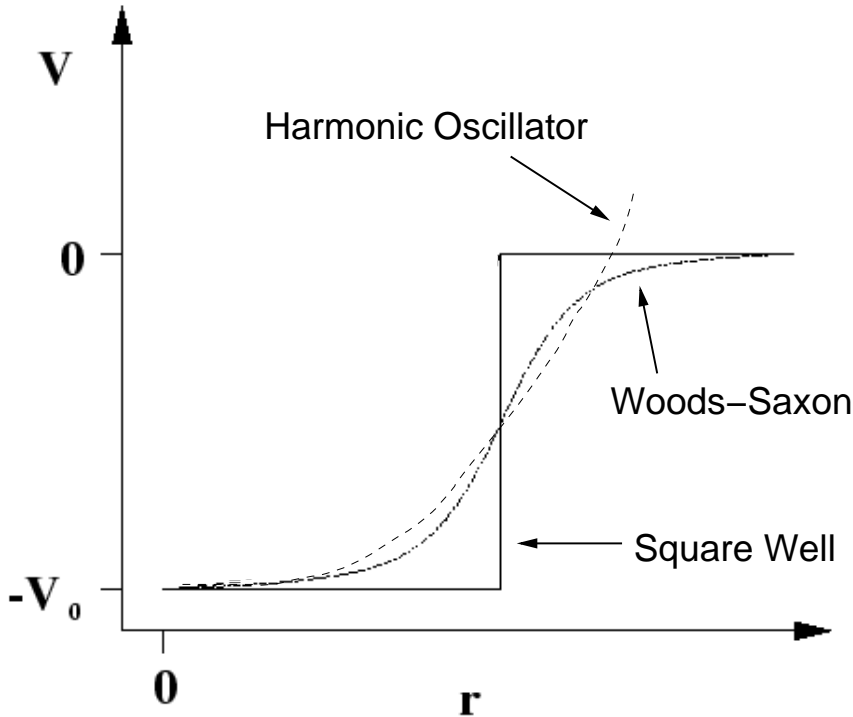


Figure 4.1: A comparison of the three nuclear potentials in two dimensions. See text for details. The figure is taken from Ref. [21].

number simultaneously which would make the nucleus in question “doubly magic” and hence very tightly bound. One example of a doubly magic nucleus is ${}^{56}_{28}\text{Ni}_{28}$ where the first excited state is at 2700 keV [22]. This can be compared with a non magic nucleus like for example ${}^{60}_{30}\text{Zn}_{30}$ where the first excited state experimentally is found at 1003 keV [23].

In order to describe and predict nuclear properties one needs to be able to describe the nuclear potential mathematically. Starting out with the square well and the harmonic oscillator, both unable to fully reproduce a plausible potential, finally the Woods-Saxon potential was developed as a cross over between the above mentioned two. The potential shapes are compared in Fig. 4.1.

Each level reproduced by the potential is given a quantum number ℓ connected with the orbital angular momentum. The ℓ quantum number starts at 0 and can take positive integer values, the denotation of ℓ is, however, often in letters as s, p, d, e, f, g, and so on. Each ℓ level can host $2(2\ell+1)$ nucleons. This is due to the projection of ℓ onto the z axis giving the quantum number $m_\ell = 0, \pm 1, \pm 2, \pm 3, \dots, \pm \ell$ which gives $(2\ell+1)$ combinations. This is then multiplied by two due to the fact that the spin quantum number, for fermions $s = 1/2$, can be orientated in either positive or negative z direction, $m_s = \pm 1/2$. Furthermore, we have the quantum number n which counts the number of levels with orbital angular momenta ℓ . Starting at 1 n takes all integer values. Lower numbers correspond to inner orbitals. These notations are all included in panel (a) in Fig. 4.2 where the shell structure using the Woods Saxon potential has been predicted. Each level is here denoted $n\ell$. As can be seen the theoretical model reproduces the lower magic numbers but not

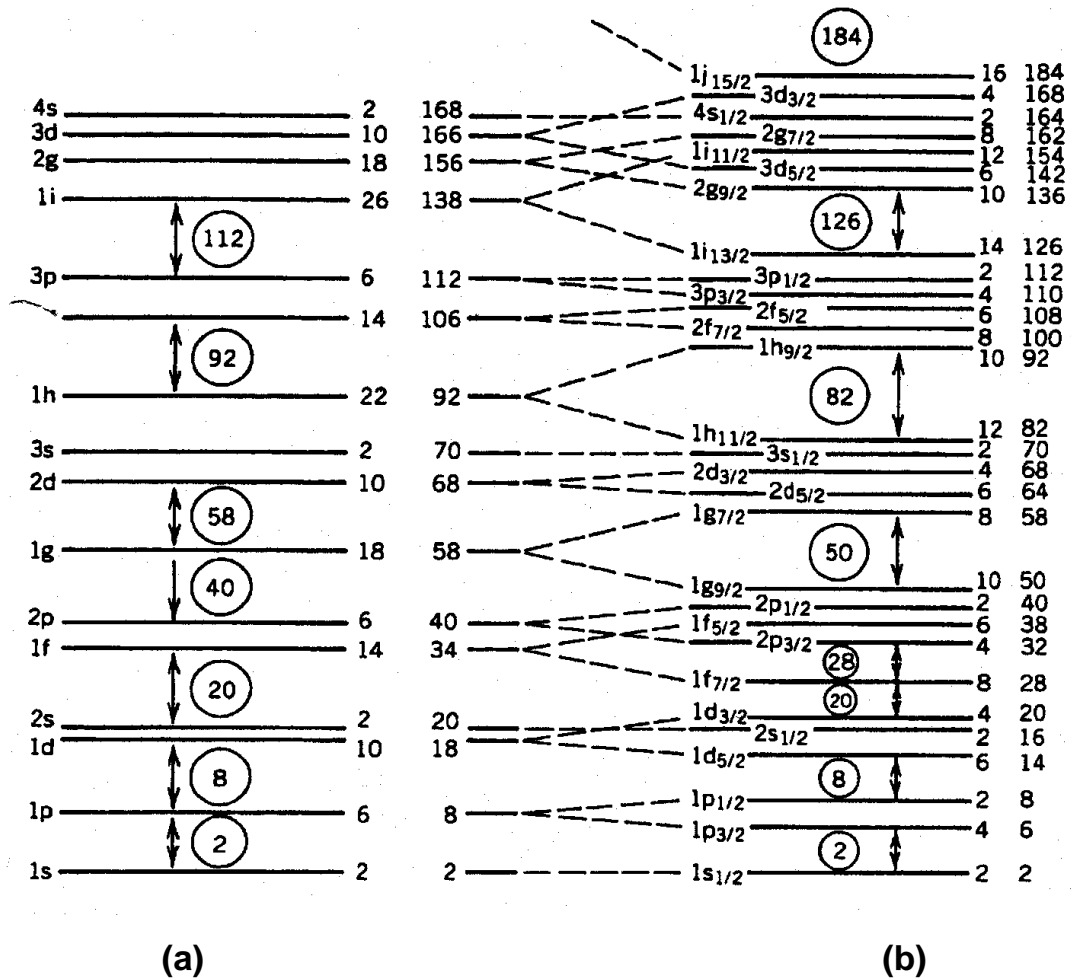


Figure 4.2: To the left (a) the energy levels calculated with the Woods-Saxon potential are illustrated. To the right (b) the results using the same potential but including the spin orbit interaction are shown. To the right of each level the degeneracy of that level is indicated as well as the accumulated number of nucleons up to and including each level. Circled numbers indicates the magic numbers. See text for details. The figure is taken from Ref. [24].

the higher ones. In order to get a result more in line with the experimental data the spin-orbit potential was added to the Woods-Saxon potential. The spin-orbit potential couples the orbital angular momentum, ℓ , and the intrinsic spin, s to a total angular momentum, $\mathbf{j} = \mathbf{l} + \mathbf{s}$ and similarly the quantum numbers are coupled so that $j = \ell + s$ or $j = \ell - s$ where s , as mentioned earlier, is equal to $\pm 1/2$. The j quantum number can then also be projected onto the quantisation axis, z , in $(2j+1)$ ways denoted by the m_j quantum number that from now on replaces the m_ℓ and m_s quantum numbers. As can be seen in Fig. 4.2 this results in a splitting for each level in panel (a), into two new levels with different values of j . In each case the higher j value ends up with a lower energy. The denotation in panel (b) and in the following sections in this report is now $n\ell_j$ for each orbital, for example does the ground state of ^{61}Zn have one unpaired neutron in orbital $2p_{3/2}$. The figure also clearly illustrates the perfect reproduction of the experimentally obtained magic

numbers which is a good indication of that the model works. Another way to test the model is to compare the predictions with the experimental data of, for example, ${}_{30}^{61}\text{Zn}_{31}$. Here the 30 protons and 31 neutrons in the ground state fill the orbitals resulting in two protons and three neutrons outside the magic $1f_{7/2}$ orbital. Two nucleons of the same kind can, if occupying the same orbital, pair up to spin zero. This kind of pairing can, however, be broken if energy is brought into the system. In the ground state we therefore expect the ${}_{30}^{61}\text{Zn}_{31}$ nucleus to have spin $I^\pi = 3/2^-$ originating from the unpaired neutron in the $2p_{3/2}$ orbital. The π denotes the so called parity which is correlated to the symmetry of the wave function. The parity is easily determined by the simple equation $\pi = (-1)^\ell$.

The spins of excited states are not equally easy to foretell as the ground states as higher spins rarely can be interpreted in this extreme single particle model. It is also important to remember that in reality there are different probabilities for the nucleons to occupy certain levels and the wave function of a single nucleon alone – due to the effects of quantum mechanics – may be likely to occupy several orbitals at the same time.

4.1.1 Electromagnetic Transitions

When the nucleons inside atomic nuclei gain or lose energy they are said to move between the orbitals. When an excited state decays to a state of lower energy the energy difference between the two orbitals is then emitted from the nucleus in the form of light. The properties of the emitted light is then dependent on the spin and parities of the levels between which the nucleon moves. If the initial state has spin I_i and parity π_i and the final state correspondingly has I_f and π_f then conservation of angular momentum gives:

$$\mathbf{I}_i = \mathbf{L} + \mathbf{I}_f, \quad (4.1)$$

where \mathbf{L} is the angular momentum of the γ ray. The equation results in a vector addition where $|I_i - I_f| \leq L \leq |I_i + I_f|$, where L can only take integer numbers. Also if $\pi_i = \pi_f$ the radiation has even parity and if $\pi_i \neq \pi_f$ the radiation has negative parity. This makes it easy to determine the character of the radiation field as:

$$\pi(ML) = (-1)^{(L+1)} \quad (4.2)$$

$$\pi(EL) = (-1)^L, \quad (4.3)$$

where M stands for magnetic and E for electric character. The conclusion is that if the parity between the two nuclear orbitals is the same then for even L the γ ray has electric character and magnetic character for odd L . Correspondingly for opposite parity odd L gives electric and even L gives magnetic character. The spin and parity of a level can hence be determined if the multipolarity, L , and the character, T, of the γ ray is determined as well as I^π of the other involved state. The multipolarity can experimentally be determined via comparing intensities of a certain γ -ray energy in detectors placed at different angles. This is due to the difference in angular distributions.

It is also possible to estimate the decay constant λ which is the probability to decay by sending out a γ ray per unit time. This constant can be estimated if assuming that the transition is due to a single nucleon that moves between two orbitals. The equations for the decay constants are then:

$$\begin{aligned}\lambda(EL) &\cong \frac{8\pi(L+1)}{L[(2L+1)!!]^2} \frac{e^2}{4\pi\epsilon_0\hbar c} \left(\frac{E_\gamma}{\hbar c}\right)^{2L+1} \left(\frac{3}{L+3}\right)^2 cR^{2L} \\ \lambda(ML) &\cong \frac{8\pi(L+1)}{L[(2L+1)!!]^2} \frac{e^2}{4\pi\epsilon_0\hbar c} \left(\frac{E_\gamma}{\hbar c}\right)^{2L+1} \left(\frac{3}{L+2}\right)^2 cR^{2L-2} \left(\mu_p - \frac{1}{L+1}\right)^2 \left(\frac{\hbar}{m_p c}\right)^2\end{aligned}\quad (4.4)$$

where m_p and μ_p is the proton mass and nuclear magneton, respectively, and E_γ is the γ -ray energy given in MeV. The radius, R , in Eq. 4.4 can here be estimated as $R = r_0 A^{1/3}$, and the term $(\mu_p - \frac{1}{L+1})^2$ can be replaced with 10 to get the so called reduced transition probabilities, $B(TL)$, where T is the character of the radiation:

$$\begin{aligned}B(EL) &= \frac{1}{4\pi} \left(\frac{3}{L+3}\right)^2 (r_0 A^{1/3})^{2L} \quad [e^2 f m^{2L}] \\ B(ML) &= \frac{10}{4\pi} \left(\frac{3}{L+2}\right)^2 (r_0 A^{1/3})^{2L-2} \quad [\mu_N^2 f m^{2L-2}]\end{aligned}\quad (4.5)$$

The units may seem a bit strange but are standard with e being the effective charge and μ_N is the nuclear magneton given by $\mu_N = e\hbar/2mc$.

Since the angular momentum of the γ -ray is calculated via $|I_i - I_f| \leq L \leq |I_i + I_f|$ there are generally different multipoles allowed for one single transition. Evaluating the so called Weisskopf estimates originating from Eqs. 4.4 gives values which are not supposed to be the experimentally obtained transition probabilities but rather a reasonable number to compare with. If an experimentally obtained transition rate agree with the Weisskopf estimates one knows that there is a good matching of initial and final wavefunctions in the transition which also has to be caused by the transition of a single nucleon.

When comparing the values of the Weisskopf estimates it is seen that the transition with the lowest multipole order by far gives the highest contribution [24] in an estimate of the relative strength of the allowed multipoles and characters for a given transition. Assuming an $A=61$ nucleus and a γ ray of 1 MeV the relative intensities for the first three multipoles would be:

$$\begin{aligned}\lambda(M1) : \lambda(E2) : \lambda(M3) : & 1 : 3.2 \times 10^{-4} : 6.8 \times 10^{-11} \\ \lambda(E1) : \lambda(M2) : \lambda(E3) : & 1 : 3.6 \times 10^{-7} : 8.7 \times 10^{-11}.\end{aligned}\quad (4.6)$$

In the upper case one might expect a mixture of M1/E2 character of the transition. The degree of mixing between the two multipole characters in a non-pure transition like this is denoted δ . Delta is defined as the higher multipolarity over the lower, i.e.

$$\delta^2 = \frac{\lambda(TL+1)}{\lambda(TL)},\quad (4.7)$$

where T again is the character of the radiation.

4.1.2 Two-state Mixing

Even though it is easy and convenient to think of configurations and transitions as caused by a single nucleon is this never the case in reality, instead real states comprise a mixing between a number of configurations. In the shell-model calculations, Sec. 4.2, the properties of the wave functions of the different levels are calculated by diagonalising a large Hamiltonian matrix. If then two states of the same spin and parity are placed close in energy it is possible that the wave functions of the two states becomes mixed in the calculation. If the initial levels have wave functions ϕ_1 and ϕ_2 , respectively, we can denote the wavefunctions after the mixing with ψ_I and ψ_{II} . The mixed wavefunctions can then be expressed as linear combinations of the two initial wavefunctions involved in the mixing:

$$\begin{aligned}\psi_I &= \alpha\phi_1 + \beta\phi_2 \\ \psi_{II} &= \alpha\phi_2 - \beta\phi_1,\end{aligned}\tag{4.8}$$

where α and β are the mixing components which have to fulfil the conditions $\alpha > \beta$ and simultaneously $\alpha^2 + \beta^2 = 1$.

The amount of mixing between the states depends on two parameters; the energy difference between the two unperturbed levels, and the mixing matrix element. The latter is often denoted $\langle\phi_1|V|\phi_2\rangle$, or simply V . An example of how the mixing equations 4.8 can be used is described in Sec. 5.2. Here the mixing has been done via the matrix elements calculated in the shell-model calculations.

4.2 Shell-Model Calculations Using the Code ANTOINE

The shell model calculations carried out here are made with the code ANTOINE [25, 26]. For the nuclei presented in this licentiate thesis ($A=61$) shell model calculations including the full fp shell ($1f_{7/2}$, $2p_{3/2}$, $1f_{5/2}$, and $2p_{1/2}$) are necessary to obtain reasonable predictions for low spin levels. If the predictions also should comprise high spin levels the calculations ought to involve not only the full fp shell but also the $1g_{9/2}$ orbital. The latter, due to its high- j nature, plays a significant role already at moderate excitations energies for $N \sim Z$ nuclei in this mass region. The development of the shell model calculations is in constant progress and many different interactions are accessible. The KB3 [27] and the later developed KB3G [28] interactions together with the GXPF1 [29, 30] and the later version GXPF1A [31] interactions use the four orbitals in the fp shell. The two former interactions are particularly successful for nuclei in the lower fp shell whereas the latter two work best for nuclei around doubly magic ^{56}Ni . Calculations mainly using the GXPF1 interaction are reported in detail in Chapter 5. For comparison a second interaction has been tried out; this is the $f_{5/2}pg_{9/2}$ interaction. This excludes the $1f_{7/2}$ orbital from the calculations but includes the $1g_{9/2}$ orbital instead. Both interactions are introduced and described in more detail below. The results from the calculations are described in Chapter 5 and a comparison between the two has been carried out.

4.2.1 The GXPF1 and GXPF1A Interactions

As already mentioned the GXPF1 interaction includes the full fp shell i.e. the $1f_{7/2}$ orbit below and the $2p_{3/2}$, $1f_{5/2}$, $2p_{1/2}$ orbitals above the $N=Z=28$ shell closure. The interaction has been empirically fitted to nuclei beyond the above mentioned shell closure (the nuclei vary between $20 \leq Z \leq 32$ and $47 \leq A \leq 65$ [30]) by adjusting the strength of interaction parameters.

Due to the fact that only odd ℓ -orbitals are included in the configuration space no positive parity states can be predicted in this calculation for the two odd-A nuclei included in this report. Two calculations have been carried out with this interaction. Both involve three particle, three hole excitations, i.e. $t = 3$ from the $1f_{7/2}$ orbit into the upper fp shell. The first calculation includes no Coulomb interaction but in the second calculation the Coulomb force has been included in the form of Coulomb multipole matrix elements, V_{CM} , derived from harmonic oscillator wave functions. In addition, the single-particle energies for protons and neutrons, respectively, have been modified according to the contributions from the electromagnetic spin-orbit interaction, $V_{C\ell s}$ (explained further in Sec. 4.3) and radial effects, V_{Cr} (the Thomas Ehrman shift)[32, 33]. The latter depend on the difference in proton minus neutron occupation number between the excited state and the ground state. In the current calculation the values of the shifts are taken from Ref. [34].

Shortly after the release of the GXPF1 interaction a modified version of the interaction was released. The release of the new interaction was based on a non satisfactory result of the predictions especially for non-stable neutron-rich nuclei. In this interaction the separation between the neutron orbitals $p_{1/2}$ and $f_{5/2}$ is less than in the GXPF1 interaction. The effect is a different gap between the $f_{5/2}$ and the $g_{9/2}$ orbital, too.

The impact of this change in interaction affects the calculations to some extent. A comparison of the results is discussed in Chapter 5.

4.2.2 The “ $f_{5/2}pg_{9/2}$ ” Interaction

This interaction uses a ^{56}Ni core allowing excitations only outside this core. This means that the $1f_{7/2}$ orbit is excluded from the calculation with expected difficulties in reproducing low spin states. In the $f_{5/2}pg_{9/2}$ configuration space, as indicated by the name, the $1g_{9/2}$ orbital is included and the interaction used here is adjusted for nuclei with $Z > 28$ and $N < 50$. The calculations with this interaction have been carried out with the help from E. Caurier in Strasbourg as the interaction is not released yet. In the current calculations no Coulomb effect has been included and the number of particle-hole excitations into the $1g_{9/2}$ orbital is unlimited.

4.2.3 The KB3G Interaction

Similarly to the GXPF1 interaction the KB3G interaction includes the $1f_{7/2}$, $2p_{3/2}$, $1f_{5/2}$, and $2p_{1/2}$ orbitals. In spite of the fact that the interaction covers the same orbitals in the shell model as the GXPF1 interaction, KB3G is proved to be more successful in the lower fp shell, for nuclei with mass number, $A \leq 52$ [30]. In this report the calculations using this interaction is only used as a reference.

4.3 Mirror Nuclei

Mirror nuclei are nuclei which contain the same number of nucleons, but the number of protons and neutrons are interchanged. Disregarding the Coulomb force between the protons the two nucleons behave the same inside the nucleus. This means that the proton and the neutron can be viewed as two states of the same particle. To differ between the two a new quantum number is introduced: the isospin quantum number t . When projected onto the quantisation (z) - axis the magnitude of t is the same but the orientation differs. Neutrons have $t_z = +1/2$ and, correspondingly, protons have $t_z = -1/2$. The sum of the projections gives the total isospin for the nucleus, T_z :

$$T_z = \frac{1}{2}(N - Z) \quad (4.9)$$

where Z and N are the proton and neutron numbers, respectively.

Assuming isospin symmetry two mirror nuclei would reveal identical decay schemes. Only the Coulomb force and isospin asymmetric components in the nucleon-nucleon interaction break this symmetry and will hence cause differences in excitation energy between corresponding levels in the two mirror nuclei. These differences in energy are referred to as Mirror Energy Differences (MED). The definition of MED is:

$$MED_J = E_J(T_z = -T) - E_J(T_z = +T) \quad (4.10)$$

Here E_J denotes the excitation energy of a state with spin J .

The MED can be explained by different contributing factors. These are divided into three main groups: the Coulomb multipole effects (V_{CM}), the Coulomb monopole effects (V_{Cm}) and the isospin breaking contribution (V_{BM}). The denotations is here selected in line with Ref. [34, 35].

The isospin breaking component is supposed to account for the difference in MED that does not originate from the two components which are described in more detail below. The Coulomb force is of course to a large extent causing isospin breaking.

The multipole effect takes into account the alignment, and breaking, of proton pairs in the nucleus. The effect is related to the increased distance between an aligned, compared to an anti-aligned, pair of protons which affects the charge distribution in the nucleus. The multipole term is estimated to contribute with about 10-100 keV in MED [34].

The monopole effect on the other hand is further divided into different components such as the deformation and radial effects (V_{Cr}) as well as the so called electromagnetic spin-orbit effect (V_{Cls}). The latter occurs when single-particle excitations takes place between orbitals of opposite spin orbit coupling, i.e. between $\ell + s$ (e.g. $2p_{3/2}$) and $\ell - s$ (e.g. $1f_{5/2}$ or $2p_{1/2}$) orbitals.

To explain the V_{Cls} term in more detail a equation is required:

$$\langle V_{Cls} \rangle = (g_s - g_l) \frac{1}{2m_N^2 c^2} \left\langle \frac{1}{r} \frac{dV_C(r)}{dr} \right\rangle \langle \vec{l} \cdot \vec{s} \rangle \quad (4.11)$$

This equation illustrates the contribution from the electromagnetic spin-orbit interaction on the single-particle energies. In Eq. 4.11 g_s and g_l are the gyromagnetic factors, or g-factors, the effect of these appear when charged particles move.

Nucleons move in two ways; the orbital motion and the intrinsic spin. Obviously g_s is related to the spin and g_ℓ to the orbital motion. The g-factors are experimentally well determined for both neutrons and protons but only as free particles, inside the nucleus the nucleons pair up and the spin and orbital angular momenta add to zero. The g-factors are $g_s=5.586$ (-3.828) and $g_\ell=1$ (0) for protons (neutrons), these are the numbers used in the equation.

The mass m_N in Eq. 4.11 denotes the mass of the nucleon and $V_C(r)$ is the Coulomb potential. If assuming the nucleus is spherical with radius $R_C = r_0 A^{1/3}$, $r_0 = 1.2$ fm, the potential can be described by the following equations, see Ref. [36]:

$$V_C(r) = \begin{cases} \frac{Ze^2}{R_C} \left(\frac{3}{2} - \frac{1}{2} \frac{r^2}{R_C^2} \right) & r < R_C \\ \frac{Ze^2}{r} & r > R_C \end{cases} \quad (4.12)$$

The upper line is the potential inside the nucleus and the lower line is the potential outside the nucleus. Using this one can estimate the contribution from the electromagnetic spin-orbit interaction on the single-particle energies, see Ref. [36]. The resulting equations are approximative as a spherical nucleus has been assumed as well as $Z = A/2$:

$$\langle V_{CIs} \rangle_{\text{protons}} = \begin{cases} -20 \cdot \ell & \text{keV if } \ell + s \\ +20 \cdot (\ell + 1) & \text{keV if } \ell - s \end{cases} \quad (4.13)$$

$$\langle V_{CIs} \rangle_{\text{neutrons}} = \begin{cases} +17 \cdot \ell & \text{keV if } \ell + s \\ -17 \cdot (\ell + 1) & \text{keV if } \ell - s \end{cases} \quad (4.14)$$

Figure 4.3 illustrates the single-particle orbital shifts for neutrons and protons, respectively. This shift can also be seen experimentally, for example, via the first excited state, $I^\pi = 5/2^-$, in the two mirror nuclei. In ^{61}Ga , where the odd particle in the ground configuration is a proton, the first excited state is at 271 keV, the corresponding level in ^{61}Zn is found at 124 keV.

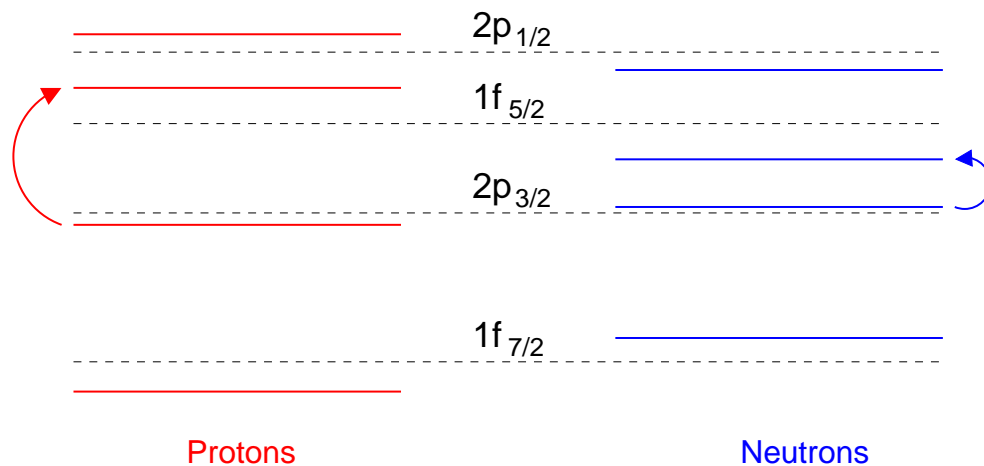


Figure 4.3: The single-particle energies have different contributions from the electromagnetic spin-orbit interaction depending on the type of nucleon and orbital. Illustrated are the shifts caused by the electromagnetic spin-orbit interaction.

Chapter 5

Interpretation

In this chapter the results from the shell model calculations will be discussed. A comparison with experimentally obtained excitation levels and relative strengths has been carried out. The results involve both ^{61}Zn and ^{61}Ga and in Sec. 5.3 a comparison between the two mirror nuclei is described.

5.1 The Shell Model Calculations

5.1.1 The ^{61}Zn Nucleus

Calculations using two of the interactions described in chapter 4.2 are reported in this licentiate thesis. Two calculations using the GXPF1 interaction, one with and one without the Coulomb effect, are presented here as well as a calculation using the $f_{5/2}pg_{9/2}$ interaction. For comparison a few results from the GXPF1A and the KB3G interactions are included as well.

The results from the shell model calculation can be seen in Fig. 6 in Article II but are also illustrated in a slightly different manner here in Fig. 5.1. The difference between the experimental and calculated excitation energies are plotted as a function of the spin of the level in the figure. The energies used in Fig. 5.1 are normalised to the experimentally determined ground state and the predicted energies are adjusted to this via the Binding Energy Shift, BES, obtained in the different calculations. Details about BES are found later in this Section. Noteworthy is the very small difference between the two GXPF1 calculations, indicating the small effect of the Coulomb interaction. Also note the expected trend of large differences for high spin states using the GXPF1 interaction. The $f_{5/2}pg_{9/2}$ calculation on the other hand works better at high spins, i.e. at spins above $19/2$, but at lower spins it generally shows a worse agreement. The same trends can also be illustrated in numbers using the Mean Level Deviation (MLD) values for the calculations. The MLD is simply the mean energy difference between the predicted and the experimentally obtained energies. When calculating MLD obviously the relative position of the compared levels is of importance. This means simply that by not setting the predicted ground state at 0 keV a lower MLD can be obtained. The MLD is obviously supposed to be as low as possible and generally the predicted level scheme hence needs to be shifted up, or down, in relation to the experimentally obtained ground state. This energy shift is often referred to as the Binding Energy Shift, BES. Both the MLD

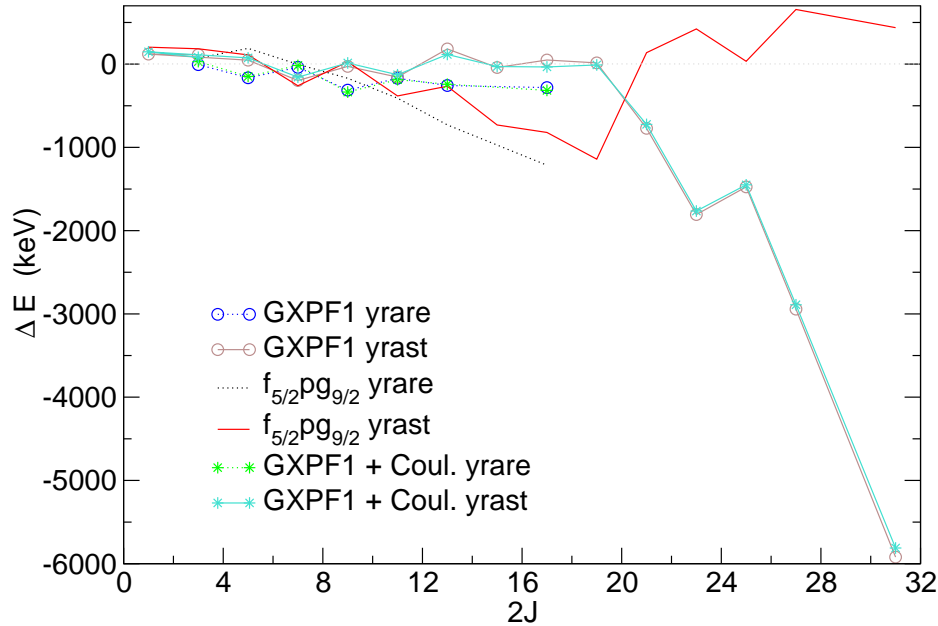


Figure 5.1: ΔE denotes the difference in energy between the experimentally obtained energy and the calculated ditto for a certain level with spin J . The plot contains both yrast and yrare states with three different interactions used. See text for details.

and the BES are dependent on how many levels are included in the calculation. It is desirable to compare the MLD values including different levels to see how well the calculations reproduce yrast/yrare, high spin/low spin levels and so on. The values are listed in Table 5.1.

The numbers in the table are quite similar for the two GXPf1 calculations. The small difference that exists varies between a few percent up to around 15%, the latter obtained for the calculation of yrast levels up to and including the $19/2^-$ level. Table 5.1 also indicates the earlier mentioned general trend; yrast levels at low spins give an MLD of 92 keV, the corresponding value for the $f_{5/2}pg_{9/2}$ calculation is 476 keV, i.e. over five times larger. In a similar way for high spin levels the MLD for the GXPf1 with Coulomb calculation, 1628 keV, is more than five times larger than the MLD of 290 keV for the $f_{5/2}pg_{9/2}$ calculation. Also note the relatively small difference between the BES values obtained for the $f_{5/2}pg_{9/2}$ in comparison to the large difference between the BES values obtained when including different levels in the two GXPf1 calculations. Finally looking at the MLD including all levels a value around 1260 keV is obtained for the fp calculations. Comparing with the high MLD for high-spin states, around 1600 keV, and the low MLD value for low-spin levels, around 100 keV, this value is expected. The corresponding number for the $f_{5/2}pg_{9/2}$ calculation is 661 keV which is higher than either of the separately calculated MLD values. The reason for this is that “all levels” includes not only yrast and yrare but also third states. In total four third states are experimentally found ($11/2$, $13/2$, $15/2$, $17/2$) and compared with the predicted values. The numbers hence indicate that the third states are well reproduced by the GXPf1 calculations. On the other hand can the same states be not very well predicted by the $f_{5/2}pg_{9/2}$ calculation.

In Table 5.2 the calculated energies for the yrast states using different interac-

Table 5.1: Mean level deviations and binding energy shifts for the three calculations in ^{61}Zn . The numbers gives an indication of how well the calculations reproduce the experimental level energies. All numbers are in keV. See text for details.

Included levels	GXPF1 Coulomb	GXPF1	$f_{5/2}pg_{9/2}$
	MLD / BES	MLD / BES	MLD / BES
all levels	1257 / -642	1261 / -723	661 / -450
yrastr + yrare levels	1334 / -740	1359 / -784	498 / -280
yrastr levels	1560 / -984	1590 / -1304	484 / -203
yrastr up to and including 19/2	92 / -82	109 / -112	476 / -382
yrastr + yrare up to and including 19/2	136 / -155	137 / -187	477 / -428
levels above 19/2	1628 / -2609	1652 / -2694	290 / 109

Table 5.2: Level energies in keV for different calculations are listed. The table only contains the negative-parity yrastr levels in ^{61}Zn .

I	Expt.	GXPF1 + Coul.	GXPF1	GXPF1A	$f_{5/2}pg_{9/2}$	KB3G
3/2	0	0	0	8	108	468
1/2	89	23	81	0	0	245
5/2	124	131	189	174	217	0
7/2	998	1237	1307	1216	1462	1263
9/2	1266	1334	1405	1332	1441	966
11/2	2270	2480	2538	2367	2856	2171
13/2	2799	2765	2729	2608	3268	2051
15/2	3844	3955	3997	3739	4778	3628
17/2	4644	4760	4707	4590	5668	3628
19/2	5543	5635	5640	5474	6888	4821
21/2	7284	8090	8167	7916	7350	8237
23/2	7629	9476	9548	9324	7410	9384
25/2	8879	10411	10466	10249	9048	10329
27/2	9161	12133	12216	12048	8708	11863
29/2	—	13931	14065	13856	9920	14147
31/2	10155	16048	16188	15881	9589	16879

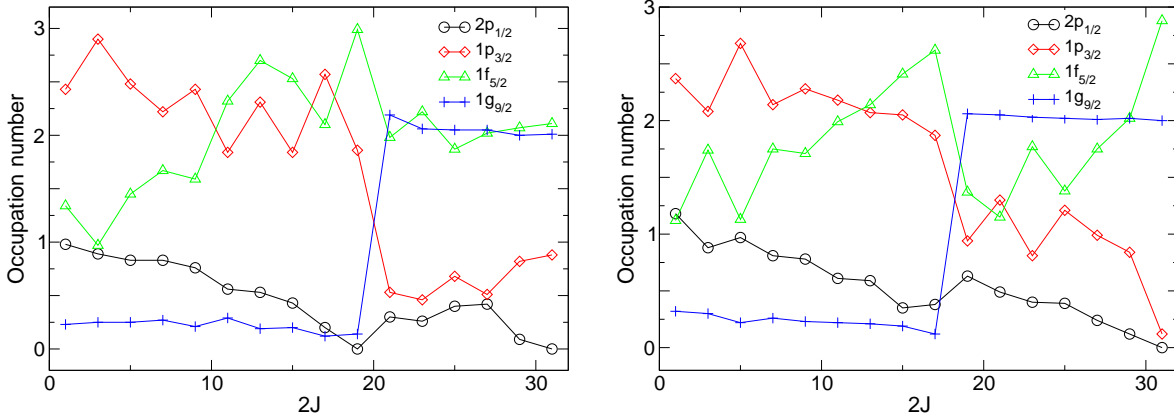


Figure 5.2: The occupation numbers for different orbitals as calculated with the $f_{5/2}pg_{9/2}$ interaction plotted against the spin of the levels. The left hand side illustrates the yrast levels, the right hand side the yrare levels. Only negative parity states are plotted. See text for details.

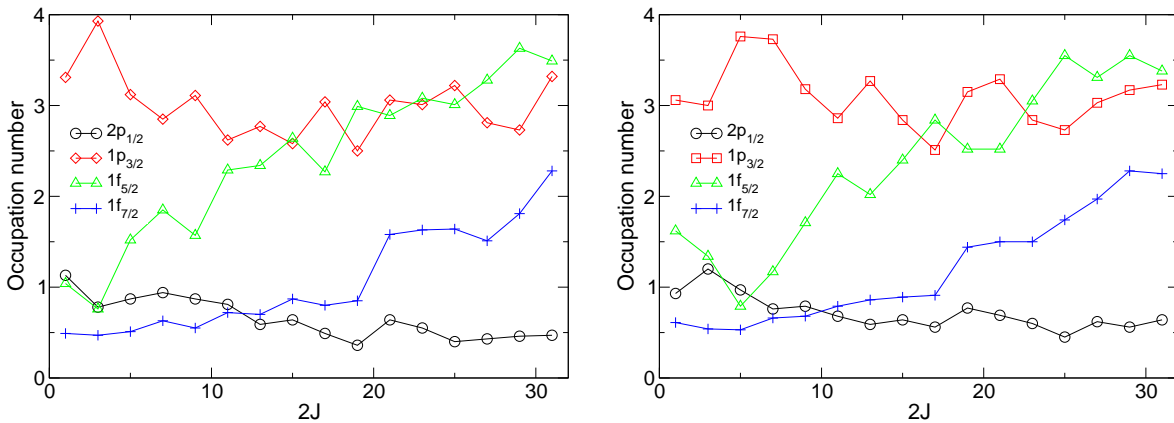


Figure 5.3: Same as for Fig. 5.2 but the occupation numbers are here calculated with the GXPF1 interaction including the Coulomb effect. In the case of the $1f_{7/2}$ orbital the plot shows holes – not particles. See text for details.

tions are listed. The table also includes the experimentally determined level energies for comparison. Looking at the result it is interesting to see that only the GXPF1 calculations can reproduce the ground state. Not even the “improved” GXPF1A interaction is able to predict the ground state correctly.

The shell model calculations can also predict occupation numbers, i.e. for each state the code can estimate the contribution of different particle configurations to the total wave function. This results in an estimate of the total number of particles in each orbital. The occupation numbers are plotted in Fig. 5.2 and Fig. 5.3 for the $f_{5/2}pg_{9/2}$ and GXPF1 with Coulomb interaction, respectively.

Figure 5.2 illustrates the results from the $f_{5/2}pg_{9/2}$ interaction. Without using any particles from the $1f_{7/2}$ orbital a maximum spin of $19/2$ can be achieved. To produce levels with higher spin than that the particles must start to fill the $1g_{9/2}$ orbital. This is also seen in the plot via the drastic jump from 0.2 particles in this orbital for spin $19/2$ up to two particles for spin $21/2$. The particles are taken from

Table 5.3: Excitation energies, γ -ray energies, and preliminary assignment of initial and final state in the decays of ^{61}Ga are listed to the left. On the right hand side the calculated values using the GXPF1 interaction including the Coulomb force are listed.

E_x (keV)	E_γ (keV)	$I_i^\pi \rightarrow I_f^\pi$	$E_x^{calc.}$ (keV)	$E_\gamma^{calc.}$
220(1)	220(1)	$(1/2^-) \rightarrow (3/2^-)$	124	124
271(1)	271(1)	$5/2^- \rightarrow 3/2^-$	349	349
1397(1)	1126(1)	$(9/2^-) \rightarrow 5/2^-$	1546	1197
—	1231(1)	—	—	—
2903(2)	1506(1)	$(13/2^-) \rightarrow (9/2^-)$	2876	1330

the $1p_{3/2}$ and the $1f_{5/2}$ orbitals. A more general trend is that the number of particles increase with increasing spin for the $1f_{5/2}$ orbital and decrease with increasing spin for the $1p_{3/2}$ orbital. This indicates that the particles are pushed further away from the core.

Figure 5.3 illustrates the corresponding situation for the GXPF1 interaction. Note that the $1f_{7/2}$ orbital illustrates holes in these graphs. Again without exciting any particles from the $1f_{7/2}$ orbital spins up to $19/2$ can be generated. However, looking at the plots there is already one particle excited from the closed $1f_{7/2}$ orbital at lower spins, still a small jump from one hole up to almost two holes can be seen at spins larger than $19/2$. The general trend here is that the number of particles are almost constant for the $1p_{3/2}$ and the $2p_{1/2}$ orbitals whereas the number of particles increases for the $1f_{5/2}$ and decreases for the $1f_{7/2}$ orbitals.

5.1.2 The ^{61}Ga Nucleus

The five transitions found in ^{61}Ga are all very low in spin and of negative parity. This makes a two-calculation analysis redundant as the $1g_{9/2}$ orbital only plays a significant role at high spins. Shell model calculations for ^{61}Ga have therefore only been carried out using the GXPF1 interaction allowing three particle excitations from the $1f_{7/2}$ orbital into the upper fp shell. The results are listed in Table 5.3.

The agreement between the experimental results and the calculations is not convincing enough to support the preliminary spin assignments. However, mirror symmetry arguments, especially when including the electromagnetic spin-orbit force can support the preliminary decay scheme. See Sec. 4.3, Sec. 5.3, and Paper I for more details.

5.2 Electromagnetic Decay Properties

To take the analysis of the results from the shell-model calculations one step further the electromagnetic decay properties have been investigated for the ^{61}Zn nucleus. The analysis is carried out using both the $f_{5/2}pg_{9/2}$ calculation and two calculations using the GXPF1 interaction (with and without including the Coulomb force). The analysis uses the free g -factors and for the $f_{5/2}pg_{9/2}$ and GXPF1 without including

the Coulomb force effective charges of $0.5 e$ ($1.5 e$) for neutrons (protons), respectively. In the GXPF1 calculation where the Coulomb force was included effective charges of $0.8 e$ ($1.15 e$) for neutrons (protons) have been used instead according to Ref. [37]. The g -factors and effective charges are applied via the $B(M1)$ and $B(E2)$ values that are obtained from the shell model calculation and which enable branching ratios to be calculated using the decay constants from Eq. 4.4 and 4.5. As can be seen in Table 5.4 the inclusion of the Coulomb force and the different effective charges do not have a very large impact on the relative strengths. The table also lists the branching ratios for the $f_{5/2}pg_{9/2}$ calculation but only levels up to and including $I^\pi = 19/2^-$. The reason for this is the poor reproduction of high spin levels using the GXPF1 interaction. Experimentally obtained relative strengths up to level $I^\pi = 31/2^-$ are listed in Table 2 in Paper II including the $f_{5/2}pg_{9/2}$ calculation and the GXPF1 without Coulomb calculation.

In both tables the calculations include all energetically allowed transitions with $\Delta I \leq 2$, independent if they are experimentally observed or not. This allows all possible transitions to be calculated and the branching ratios should then be similar to the experimental ones if the spin and parity assignments are correct. Transitions to experimentally unobserved levels should hence be very weak or equal to zero in the calculations as well.

Calculated branching ratios do generally agree well with the experimental results, especially at low spins. There is, however, one interesting detail noticed only in the analysis of the electromagnetic decay properties: the difficulty in reproducing branching ratios for the yrast and yrare $3/2^-$ levels in the fp calculation. This has been investigated in more detail and is highlighted in Table 5.5, where transitions involving the two $3/2^-$ levels are listed. The table contains three different branching ratios and lifetimes. The b_1 column is the straight forward result from the fp shell-model calculation. As can be seen there are relatively large discrepancies between the experimental and the calculated results, especially for the $7/2_1^- \rightarrow 3/2_1^-$ transition. Experimentally this is determined as 0.26(2) but the calculated branching ratio is as low as 0.01. The distinct difference is very surprising, especially when compared with the very good agreement between experimental and calculated branching ratios for all other yrast levels.

If two predicted levels with the same spin and parity are placed close in energy, shell model calculations have problems in correctly describing their electromagnetic decay properties. The problem can usually be solved by afterwards mixing the wave functions of the two states based on the matrix elements of the electromagnetic operators. However, in the current experiment *and* calculation the two $3/2^-$ states are separated by $\Delta E \geq 400$ keV. Considering the MLD value of 137 keV obtained for this calculation — about three times less than the energy difference of the two levels of interest — the two states should be well separated, yet these difficulties persist.

To investigate this, first an analysis involving a total exchange of the wave functions has been carried out. The branching ratios are denoted as b_2 in Table 5.5 and the result is not entirely satisfactory. Then, a 10% mixing of the wave functions of the yrast and yrare $3/2^-$ states has been performed. The mixing percentage is based on the values of the transitions from the yrast $7/2^-$ level. All results are provided in Table 5.5 and the results from the mixed wave functions agree best

Table 5.4: Comparison between experimental and predicted branching ratios, b , of the γ rays in ^{61}Zn . Three shell-model calculations have been compared in this analysis. $b_{fp}^{Coulomb}$ and b_{fp} denote the branching ratios from the fp calculation with and without the Coulomb force included. b_{fpg} denotes ditto from the $f_{5/2}p_{9/2}$ calculation. Only transitions up to and including the state with $I^\pi = 19/2^-$ are included in the table. See text for more details.

E_x (keV)	E_γ (keV)	I_i^π	I_f^π	b_{exp}	$b_{fp}^{Coulomb}$	b_{fp}	b_{fpg}
88.8	89	$1/2_1^-$	$3/2_1^-$	1.0	1.0	1.0	1.0
123.9	35	$5/2_1^-$	$1/2_1^-$	n.o.	0.00	0.00	0.03
	124		$3/2_1^-$	1.0	1.0	1.0	0.97
419.2	296	$3/2_2^-$	$5/2_1^-$	0.06(1)	0.02	0.02	0.09
	331		$1/2_1^-$	0.11(1)	0.04	0.04	0.43
	419		$3/2_1^-$	0.83(2)	0.94	0.94	0.48
756.4	339	$5/2_2^-$	$3/2_2^-$	0.04(1)	0.05	0.05	0.01
	632		$5/2_1^-$	0.05(1)	0.06	0.07	0.04
	667		$1/2_1^-$	0.08(1)	0.00	0.00	0.00
	756		$3/2_1^-$	0.83(2)	0.89	0.88	0.95
997.7	241	$7/2_1^-$	$5/2_2^-$	n.o.	0.01	0.00	0.00
	578		$3/2_2^-$	0.04(1)	0.13	0.11	0.06
	873		$5/2_1^-$	0.70(4)	0.86	0.88	0.02
	997		$3/2_1^-$	0.25(5)	0.01	0.01	0.91
1266	268	$9/2_1^-$	$7/2_1^-$	n.o.	0.0	0.03	0.00
	510		$5/2_2^-$	n.o.	0.0	0.00	0.00
	1141		$5/2_1^-$	1.0	1.0	0.97	1.0
1403	137	$7/2_2^-$	$9/2_1^-$	n.o.	0.00	0.00	0.00
	405		$7/2_1^-$	n.o.	0.00	0.00	0.00
	647		$5/2_2^-$	0.24(2)	0.32	0.32	0.10
	984		$3/2_2^-$	0.25(4)	0.00	0.00	0.45
	1278		$5/2_1^-$	0.14(1)	0.07	0.05	0.14
	1403		$3/2_1^-$	0.37(3)	0.61	0.63	0.30
2003	600	$9/2_2^-$	$7/2_2^-$	n.o.	0.10	0.09	0.01
	738		$9/2_1^-$	0.06(1)	0.36	0.33	0.02
	1006		$7/2_1^-$	0.48(4)	0.22	0.27	0.02
	1246		$5/2_2^-$	0.46(4)	0.33	0.28	0.95
	1879		$5/2_1^-$	n.o.	0.00	0.02	0.00
2270	267	$11/2_1^-$	$9/2_2^-$	n.o.	0.00	0.00	0.00
	867		$7/2_2^-$	n.o.	0.00	0.00	0.03
	1005		$9/2_1^-$	0.27(3)	0.21	0.25	0.01
	1273		$7/2_1^-$	0.73(3)	0.79	0.75	0.96
2400	997	$9/2_1^+$	$7/2_2^-$	0.10(6)	—	—	—
	1403		$7/2_1^-$	0.85(15)	—	—	—
	2273		$5/2_1^-$	0.05(1)	—	—	—
2699	276	$11/2_2^-$	$7/2_3^-$	n.o.	0.00	0.00	—
	429		$11/2_1^-$	n.o.	0.00	0.00	0.00
	696		$9/2_2^-$	0.20(1)	0.17	0.19	0.01
	1433		$9/2_1^-$	0.80(1)	0.47	0.44	0.00
	1296		$7/2_2^-$	n.o.	0.34	0.33	0.68
	1701		$7/2_1^-$	n.o.	0.01	0.04	0.30

Table 5.4: Continued.

E_x (keV)	E_γ (keV)	I_i^π	I_f^π	b_{exp}	$b_{fp}^{Coulomb}$	b_{fp}	b_{fpg}
2799	100	13/2 ₁ ⁻	11/2 ₂ ⁻	n.o.	0.00	0.00	0.00
	529		11/2 ₁ ⁻	0.02(1)	0.00	0.00	0.00
	796		9/2 ₂ ⁻	n.o.	0.00	0.00	0.00
	1531		9/2 ₁ ⁻	0.98(1)	1.00	1.00	1.00
3244	1978	11/2 ₁ ⁺	9/2 ₁ ⁻	1.0	—	—	—
3336	937	13/2 ₁ ⁺	9/2 ₁ ⁺	0.85(7)	—	—	1.00
	1066		11/2 ₁ ⁻	0.15(1)	—	—	—
3461	662	13/2 ₂ ⁻	13/2 ₁ ⁻	n.o.	0.04	0.03	0.01
	762		11/2 ₂ ⁻	n.o.	0.05	0.04	0.01
	820		9/2 ₃ ⁻	n.o.	0.00	0.00	—
	1191		11/2 ₁ ⁻	n.o.	0.00	0.00	0.00
	1458		9/2 ₂ ⁻	0.55(2)	0.26	0.24	0.99
	2195		9/2 ₁ ⁻	0.45(2)	0.65	0.69	0.00
	3495(3)		34	11/2 ₃ ⁻	13/2 ₂ ⁻	n.o.	0.00
696	13/2 ₁ ⁻	n.o.	0.01		0.09	0.32	
796	11/2 ₂ ⁻	n.o.	0.03		0.02	0.00	
854	9/2 ₃ ⁻	n.o.	0.01		0.00	—	
1079	7/2 ₃ ⁻	n.o.	0.00		0.00	—	
1225	11/2 ₁ ⁻	n.o.	0.09		0.07	0.00	
1492	9/2 ₂ ⁻	n.o.	0.05		0.11	—	
2092	7/2 ₂ ⁻	n.o.	0.24		0.02	—	
2229(1)	9/2 ₁ ⁻	1.0	0.49		0.59	—	
3844	2497	15/2 ₁ ⁻	7/2 ₁ ⁻	n.o.	0.09	0.08	—
349	11/2 ₃ ⁻		n.o.	0.00	0.00	—	
383	13/2 ₂ ⁻		n.o.	0.00	0.00	0.00	
1046	13/2 ₁ ⁻		0.21(1)	0.12	0.16	0.00	
1145	11/2 ₂ ⁻		n.o.	0.01	0.01	0.00	
1572	11/2 ₁ ⁻		0.79(1)	0.88	0.83	1.0	
4264	928		15/2 ₁ ⁺	13/2 ₁ ⁺	n.o.	—	—
1019	11/2 ₁ ⁺	0.16(1)		—	—	1.0	
1466	13/2 ₁ ⁻	0.84(6)		—	—	—	
4309(3)	465	13/2 ₃ ⁻	15/2 ₁ ⁻	n.o.	0.04	0.04	—
	814		11/2 ₃ ⁻	n.o.	0.08	0.10	—
	848		13/2 ₂ ⁻	n.o.	0.01	0.01	—
	1510		13/2 ₁ ⁻	n.o.	0.04	0.08	—
	1610		11/2 ₂ ⁻	n.o.	0.01	0.01	—
	1668		9/2 ₃ ⁻	n.o.	0.19	0.20	—
	2039(1)		11/2 ₁ ⁻	1.0	0.38	0.36	—
	2306		9/2 ₂ ⁻	n.o.	0.24	0.17	—
	3043		9/2 ₁ ⁻	n.o.	0.02	0.04	—
	4415		151	17/2 ₁ ⁺	15/2 ₁ ⁺	n.o.	—
1079	13/2 ₁ ⁺	1.0	—		—	1.0	
4644	335	17/2 ₁ ⁻	13/2 ₃ ⁻	n.o.	—	0.00	0.00
	800		15/2 ₁ ⁻	n.o.	0.01	0.01	0.00
	1183		13/2 ₂ ⁻	n.o.	0.02	0.03	0.00
	1847		13/2 ₁ ⁻	1.0	0.97	0.95	1.0

Table 5.4: Continued.

E_x (keV)	E_γ (keV)	I_i^π	I_f^π	b_{exp}	b_{fp}	$b_{fp}^{Coulomb}$	b_{fpg}		
4915(3)	271	$15/2_3^-$	$17/2_1^-$	n.o.	0.00	0.00	0.03		
	606		$13/2_3^-$	n.o.	0.16	0.16	0.05		
	1071		$15/2_1^-$	n.o.	0.06	0.04	0.00		
	1420		$11/2_3^-$	n.o.	0.02	0.03	0.85		
	1454		$13/2_2^-$	n.o.	0.01	0.01	0.00		
	2116(1)		$13/2_1^-$	1.0	0.67	0.69	0.00		
	2216		$11/2_2^-$	n.o.	0.04	0.04	0.01		
	2645		$11/2_1^-$	1.0	0.04	0.02	0.07		
	5195		208	$17/2_2^-$	$15/2_3^-$	n.o.	0.01	0.01	0.00
			551		$17/2_1^-$	n.o.	0.02	0.02	0.27
886		$13/2_3^-$	n.o.		0.01	0.01	0.03		
1351		$15/2_1^-$	n.o.		0.04	0.08	0.01		
1733		$13/2_2^-$	1.0		0.70	0.64	0.06		
2396		$13/2_1^-$	n.o.		0.23	0.25	0.63		
5543	75	$19/2_1^-$	$17/2_3^-$	n.o.	0.00	0.00	0.00		
	348		$17/2_2^-$	n.o.	0.00	0.00	0.00		
	628		$15/2_3^-$	n.o.	0.00	0.00	0.00		
	899		$17/2_1^-$	0.27(7)	0.06	0.09	0.00		
	1698		$15/2_1^-$	0.73(7)	0.93	0.91	1.0		

Table 5.5: Comparison between experimental and predicted branching ratios and lifetimes for levels involving the yrare and yrast $3/2^-$ levels: b_1 , τ_1 shows the results for the basic fp shell-model calculation described in the text. In case of b_2 , τ_2 the wave functions of the yrast and yrare $3/2^-$ states have been exchanged, while b_3 , τ_3 presents the results for two-state mixing calculation of the two $3/2^-$ states. In this calculation the yrast state consists to 90% of the yrast wave functions, the remaining 10% originates from the yrare state, and vice versa.

E_x (keV)	E_γ (keV)	I_i^π	I_f^π	b_{exp}	b_1	b_2	b_3	τ_1	τ_2	τ_3
89	89	$1/2_1^-$	$3/2_1^-$	1.00	1.00	1.00	1.00	0.84 ns	27 ns	0.83 ns
124	124	$5/2_1^-$	$3/2_1^-$	1.00	1.00	1.00	1.00	5.6 ns	26 ns	4.7 ns
	35		$1/2_1^-$	n.o.	0.00	0.00	0.00			
756	756	$5/2_2^-$	$3/2_1^-$	0.83(2)	0.89	0.79	0.94	0.83 ps	1.2 ps	0.62 ps
	667		$1/2_1^-$	0.08(1)	0.00	0.01	0.00			
	632		$5/2_1^-$	0.05(1)	0.06	0.09	0.05			
	339		$3/2_2^-$	0.04(1)	0.05	0.11	0.01			
	998		997	$7/2_1^-$	$3/2_1^-$	0.26(2)	0.01	0.69	0.23	6.2 ps
873	$5/2_1^-$	0.69(2)	0.86		0.31	0.68				
578	$3/2_2^-$	0.04(1)	0.13		0.00	0.09				
241	$5/2_2^-$	n.o.	0.01		0.00	0.00				
1403	1403	$7/2_2^-$	$3/2_1^-$	0.37(15)	0.61	0.01	0.60	0.65 ps	1.3 ps	0.66 ps
	1278		$5/2_1^-$	0.14(3)	0.07	0.13	0.07			
	984		$3/2_2^-$	0.25(7)	0.00	0.21	0.00			
	647		$5/2_2^-$	0.24(5)	0.32	0.65	0.33			
	405		$7/2_1^-$	n.o.	0.00	0.00	0.00			
	137		$9/2_1^-$	n.o.	0.00	0.00	0.00			

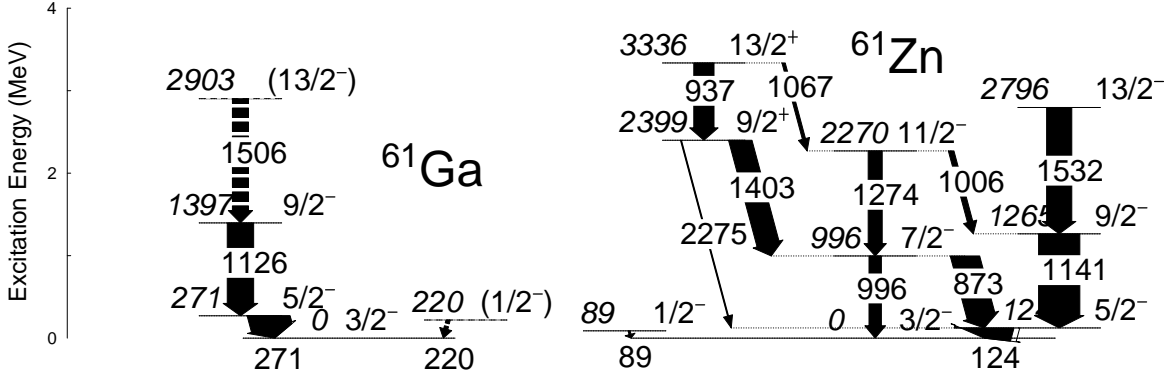


Figure 5.4: The mirror transitions in both ^{61}Ga and ^{61}Zn are illustrated. According to isospin symmetry the two nuclei should reveal almost identical level schemes. See text for details.

with the experimentally obtained values. However, some discrepancies still remain for the branching ratios of the $7/2_2^- \rightarrow 3/2_1^-$ and the $7/2_2^- \rightarrow 5/2_1^-$ transitions. These differences are of minor relevance due to the experimental difficulties related to the doublet structure of the 997 keV and the 1403 keV transitions, which lead to large uncertainties of their relative strengths. It is interesting to note that Ref. [22] reports on a similar case ($\Delta E \gg \text{MLD}$) for both the GXPF1 and other fp -shell interactions.

Table 5.5 also includes the calculated lifetimes of the levels. The lifetimes are experimentally unknown except for the estimation of $\tau \approx 8$ ns for the 124 keV state derived in Paper II and Sec. 3.4.1. This estimate is also in line with the 10% two-state mixing calculation of the two $3/2^-$ states.

5.3 Mirror Energy Differences

As mentioned in Sec. 4.3 mirror nuclei are pairs of nuclei which are expected to have very similar decay schemes since the strong force is nearly charge independent. This means that ^{61}Zn and ^{61}Ga should decay in a very similar way. The full level schemes from the current analysis are presented in Fig. 3.1 and Fig. 3.2. In Fig. 5.4 a zoomed version is presented. Here the mirror transitions in both nuclei are focused upon.

As can be seen in the figure some large discrepancies occur, and it is common to illustrate the so called Mirror Energy Differences (MEDs, see Sec. 4.3) in a MED diagram. The MEDs are plotted as a function of the spin J of the level in Fig. 5.5. In the figure also different contributions, described in Sec. 4.3, to the MED are illustrated. If only including the V_{CM} part the obtained contribution is not sufficient to explain the experimentally obtained MED. Since the largest MED values are obtained for the $1/2^-$ and the $5/2^-$ states, both of which involve mainly single-particle excitations from the $2p_{3/2}$ orbital, the electromagnetic spin orbit effect may play a significant role, as discussed in Sec. 4.3. Adding the V_{CIs} term to the Coulomb multipole term gives a result that is very close to the experimental results. This indicates a large contribution of the V_{CIs} term although the contributions from the other parts of the Coulomb monopole effect cannot be neglected as contributions

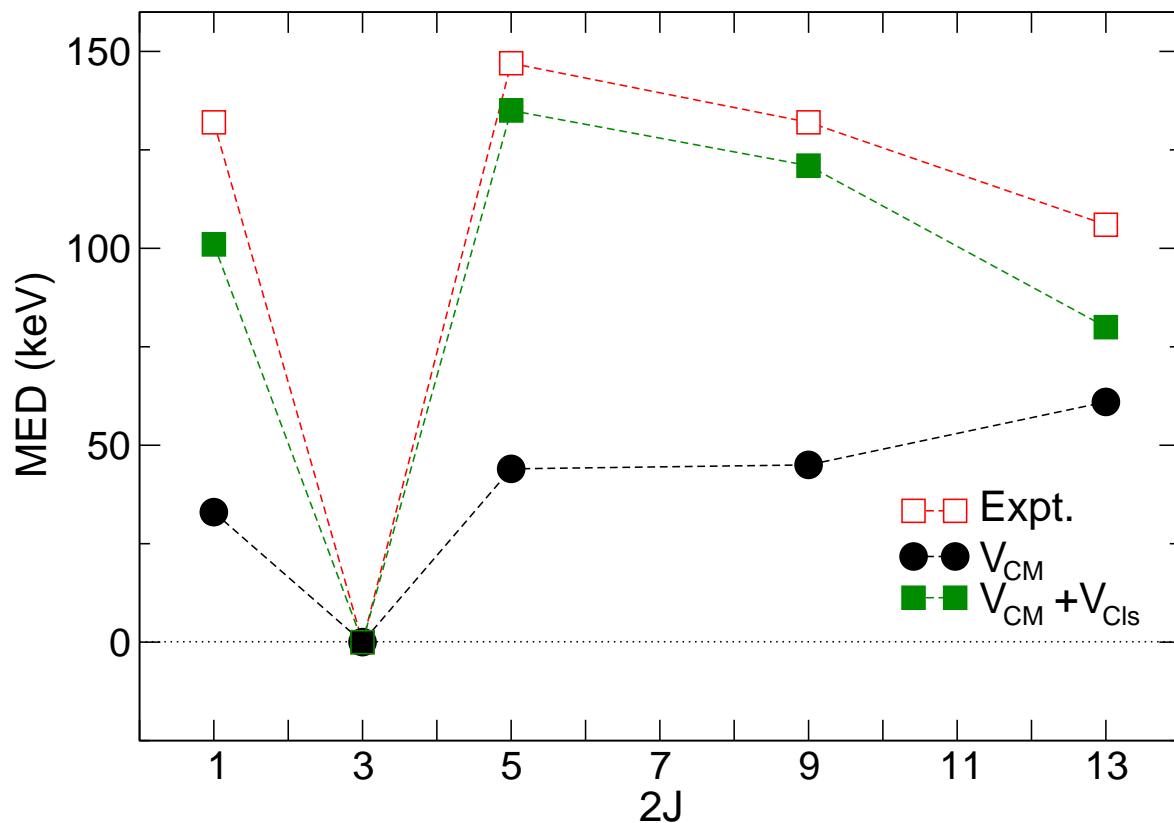


Figure 5.5: The MED values including different contributions plotted as a function of spin J . See text for details.

from different parts of this may be large even if they cancel out in the end.

To my discussion above, however, the analysis and results from Ref. [38] should be added. In this paper yet another term is added to the mirror energy differences. This term takes into account the effect of an additional Coulomb monopole term, $V_{\ell\ell}$, describing the effect of the monopole electromagnetic field on the single particle energies for neutrons and protons, respectively. More details about this can be found in Refs. [38, 39]. When adding the contribution of the term to the calculations the resulting MED, including the V_{CM} , V_{Cl_s} , and $V_{\ell\ell}$ terms, only accounts for around 50% of the experimentally obtained difference. However, according to the discussion in the paper the difference could be accounted for by the Coulomb monopole radial term, V_{Cr} .

The $V_{\ell\ell}$ term is also included in [34], here referred to as $V_{Cr}^{(b)}$. The two terms are, however, interpreted slightly differently which results in different contributions to the full MED. In Ref. [34] the sum of the V_{CM} , V_{Cl_s} , and $V_{Cr}^{(b)}$ terms results in an MED which is some 30% larger than was experimentally found for the $I^\pi = 5/2$ and $9/2$ but fits well with the experimental results for the $1/2$ and $13/2$ states. The discussion about the $V_{\ell\ell}$, or $V_{Cr}^{(b)}$, term is ongoing and will not be treated in more depth here.

5.4 Prompt Proton Decay

When looking at the experimentally obtained level scheme for ^{61}Zn in Fig. 5.4, the bottom of the yrast sequence with its $5/2^-$ band head is clearly indicated with very intense transitions between the levels. The second most intense transitions are the 937 keV, $13/2^+ \rightarrow 9/2^+$, the 1403 keV, $9/2^+ \rightarrow 7/2^-$, and the 873 keV, $7/2^- \rightarrow 5/2^-$, transitions. Considering the low spins of the involved levels and the intense transitions, and keeping the mirror symmetry in mind it is surprising to see that the corresponding levels are absent in the ^{61}Ga nucleus. One possible explanation for this would be a prompt proton decay from the $1g_{9/2}$ dominated $9/2^+$ state into the ground state of ^{60}Zn . Using mirror symmetry arguments to estimate the excitation energy of the $9/2^+$ level (approximately 2.4 MeV) and knowing binding energies (last proton bound by only 190(50) keV) gives a Q -value of about 2.2 MeV for the prompt proton decay. This value compares well with previously found prompt proton decays [40, 41] in the mass $A = 60$ region.

In addition to these encouraging facts one can draw conclusions from the two main factors that affect the probability to emit a prompt proton. These factors are the probability of the proton to tunnel and the overlap of the initial and final wave functions of the “mother” and “daughter” nucleus. The former depends on the orbital angular momentum that the proton has to carry, as this effects the barrier height, and the energy (Q value) of such a decay. Comparing with the numbers obtained for ^{58}Cu [40] with $Q_p \approx 2.3$ and orbital angular momentum of $\ell = 4$ [42] we expect the decay constant related to plain tunnelling of the prompt proton in the two cases to be about the same size. However, as mentioned above the decay probability also depends on the overlap of the wave functions. In ^{58}Cu the overlap is not expected to be very large due to the configuration behind the two states between which the decay takes place. The initial level is expected [43] to have two proton and two neutron holes in the $1f_{7/2}$ orbital and one proton and one neutron in the $1g_{9/2}$ orbital. On the other hand it seems reasonable to assume that the $9/2^+$ state in the daughter nucleus ^{57}Ni is caused by a single neutron in the $1g_{9/2}$ orbital with completely filled inner orbitals. The difference in configuration, which also is related to the shape, makes the decay probability decrease by about a factor of 1000 [44].

In the case of ^{61}Ga the configuration of the $9/2^+$ excited state is two protons and two neutrons outside doubly magic ^{56}Ni core and additional to that one proton in the $1g_{9/2}$ orbital. The ground state in the daughter nucleus ^{60}Zn has the same configuration except for the $1g_{9/2}$ proton. Such a similar configuration must mean a good overlap between the initial and final wave functions. The similarities in wave functions will make a prompt proton decay in ^{61}Ga unique as no structural hindrance appears in the decay, resulting in a much higher decay probability than for the prompt proton emitters observed so far.

Chapter 6

Conclusions and Outlook

From the experiment at the Oak Ridge National Laboratory excited states in both ${}^{61}_{30}\text{Zn}_{31}$ and ${}^{61}_{31}\text{Ga}_{30}$ have been found. From the ${}^{61}_{31}\text{Ga}_{30}$ nucleus four excited levels have been identified for the first time via the γ -ray transitions between the states. In ${}^{61}_{30}\text{Zn}_{31}$ the previously determined levels scheme has been extended resulting in almost 70 transitions arranged in a firmly determined scheme. The spin and parity assignments are based on angular distribution ratios. Spins and parities determined in the current analysis affect corresponding assignments of the levels in the the previously identified superdeformed band. This finding suggests the need for more experimental information about the superdeformed bands in this nucleus.

Information about the excited states in both mirror nuclei provides the possibility to investigate the mirror energy differences (MED). These differences can be used to investigate which parameters play a significant role for the unique level energies in different nuclei. The MED values can be separated into different contributions; not only a Coulomb multipole and monopole part but the latter can also be further divided into sub sections such as radial, electromagnetic spin-orbit, and single particle contributions. The different MED contributions as well as the level energies can be calculated using large-scale shell-model calculations.

Two interactions are of interest for this mass region: the GXPF1 and the, yet unreleased, $f_{5/2}pg_{9/2}$ interaction. Neither is successful in fully describing the experimental data in ${}^{61}_{30}\text{Zn}_{31}$. This implies that further development of the shell model calculations in this mass region is required. Ideally an interaction including both the $1f_{7/2}$ and the $1g_{9/2}$ orbitals should be developed. Such an interaction would be able to reproduce both the low spin states, which are strongly dependent on the inclusion of the $1f_{7/2}$ orbital, and high spin states, which require the inclusion of the $1g_{9/2}$ orbital. At present such an interaction is not feasible due to the centre of mass problems arising when including both of these in the calculation.

The $B(M1)$, $B(M2)$, $B(E1)$, and $B(E2)$ values obtained from the shell model calculations were used to compare experimental and calculated branching ratios. In the current analysis the general agreement is good. However, difficulties in fully separating the yrast and yrare $3/2^-$ levels have been observed. A two-state mixing calculation suggests a 10% mixing of the states.

Finally, mirror symmetry arguments suggest a possible prompt proton decay from the $9/2^+$ level in the ${}^{61}_{31}\text{Ga}_{30}$ nucleus, due to expected but experimentally not observed transitions. The existence of such a proton decay would be unique due

to the large overlap in initial and final wave functions of the states involved in the transitions. The overlap would result in no structural hindrance in the transition in contrast to prompt proton transitions observed so far.

Obviously the interesting features of the prompt proton decay together with the firmly determined level scheme of ${}^{61}_{30}\text{Zn}_{31}$ make further investigations of ${}^{61}_{31}\text{Ga}_{30}$ desirable. The experiment described in this thesis carried out at the Argonne National Laboratory will, with the charged particle detector LuSiA around the target position, hopefully enable experimental observation of this decay. Furthermore, LuSiA can in principle, with its fine pixilation, be used to measure the angular distribution of the emitted protons, resulting in information about the involved tunnelling process.

Another experiment is also currently being planned. This experiment will take place at the Oak Ridge National Laboratory using an identical set-up as for the experiment from ORNL described in this thesis. The only difference will be a Silicon CD detector inside the target chamber to detect possible prompt protons. The aim is to increase the statistics of the current data set to observe more transitions in ${}^{61}_{31}\text{Ga}_{30}$ and to be able to place all of the transitions currently assigned to this nucleus in the level scheme. The identification of more transitions would also be desirable to further extend the mirror analysis between the nuclei in this mirror pair and similarly further explore the limits and possibilities of current interactions in the shell model calculations.

Acknowledgements

First I would like to thank my advisor Dirk Rudolph, without whom I would not have been able to publish “my” two papers nor write this licentiate thesis. I will never stop being fascinated over your joy for Physics and your obsession for ice-cream nor being amazed over your German efficiency.

I also would like to thank Professor Claes Fahlander for giving me the opportunity to join the Lund Nuclear Structure Group and Professor Emeritus Hans Ryde for his constant engagement and for still going strong. I feel grateful to you both for always showing interest in my work and always encouraging me.

My daily gratitude goes to Emma Johansson, with whom I have shared office, flights, trains, cars and hotels since I arrived to this department – it has been a pleasure. Also thanks to Diego A. Torres and Andreas Ekström for making our new office an enjoyable place to work in. I am equally thankful to the rest of the people working in and together with the Nuclear Structure Group in Lund that have helped me and showed interest in my work.

I am also grateful to all the people working at the Oak Ridge National Laboratory and the Argonne National Laboratory for helping out and making our experiments successful. In particular thanks to Carl Gross who helped out during both of my visits to the laboratory in Oak Ridge.

Thanks to The Royal Physiographic Society in Lund which financially has supported one of my journeys to the U. S.

Last but not least I want to thank My, Bellen, and Aisa for supporting me through my abstract work. I love you! ♥

Bibliography

- [1] L-L. Andersson, Master Thesis, Lund University, LUNFD6/(NFFR-5022)1-47/(2004).
- [2] L-L. Andersson *et al.*, Phys. Rev. C **71**, 011303(R) (2005).
- [3] L-L. Andersson *et al.*, Eur. Phys. J. A **30**, 381 (2006).
- [4] E. K. Johansson, Master thesis, Lund University, LUNFD6/(NFFR-5023)1-47/(2004).
- [5] C.J. Gross *et al.*, Nucl. Instrum. Meth. Phys. Res. A **450**, 12 (2000).
- [6] I. -Y. Lee, Nucl. Phys. A **520**, 641c (1990).
- [7] D. G. Sarantites *et al.*, Nucl. Instrum. Meth. Phys. Res. A **530**, 473 (2004).
- [8] D. G. Sarantites *et al.*, Nucl. Instrum. Meth. Phys. Res. A **381**, 418 (1996).
- [9] <http://www.chemistry.wustl.edu/dgs/NeutronShell/NeutronShell.html>
- [10] E. K. Johansson, Licentiate Thesis, Lund University, LUNFD6/(NFFR-3099)/1-74/(2006).
- [11] W. R. Leo, “Techniques for Nuclear and Particle Physics Experiments”, Springer-Verlag, Würtzberg, (1994).
- [12] C. N. Davids *et al.*, Nucl. Instrum. Meth. Phys. Res. B **70**, 358 (1992).
- [13] G. D. Alton, J. R. Beene, J. Phys. G: Nucl. Part. Phys. **24**, 1347 (1998).
- [14] <http://www.phy.anl.gov/fma/fmasch2.gif>
- [15] D. A. Torres Galindo, private communication.
- [16] C. Andreoiu, “Superdeformation and Prompt Proton Decays in ^{59}Cu ”, Licentiate Thesis, Department of Physics, Lund University, (2000).
- [17] M. R. Bhat, Nucl. Data Sheets **88**, 417 (1999).
- [18] O. Izotova *et al.*, Phys. Rev. C **69**, 037303 (2004).
- [19] C. -H. Yu *et al.*, Phys. Rev. C. **60**, 031305 (1999).

- [20] T. Yamazaki, Nucl. Data A **3**, 1 (1967).
- [21] <http://www.phys.jyu.fi/research/gamma/publications/akthesis/node7.html>
- [22] E. K. Johansson *et al.*, Eur. Phys. J, **A 27**, 157 (2006).
- [23] R. B. Schubank, J. A. Cameron, and V. P. Janzen, Phys. Rev. C **40**, 2310 (1989).
- [24] K. S. Krane, “Introductory Nuclear Physics”, John Wiley & Sons, New York, (1988).
- [25] E. Caurier, shell model code ANTOINE, IRES, Strasbourg 1989-2002.
- [26] E. Caurier, F. Nowacki, Acta Phys. Pol. **30**, 705 (1999).
- [27] A. Poves and A. P. Zuker, Phys. Rep. **70**, 235 (1981).
- [28] A. Poves, J. Sánchez-Solano, E. Caurier, and F. Nowacki, Nucl. Phys. **A694**, 157 (2001).
- [29] M. Honma, T. Otsuka, B. A. Brown, and T. Mizusaki, Phys. Rev. C **69**, 034335 (2004).
- [30] M. Honma, T. Otsuka, B. A. Brown, and T. Mizusaki, Phys. Rev. C **65**, 061301 (2002).
- [31] M. Honma, T. Otsuka, B. A. Brown, and T. Mizusaki, Eur. Phys. J. A **25**, s01, 499 (2005).
- [32] J. B. Ehrman, Phys. Rev. **81**, 412 (1951).
- [33] R. G. Thomas, Phys. Rev. **88**, 1109 (1952).
- [34] J. Ekman, C. Fahlander, and D. Rudolph, Mod. Phys. Lett. A **20**, No. 39, 2977 (2005).
- [35] A. P. Zuker *et al.*, Phys. Rev. Lett. **89**, 142502 (2002).
- [36] J. Ekman, PhD thesis, Lund University, ISBN 91-628-6061-5 (Intellecta DocuSys AB, Lund, 2004)
- [37] R. du Rietz *et al.*, Phys. Rev. Lett. **93**, 222501 (2004).
- [38] M. A. Bentley and S. M. Lenzi, Prog. Part. Nucl. Phys. (2006).
- [39] J. Dufflo and A. P. Zuker, Phys. Rev. C **66**, 051304(R) (2002).
- [40] D. Rudolph *et al.*, Phys. Rev. Lett. **80**, 3018 (1998).
- [41] D. Rudolph *et al.*, Phys. Rev. Lett. **89**, 022501 (1998).
- [42] D. Rudolph *et al.*, Eur. Phys. J. A **14**, 137 (2002).

- [43] A. V. Afanasjev, I. Ragnarsson, and P. Ring, *Phys. Rev. C* **59**, 3166 (1999).
- [44] D. S. Delion, R. J. Liotta, and R. Wyss, *Phys. Rev. C* **68**, 054603 (2003).

Paper 1

Identification of excited states in $^{61}_{31}\text{Ga}_{30}$: Mirror nuclei in the upper fp shell

L.-L. Andersson, E. K. Johansson, J. Ekman, D. Rudolph, R. du Rietz, and C. Fahlander
Department of Physics, Lund University, S-22100 Lund, Sweden

C. J. Gross, P. A. Hausladen, and D. C. Radford
Physics Division, Oak Ridge National Laboratory, Oak Ridge, Tennessee 37830

G. Hammond
School of Chemistry and Physics, Keele University, Keele, Staffordshire, ST5 5BG, United Kingdom
 (Received 6 September 2004; published 24 January 2005)

In the fusion-evaporation reaction $^{40}\text{Ca} + ^{24}\text{Mg}$ at 104 MeV beam energy, excited states have been observed for the first time in the isotope $^{61}_{31}\text{Ga}_{30}$. The experimental setup comprised the Ge array CLARION, a recoil mass spectrometer and, in its focal plane, an ionization chamber. Five transitions in ^{61}Ga are identified, out of which a cascade of three transitions has been established by means of recoil- $\gamma\gamma$ coincidences. The strong transitions at 271 keV in ^{61}Ga and 124 keV in ^{61}Zn are viewed as the “mirror” $5/2^- \rightarrow 3/2^-$ ground-state transitions. The rather large energy difference of 150 keV is suggested to arise from Coulomb monopole contributions. Shell-model calculations support this interpretation.

DOI: 10.1103/PhysRevC.71.011303

PACS number(s): 21.60.Cs, 23.20.En, 23.20.Lv, 27.40.+z

The proton and the neutron can be viewed as two states of the nucleon, characterized by an isospin quantum number [1]. Assuming isospin symmetry, mirror nuclei, i.e., pairs of nuclei where the number of protons and neutrons are interchanged, would reveal identical level schemes. However, the electromagnetic interaction between protons obviously breaks this symmetry, which leads to small differences between level energies of analog states in pairs of mirror nuclei—the so-called mirror energy differences (MED).

During the past decade the experimental knowledge of $T = 1/2$ and $T = 1$ mirror nuclei in the $1f_{7/2}$ shell has increased substantially (see, e.g., Refs. [2–8]). This continuing progress has been accompanied with detailed theoretical studies and refinements, for example, in Refs. [4,6,7,9]. The observed MED values, typically 10–100 keV, are readily explained by Coulomb monopole effects—e.g., slightly different shapes or radii—and Coulomb multipole effects, which are sensitive to the alignment of pairs of protons.

In nuclei close to the center of the $1f_{7/2}$ shell, Coulomb monopole effects arise from significant $2p_{3/2}$ admixtures into the ground state wave functions, which decrease gradually towards terminating states. In nuclei below and above the rather well isolated $1f_{7/2}$ shell, differences in configurations of adjacent states may cause significant changes in Coulomb monopole contributions manifested as sudden changes in observed MED diagrams. One such example is the ~ 300 keV drop in MED between the $11/2^-$ and $13/2^-$ states in the $A = 35$ and $A = 39$ mirror systems, which can be explained by radial effects as well as a hitherto overlooked electromagnetic spin-orbit contribution [10]. The latter is sensitive to single-particle excitations between orbits of opposite spin-orbit couplings and may hence reoccur in the upper fp shell, i.e., in the $T_z = \pm 1/2$, $A = 57, 59, 61$ mirror pairs. While some basic knowledge of the neutron-deficient nuclei ^{57}Cu [11] and ^{59}Zn [12] exists, only ground-state half-life measurements

based on fragmentation reactions [13,14] and recent β -decay studies [15,16] are available for ^{61}Ga .

In the present paper we report on the observation of excited states in ^{61}Ga and compare its excitation scheme to the rather well known mirror nucleus ^{61}Zn [17–19]. Interestingly, Ref. [16] showed that the $3/2^-$ ground state of ^{61}Ga is bound by only 190(50) keV, which can imply particle-decaying excited states as well.

The experiment was conducted at the Holifield Radioactive Ion Beam Facility at Oak Ridge National Laboratory. In fusion-evaporation reactions of a ^{40}Ca beam at 104 MeV, impinging on a 99.92% isotopically enriched ^{24}Mg target foil of thickness 0.3 mg/cm^2 , ^{64}Ge compound nuclei are formed. The $^{61}_{31}\text{Ga}_{30}$ nuclei are then produced via the evaporation of one proton and two neutrons.

The Ge detector array CLARION [21] was used to detect the γ radiation at the target position. At the time of the experiment CLARION comprised ten clover detectors. These detectors were placed in a three-ring construction at 90° , 132° , and 154° with respect to the beam axis. The rings consisted of five, three, and two clover detectors, respectively. Each clover contains four Ge crystals, each of which is electrically twofold segmented. This construction allows for add-back and high accuracy event-by-event Doppler corrections.

Add-back is used to reconstruct the energy of Compton scattered γ rays. It is performed if (i) two γ rays are detected within the same clover with a time separation of 30 ns or less and (ii) if the individual energy deposited exceeds a chosen add-back threshold of 20 keV. For a γ -ray energy of ~ 1 MeV these corrections resulted in a 25% increase in statistics.

As the recoiling nuclei are moving at some 4.3% of the speed of light, the γ -ray energies have to be corrected to account for the Doppler shift and broadening. These corrections require a determination of the emission angles of the γ rays with respect to the velocity vectors of the recoiling

nuclei. The latter are well defined for the residues of interest, as the recoils have to lie in a narrow cone around the beam axis to enter the recoil mass spectrometer (see details in the next paragraph). Due to the physical size of the Ge detectors, the angle at which a γ ray is detected usually differs slightly from the nominal angle at which the detector is placed. Using the side channel information of the segmented crystals, more precise emission angles can be derived [20], which results in a more precise determination of the emitted γ -ray energy. Since the velocity of a recoiling nucleus depends on its kinetic energy, which is measured in the ionization chamber (see below), an event-by-event velocity correction can be performed to further improve the energy resolution of the γ rays. The combination of γ -detection angle and recoil velocity corrections leads to a $\sim 30\%$ ($\sim 10\%$) improvement of the full width at half maximum (FWHM) of the peaks in the γ -ray spectra in a single crystal at 90° (154°).

After the particle evaporation and prompt γ -decay processes, the reaction products are recoiling from the thin target into a recoil mass spectrometer (RMS) before finally being stopped in an ionization chamber (IC). The RMS [21] separates the recoiling nuclei in mass-to-charge ratio A/Q , where Q represents a nominal charge state of the ions. The RMS was run in converging mode and tuned to center recoils of mass $A = 62$ with charge state $Q = 18.1$ and recoil energy $E = 58.2$ MeV. The noninteger value of Q implies that the $A = 62$ recoils reach the focal plane slightly to the right of the center. Since the RMS has an A/Q acceptance greater than $\pm 4\%$ this setting also allowed recoils of mass $A = 61$ to impinge on the left-hand side of the A/Q dispersed focal plane.

The horizontal position (the A/Q value) is determined by a position-sensitive grid placed inside the IC [21]. The recoiling $A = 61$ nuclei are well separated from scattered beam and other recoiling nuclei using a two-dimensional gate in a plot showing the position of the recoils in the IC versus the total energy deposited in the left-hand side of the IC.

The anode of the position-sensitive IC is split into three segments along the beam direction. The IC was filled with isobutane gas at a pressure of 16.5 torr to put the recoils to a complete stop and to let the energy loss in the three parts of the IC be approximately equal. According to the Bethe-Bloch formula, the fractional energy loss in the three parts of the anode in the IC is proportional to the Z value, and inversely proportional to the total kinetic energy of the recoils. The latter dependence can easily be removed by mathematical procedures, which are described in detail in Ref. [22].

In the next step the modified energy-loss signals, or combinations of these, have been correlated with γ rays detected in CLARION. A number of energy-loss spectra have been studied in coincidence with the known, intense, and clean $A = 61$ transitions at 970 keV (^{61}Cu) and 124 keV (^{61}Zn) [17,18]. A comparison of these spectra resulted in an approach using the ratio between the energy loss in the first and the third part, R_{13} , which improved the Z separation with respect to the traditional usage of the sum of the energy losses in the first and the second part of the IC [21,22].

There are three isotopes of mass $A = 61$ produced in the present fusion-evaporation reaction; $^{61}_{29}\text{Cu}_{32}$, $^{61}_{30}\text{Zn}_{31}$, and $^{61}_{31}\text{Ga}_{30}$. Each of these will peak at slightly different values of

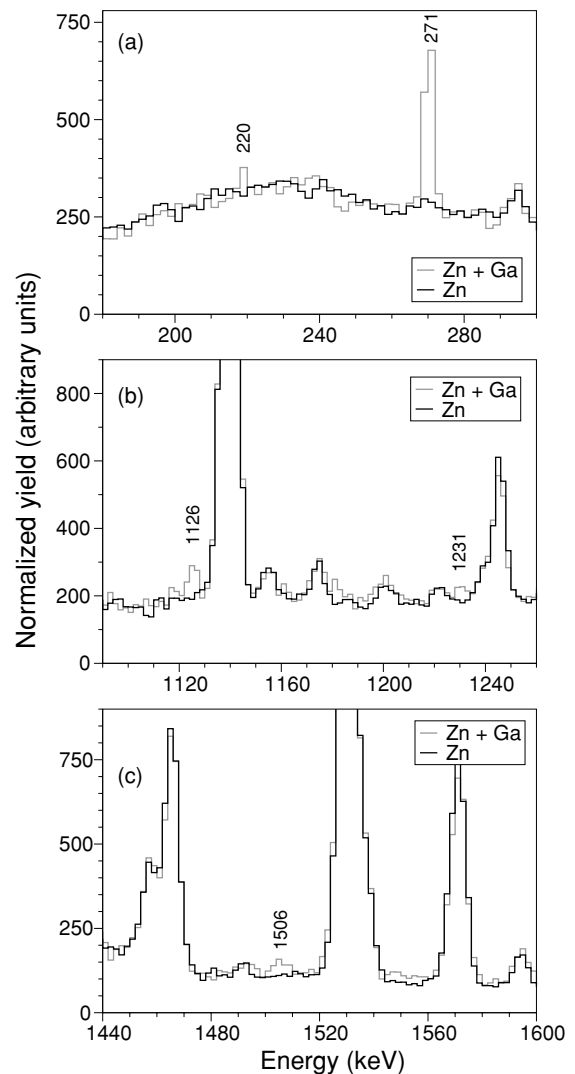


FIG. 1. Normalized γ -ray spectra containing transitions from ^{61}Ga and ^{61}Zn (gray) and only ^{61}Zn (black). The three panels show different energy regions. Energy labels are in keV.

R_{13} . By incrementing γ -ray spectra containing recoils with R_{13} restricted around the known peak positions for ^{61}Cu and ^{61}Zn and performing a careful fractional subtraction, it is possible to obtain clean ^{61}Cu and ^{61}Zn γ -ray spectra. The black γ -ray spectra in Fig. 1(a–c) show parts of the clean ^{61}Zn spectrum. The overlaid gray spectrum in Fig. 1 is correlated with a range of R_{13} values expected for ^{61}Ga . Even for this spectrum, small “contaminations” from ^{61}Cu have been subtracted, and any difference between the gray and the black spectrum will hence indicate the candidates for γ -ray transitions from ^{61}Ga . Figure 1(a) comprises the most prominent candidate at 271 keV. Similarly, four weak transitions can be distinguished at 220, 1126, 1231, and 1506 keV.

Figure 2 proves that the peak at 271 keV indeed belongs to ^{61}Ga . The energy loss ratio R_{13} is shown for the 271 keV line and compared to those of the previously mentioned transitions from ^{61}Cu and ^{61}Zn . It reaches its maximum at a value of R_{13} expected for $Z = 31$, i.e., Ga. Table I provides the energies

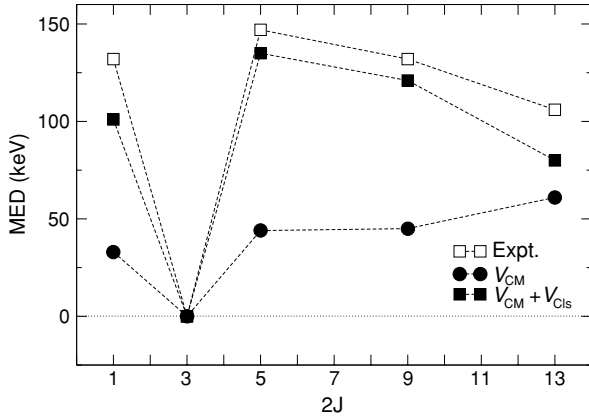


FIG. 4. MED diagram of the $A = 61$ mirror nuclei. Open squares indicate experimental data; filled circles indicate calculated MED values including the V_{CM} component; and filled squares indicate MED values including the $V_{\text{CM}} + V_{\text{Cls}}$ component. The error bars are smaller than the symbols. See text for details.

Predictions from large-scale shell-model calculations using the shell-model code ANTOINE [25,26] are included in Fig. 4. The calculations were performed in the full fp space containing the $1f_{7/2}$ orbit below and the $2p_{3/2}$, $1f_{5/2}$, and $2p_{1/2}$ orbits above the $N = Z = 28$ shell closures. The configuration space was truncated to allow up to three particle excitations from the $1f_{7/2}$ shell into the upper fp shell. The calculations were performed using the GXPF1 [27,28] with Coulomb interaction, where the two-proton matrix elements are constructed by adding harmonic oscillator Coulomb matrix elements to the bare two-body matrix elements. The interaction used is well adjusted not only for nuclei in the $1f_{7/2}$ shell but also in particular for nuclei at or beyond the $N = Z = 28$ shell closure, i.e., the upper fp shell.

In the first calculation identical single-particle energies for protons and neutrons were used to estimate the Coulomb multipole component, V_{CM} , which takes the effect from the alignment of proton pairs into account. The result is shown as filled circles in Fig. 4. It is seen that the correct sign of the MED values is reproduced, although the predicted MED values are typically 50 to 100 keV smaller than the experimental MED values. These discrepancies may be the result of Coulomb monopole effects, V_{cm} , which are not yet included in the shell-model calculation.

Since excitations from the $2p_{3/2}$ orbit to the $1f_{5/2}$ and $2p_{1/2}$ orbits are present in the formation of the observed states, the electromagnetic spin-orbit effect, V_{Cls} , comes naturally to mind as a possible explanation. The contribution from the electromagnetic spin-orbit interaction to the single-particle energies can be written as [29]

$$V_{\text{Cls}} = (g_s - g_l) \frac{1}{2m_N^2 c^2} \left\langle \frac{1}{r} \frac{dV_C(r)}{dr} \right\rangle (\vec{l} \cdot \vec{s}), \quad (1)$$

where $g_s = 5.586$ (-3.828) and $g_l = 1$ (0) are the free gyromagnetic factors for the proton (neutron) and m_N is the nucleon mass. In the present work, V_{Cls} was calculated using harmonic oscillator single-particle wave functions and

TABLE II. Contribution to the single-particle energies in keV arising from the electromagnetic spin-orbit effect [cf. Eq. (1)].

	$1f_{7/2}$	$2p_{3/2}$	$1f_{5/2}$	$2p_{1/2}$
Protons	-49	-16	66	32
Neutrons	41	13	-55	-26

assuming a charge distribution given by a Fermi distribution with a surface diffuseness parameter and radius equal to 0.5 fm and $1.2 \cdot A^{1/3}$ fm, respectively. The contributions are given in Table II, and the result from a shell-model calculation, where the original single-particle energies have been modified according to Eq. (1), is shown in Fig. 4 as filled squares.

Obviously, the agreement with the experimental MED values has improved considerably. Other Coulomb monopole contributions such as radial effects—for example, differences in radii between ground states and excited states—appear at first glance to be less important when describing the MED diagram of the $A = 61$ mirror pair. Nevertheless, these effects can be present and large, though they would have to, at least, partially cancel out each other. Naively, one would expect a positive contribution from radial effects for the $5/2^-$ states in both the $A = 57$ and $A = 61$ mirror systems, since these states are formed by exciting a proton (neutron) from a low $l = 1$ ($2p_{3/2}$) orbit to a high $l = 3$ ($1f_{5/2}$) orbit in the $T_z = -1/2(+1/2)$ member. Indeed, the MED value of 260 keV for the $5/2^-$ states in the $A = 57$ mirror nuclei could indicate that such effects are present, because only some 160 keV are accounted for in shell-model calculations including V_{CM} and V_{Cls} , which contribute with $\sim 25\%$ and $\sim 75\%$, respectively. The fact that the $5/2^-$ states in ^{57}Cu and ^{61}Ga are unbound with 333(19) keV and 79(54) keV, respectively, further complicates the situation. One could finally add that in the $A = 59$ mirror pair all Coulomb monopole effects are suppressed because of a high degree of configuration mixing of both proton and neutron excitations in both ^{59}Zn and ^{59}Cu [12]. A full assessment of radial Coulomb monopole contributions to MED diagrams in the upper fp shell thus requires a forthcoming detailed and thorough theoretical investigation.

Last but not least, it is intriguing to take a closer look at the level schemes in Fig. 3. There is no apparent hint of the $9/2^+ \rightarrow 7/2^- \rightarrow 5/2^-$ (1403–873 keV in ^{61}Zn) or the $9/2^+ \rightarrow 7/2^- \rightarrow 3/2^-$ (1403–996 keV in ^{61}Zn) sequence in ^{61}Ga in the present data set, even though the branch through the 2399 keV $9/2^+$ state in ^{61}Zn has about the same intensity as the $13/2^- \rightarrow 9/2^- \rightarrow 5/2^-$ cascade. A possible explanation for the nonobservation of γ -rays decaying from a $9/2^+$ state in ^{61}Ga is a $1g_{9/2}$ proton decay of that level into the ground state of ^{60}Zn . Using $E_x(9/2^+) \sim 2.4$ MeV, together with the known binding energy, one can estimate $Q_p \sim 2.2$ MeV for such a decay, which is very similar to the energetics of $1g_{9/2}$ prompt proton decays from deformed to near spherical states in the mass region [30]. In the present case, however, no significant shape change should be associated with the decay, which further enhances its likelihood.

To summarize, we have observed excited states in ^{61}Ga via recoil- γ coincidences. Three transitions were found to

be in coincidence. Pronounced energy differences in $A = 61$ analog states can to a large extent be explained by a combination of the multipole Coulomb term and the electromagnetic spin-orbit contribution. This interpretation is based on truncated shell-model calculations in the full fp space. The magnitude, sign, and hence significance of other Coulomb monopole terms in explaining the observed MED differences

remains to be investigated, preferably through a dedicated theoretical study of mirror nuclei in the upper fp shell.

We would like to thank the staff and the accelerator crew at ORNL for the excellent support during the experiment and F. Nowacki for helpful discussions. This research was supported in part by the Swedish Research Council.

-
- [1] *Isospin in Nuclear Physics*, edited by D. H. Wilkinson (North-Holland, Amsterdam, 1969).
- [2] M. A. Bentley *et al.*, in *Proceedings Pingst 2000—Selected Topics on $N = Z$ Nuclei*, edited by D. Rudolph and M. Hellström (Bloms i Lund, Sweden, 2000), p. 222.
- [3] S. M. Lenzi and P. G. Bizzeti, in *Achievements with the EUROBALL Spectrometer*, edited by W. Korten and S. Lunardi (LNL-IFN(Rep)201, 2004), p. 59.
- [4] M. A. Bentley, C. D. O’Leary, A. Poves, G. Martínez-Pinedo, D. E. Appelbe, R. A. Bark, D. M. Cullen, S. Ertürk, and A. Maj, *Phys. Lett.* **B437**, 243 (1998).
- [5] J. Ekman *et al.*, *Eur. Phys. J. A* **9**, 13 (2000).
- [6] S. J. Williams *et al.*, *Phys. Rev. C* **68**, 011301(R) (2003).
- [7] S. M. Lenzi *et al.*, *Phys. Rev. Lett.* **87**, 122501 (2001).
- [8] P. E. Garrett *et al.*, *Phys. Rev. Lett.* **87**, 132502 (2001).
- [9] A. P. Zuker, S. M. Lenzi, G. Martínez-Pinedo, and A. Poves, *Phys. Rev. Lett.* **89**, 142502 (2002).
- [10] J. Ekman *et al.*, *Phys. Rev. Lett.* **92**, 132502 (2004).
- [11] M. R. Bhat, *Nucl. Data Sheets* **85**, 415 (1998).
- [12] C. Andreoiu *et al.*, *Eur. Phys. J. A* **14**, 317 (2002).
- [13] J. A. Winger *et al.*, *Phys. Rev. C* **48**, 3097 (1993).
- [14] M. J. López Jiménez *et al.*, *Phys. Rev. C* **66**, 025803 (2002).
- [15] M. Oinonen *et al.*, *Eur. Phys. J. A* **5**, 151 (1999).
- [16] L. Weissman *et al.*, *Phys. Rev. C* **65**, 044321 (2002).
- [17] M. R. Bhat, *Nucl. Data Sheets* **88**, 417 (1999).
- [18] S. M. Vincent *et al.*, *Phys. Rev. C* **60**, 064308 (1999).
- [19] O. Izotova *et al.*, *Phys. Rev. C* **69**, 037303 (2004).
- [20] E. K. Johansson, Master’s thesis, Lund University, LUNFD6/(NFFR-5023)1-47, 2004.
- [21] C. J. Gross *et al.*, *Nucl. Instrum. Meth. Phys. Res. A* **450**, 12–29 (2000).
- [22] L-L. Andersson, Master’s thesis, Lund University, LUNFD6/(NFFR-5022)1-47, 2004.
- [23] J. A. Cameron and B. Singh, *Nucl. Data Sheets* **94**, 429 (2001).
- [24] J. Ekman *et al.*, *Phys. Rev. C* **70**, 057305 (2004).
- [25] E. Caurier, shell model code ANTOINE, IRES, Strasbourg, 1989-2002.
- [26] E. Caurier and F. Nowacki, *Acta Phys. Pol.* **30**, 705 (1999).
- [27] M. Honma, T. Otsuka, B. A. Brown, and T. Mizusaki, *Phys. Rev. C* **69**, 034335 (2004).
- [28] M. Honma, T. Otsuka, B. A. Brown, and T. Mizusaki, *Phys. Rev. C* **65**, 061301 (2002).
- [29] R. J. Blin-Stoyle, in *Isospin in Nuclear Physics*, edited by D. H. Wilkinson (North-Holland, Amsterdam, 1969), Ch. 4.
- [30] D. Rudolph *et al.*, *Phys. Rev. Lett.* **80**, 3018 (1998).

Paper 2

γ -ray spectroscopy of excited states in $^{61}_{30}\text{Zn}_{31}$

L-L. Andersson^{1,a}, D. Rudolph¹, J. Ekman^{1,b}, C. Fahlander¹, E.K. Johansson¹, R. du Rietz¹, C.J. Gross², P.A. Hausladen², D.C. Radford², and G. Hammond^{3,c}

¹ Department of Physics, Lund University, S-221 00 Lund, Sweden

² Physics Division, Oak Ridge National Laboratory, Oak Ridge, TN 37830, USA

³ School of Chemistry and Physics, Keele University, Keele, Staffordshire ST5 5BG, UK

Received: 22 June 2006 / Revised: 2 October 2006 /

Published online: 15 November 2006 – © Società Italiana di Fisica / Springer-Verlag 2006

Communicated by R. Krücken

Abstract. The $^{61}_{30}\text{Zn}_{31}$ isotope has been produced at the Oak Ridge National Laboratory in the fusion-evaporation reaction $^{40}\text{Ca}(^{24}\text{Mg}, 2\text{pn})^{61}\text{Zn}$ at 104 MeV. The experimental set-up allowed γ -rays to be detected in the CLARION Ge detector array in coincidence with the detection of recoiling nuclei in the focal plane at the end of the recoil mass spectrometer. This provides a unique identification of γ -rays belonging to ^{61}Zn . The excited states have been explored by means of recoil- $\gamma\gamma$ coincidences, and the resulting decay scheme comprises almost 70 transitions. The data reveal numerous non-yrast states and suggest a revised spin and parity assignment for a previously observed superdeformed band. The resulting decay scheme is compared to predictions from different sets of large-scale shell model calculations.

PACS. 21.60.Cs Shell model – 23.20.En Angular distribution and correlation measurements – 23.20.Lv γ transitions and level energies – 27.40.+z $39 \leq A \leq 58$

1 Introduction

The $^{61}_{30}\text{Zn}_{31}$ nucleus lies just beyond the $N = Z = 28$ shell closure, with two protons and three neutrons occupying the subshells up to the next closure at $N = Z = 50$. The subshells placed in between the two shell closures are the negative-parity $2p_{3/2}$, $1f_{5/2}$ and $2p_{1/2}$ orbitals in the upper fp shell, and the positive-parity $\ell = 4$ $1g_{9/2}$ intruder orbital. Because of its high- j nature, excitations into the latter influence or even dominate the level sequences of $N \sim Z$, $A \simeq 60$ nuclei already at moderate excitation energies. Examples of this are $^{59,61}\text{Cu}$ and ^{61}Zn [1–3]. An additivity principle was derived in ref. [1], which relates the amount of quadrupole deformation to the number of particles in the $1g_{9/2}$ orbital and holes in the $1f_{7/2}$ orbital, providing a natural transition from spherical structures to superdeformed (SD) rotational sequences.

Theoretically, the inclusion of the $1g_{9/2}$ orbital in state-of-the-art shell-model calculations is difficult due to the center-of-mass problem, here caused by insufficient

separation of center-of-mass and relative coordinates of the 61 nucleons (cf. p. 447 and p. 482ff in ref. [4]).

Another facet of $N \sim Z$, $A \simeq 60$ nuclei is the investigation of isospin symmetry by studying mirror nuclei, *i.e.* nuclei with the same mass number but with interchanged proton and neutron numbers. The mirror nucleus of $^{61}_{30}\text{Zn}_{31}$ is $^{61}_{31}\text{Ga}_{30}$, where the first few excited states recently have been established [5]. To obtain solid information on isospin-breaking effects from mirror nuclei, detailed spectroscopic knowledge of the less exotic partner—in this case ^{61}Zn —is necessary.

In the present paper we report on the investigation of excited states in ^{61}Zn . Previous data aimed to extend an existing [6, 7] low-spin level scheme [2], to determine parity-changing $E1$ transitions [3], and to search for superdeformed rotational bands [8]. The most recent decay scheme of normally deformed structures in ^{61}Zn comprises some 25 γ -ray transitions reaching over 9 MeV excitation energy and a few spin and parity assignments [2], which were refined in ref. [3]. Our analysis provides a firm decay scheme with a considerable increase to almost 70 transitions ranging up to a spin $I^\pi = 31/2^-$ state at an excitation energy of $E_x = 10155$ keV. Interestingly, revised spin assignments of the low-lying levels based on ref. [3] and the current analysis affect the presumed, tentative spin assignments of the ^{61}Zn SD band [8].

^a e-mail: lise-lotte.andersson@nuclear.lu.se

^b Present address: Technology and Society, Malmö University, S-205 06 Malmö, Sweden.

^c Present address: Department of Physics, University of York, Heslington, York, YO10 5DD, UK.

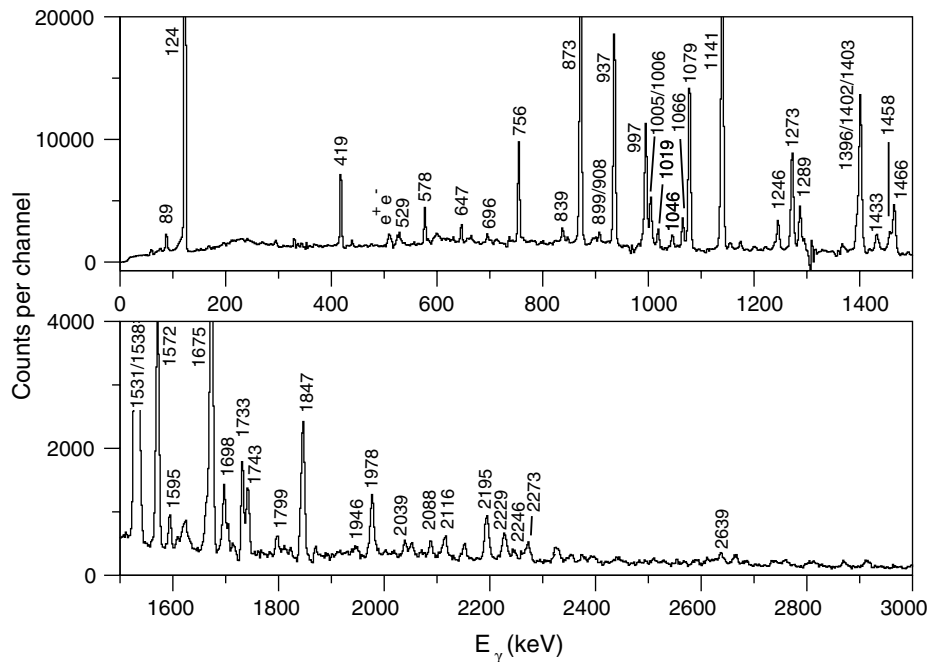


Fig. 1. Clean recoil- γ spectrum of ^{61}Zn . The most intense transitions are marked with energies in keV. The spectrum is binned to 2 keV/channel. See text for more details.

The experimentally observed energy levels in the ^{61}Zn nucleus are compared with shell model calculations using two different configuration spaces: i) the full fp space, neglecting excitations up to the $1g_{9/2}$ orbital, and ii) a closed ^{56}Ni core with the five valence nucleons moving in and between the $1f_{5/2}$, $2p_{3/2}$, $2p_{1/2}$, and $1g_{9/2}$ orbitals.

This paper reports on the experimental details including the set-up (sect. 2), the data analysis (sect. 3) and results (sect. 4). Section 5 deals with the shell model calculations involving both of the above-mentioned configuration spaces.

2 The experiment

The experiment was conducted at the Holifield Radioactive Ion Beam Facility (HRIBF) at Oak Ridge National Laboratory. In fusion-evaporation reactions of a 104 MeV ^{40}Ca beam, impinging on a 99.92% isotropically enriched ^{24}Mg target foil of thickness 0.3 mg/cm^2 , ^{64}Ge compound nuclei are formed. The $^{61}\text{Zn}_{31}$ nuclei are then produced via the evaporation of two protons and one neutron.

The experimental set-up comprised the germanium detector array, CLARION [9], consisting of ten Ge clover detectors placed in a three ring configuration (90° , 132° , and 154°), and the Recoil Mass Spectrometer (RMS) using the split anode Ionisation Chamber (IC) at the focal plane [10]. The distance between the clover detectors and the target was 20.0 cm. In that configuration CLARION has an overall γ -ray detection efficiency of about 2.3% at 1.3 MeV γ -ray energy. At the end of the experiment CLARION was energy calibrated using the three standard γ -ray sources ^{152}Eu , ^{133}Ba , and ^{88}Y .

The combination of CLARION, RMS, and IC allows for correlations between γ -rays and residual nuclei providing a unique identification of γ -rays belonging to ^{61}Zn . The correlation was also used in the trigger conditions. An event was recorded only if one of two conditions was met: i) at least one Compton-suppressed γ -ray was detected in CLARION in coincidence with the detection of a recoil at the focal plane of the RMS or ii) two or more Compton-suppressed γ -rays were detected in the germanium detectors. More details about the set-up and data handling are described in ref. [5]. These include the Doppler and add-back corrections applied to the γ -ray data collected from the segmented 4-fold germanium clover detectors in CLARION.

The RMS separates the recoils in mass-to-charge ratio, A/Q , where Q denotes the charge state of the recoiling nuclei. For a given charge state masses are thus determined by their horizontal position at the focal plane of the spectrometer. These positions are measured by a position-sensitive grid, placed inside the IC. Information about the energy and the atomic number, Z , of the recoils is provided via the differential energy loss information from the split anode in the IC. This information is comprised in the R_{13} parameter, which relates the energy loss in the first and the third part of the IC anode via the ratio between the two. The R_{13} parameter is introduced and explained further in ref. [5].

3 Analysis

In total there are three isotopes of mass $A = 61$ observed in the present fusion-evaporation reaction; $^{61}\text{Cu}_{32}$, $^{61}\text{Zn}_{31}$,

Table 1. Excitation energies, γ -ray energies, relative intensities, and angular-distribution ratios for transitions in ${}^{61}\text{Zn}$ [6, 2, 3].

E_x (keV)	E_γ (keV)	I_γ (%)	R_{154-96}	I_i^π	I_f^π
88.8(2)	88.9(1)	3.0(1)	1.08(7)	$1/2^{-2}$	$3/2^{-1}$
123.9(2)	123.9(1)	100(3)	$\simeq 0.55^4$	$5/2^{-1}$	$3/2^{-}$
419.2(2)	295.5(1)	0.6(1)	1.55(34)	$3/2^{-2}$	$5/2^{-}$
	331.3(2)	1.2(1)	0.97(16)	$3/2^{-}$	$1/2^{-}$
	419.1(2)	8.9(3)	1.11(6)	$3/2^{-}$	$3/2^{-}$
756.4(3)	339.0(2)	0.9(1)	—	$5/2^{-2}$	$3/2^{-}$
	631.7(3)	1.1(1)	0.72(16)	$5/2^{-}$	$5/2^{-}$
	666.6(3)	1.8(1)	—	$5/2^{-}$	$1/2^{-}$
	755.7(4)	18(1)	0.60(3)	$5/2^{-}$	$3/2^{-}$
997.7(4)	241.4(1)	0.5(1)	—	$7/2^{-1}$	$5/2^{-}$
	578.2(3)	4.4(2)	1.40(9)	$7/2^{-}$	$3/2^{-}$
	872.7(4)	73(2)	0.64(3)	$7/2^{-}$	$5/2^{-}$
	996.7(5)	27(6)	1.48(7) ³	$7/2^{-}$	$3/2^{-}$
1266(1)	1141(1)	83(3)	1.62(7)	$9/2^{-1}$	$5/2^{-}$
1403(1)	647.1(3)	3.4(1)	0.66(6)	$7/2^{-2}$	$5/2^{-}$
	984.3(5)	3.5(5)	—	$7/2^{-}$	$3/2^{-}$
	1278(1)	2.0(1)	1.01(12)	$7/2^{-}$	$5/2^{-}$
	1403(1)	5.3(31)	0.84(4) ³	$7/2^{-}$	$3/2^{-}$
2003(1)	737.6(4)	1.0(1)	—	$9/2^{-2}$	$9/2^{-}$
	1006(1)	8.5(10)	0.37(2) ³	$9/2^{-}$	$7/2^{-}$
	1246(1)	8.1(3)	1.40(8)	$9/2^{-}$	$5/2^{-}$
2270(1)	1005(1)	10(1)	0.37(2) ³	$11/2^{-1}$	$9/2^{-}$
	1273(1)	27(1)	1.77(8)	$11/2^{-}$	$7/2^{-}$
2400(1)	997.0(5)	5(3)	1.48(7) ³	$9/2^{+1}$	$7/2^{-}$
	1403(1)	41(5)	0.84(4) ³	$9/2^{+}$	$7/2^{-}$
	2273(1)	2.3(1)	1.17(16)	$9/2^{+}$	$5/2^{-}$
2699(2)	696.2(3)	1.7(1)	0.70(13)	$11/2^{-}$	$9/2^{-}$
	1433(1)	6.7(2)	1.01(6)	$11/2^{-}$	$9/2^{-}$
2799(2)	529.4(3)	0.8(1)	—	$13/2^{-1}$	$11/2^{-}$
	1531(1)	46(3)	1.70(7) ³	$13/2^{-}$	$9/2^{-}$
3244(2)	1978(1)	7.7(3)	0.78(6)	$11/2^{+1}$	$9/2^{-}$
3336(1)	936.7(5)	39(2)	1.70(7)	$13/2^{+1}$	$9/2^{+}$
	1066(1)	6.9(2)	0.98(6)	$13/2^{+}$	$11/2^{-}$
3461(2)	1458(1)	6.6(3)	1.51(9)	$13/2^{-}$	$9/2^{-}$
	2195(1)	5.5(3)	1.60(11)	$13/2^{-}$	$9/2^{-}$
3495(3)	2229(1)	3.4(1)	1.40(12)	—	$9/2^{-}$
3844(2)	1046(1)	4.2(1)	—	$15/2^{-1}$	$13/2^{-}$
	1572(1)	16(1)	1.62(8)	$15/2^{-}$	$11/2^{-}$
4264(2)	1019(1)	3.6(1)	1.73(13)	$15/2^{+1}$	$11/2^{+}$
	1466(1)	19(1)	0.73(4)	$15/2^{+}$	$13/2^{-}$
4309(3)	2039(1)	1.9(1)	0.87(14)	$13/2$	$11/2^{-}$
4415(2)	1079(1)	35(1)	1.76(7)	$17/2^{+1}$	$13/2^{+}$
4644(2)	1847(1)	11(1)	1.66(9)	$17/2^{-1}$	$13/2^{-}$
4915(3)	2116(1)	3.4(1)	0.81(9)	—	$13/2^{-}$
5195(3)	1733(1)	3.5(11)	1.49(10) ³	$17/2^{-}$	$13/2^{-}$
5254(2)	839.2(4)	3.1(1)	1.18(10)	—	$17/2^{+}$
	990.9(5)	1.4(3)	1.32(13) ³	—	$15/2^{+}$
5468(3)	1624(1)	3.6(1)	—	—	$15/2^{-}$
5543(2)	898.9(4)	2.1(7)	—	$19/2^{-1}$	$17/2^{-}$
	1698(1)	5.8(3)	1.57(10)	$19/2^{-}$	$15/2^{-}$
5552(2)	908.3(5)	2.6(1)	0.62(10)	$19/2^{+1}$	$17/2^{-}$
	1289(1)	11(1)	1.67(9)	$19/2^{+}$	$15/2^{+}$
6090(2)	1675(3)	22(2)	1.69(8) ³	$21/2^{+1}$	$17/2^{+}$
6212(3)	1799(1)	2.3(6)	—	—	$17/2^{+}$
	1946(1)	1.4(1)	—	—	$15/2^{+}$

Table 1. Continued.

E_x (keV)	E_γ (keV)	I_γ (%)	R_{154-96}	I_i^π	I_f^π
7284(2)	1733(1)	1.2(3)	1.49(10) ³	$21/2^{-}$	$19/2^{+}$
	2088(1)	1.7(1)	1.32(17)	$21/2^{-}$	$17/2^{-}$
	2639(1)	2.1(9)	—	$21/2^{-}$	$17/2^{-}$
7295(3)	1743(1)	5.4(3)	1.47(10)	$23/2^{+1}$	$19/2^{+}$
7486(3)	1396(1)	9.9(4)	1.93(10)	$25/2^{+1}$	$21/2^{+}$
7629(2)	344.8(2)	0.3(1)	1.20(24)	$23/2^{-1}$	$21/2^{-}$
	1538(1)	7.5(7)	0.60(6)	$23/2^{-}$	$21/2^{+}$
8336(3)	2246(1)	0.9(1)	—	—	$21/2^{+}$
8496(4)	1201(1)	2.2(1)	—	—	$23/2^{+}$
8777(3)	440.6(2)	0.5(1)	0.71(18)	—	—
8879(3)	1595(1)	1.9(1)	1.79(21)	$25/2^{-}$	$21/2^{-}$
9161(3)	1532(1)	6.3(7)	1.70(7) ³	$27/2^{-1}$	$23/2^{-}$
	1675(4)	4.0(20)	1.69(8) ³	$27/2^{-}$	$25/2^{+}$
10155(3)	994.1(5)	3.4(6)	1.48(7) ³	$31/2^{-1}$	$27/2^{-}$

¹Spin and parity supported or adopted from ref. [3].²Spin and parity supported or adopted from ref. [6].³Doublet structure.⁴Ratio corrected using the estimated lifetime of the state.

and ${}^{61}\text{Ga}_{30}$. Since the recoils have different proton numbers the energy loss signals will peak at slightly different values of R_{13} . Hence, it is possible to increment γ -ray spectra containing predominately recoils of only one species. This is done by restricting the values of R_{13} around the known peak positions for ${}^{61}\text{Cu}$, ${}^{61}\text{Zn}$, and ${}^{61}\text{Ga}$, respectively. Performing a careful fractional subtraction makes it possible to obtain clean γ -ray spectra for the three $A = 61$ recoils. The resulting clean ${}^{61}\text{Zn}$ spectrum is shown in fig. 1. Only at 1310 keV, an effect of the fractional subtraction can be seen. The fluctuations are a result of the subtraction of the most intense peak in ${}^{61}\text{Cu}$, which is the strongest of the $A = 61$ reaction channels.

From the clean ${}^{61}\text{Zn}$ spectrum transitions have been identified, their energies have been determined, and relative intensities have been obtained. The results are listed in table 1. Intensities, I_γ , in the table are both efficiency corrected and corrected for the mean angular position of all detectors. At a mean position of $\bar{\theta} \approx 55^\circ$ the relative intensities of $\Delta I = 0, 1$, and 2 transitions are equal [11]. In CLARION the mean position is at $\bar{\theta} = 65^\circ$ and correction factors to account for the non-equal detection have to be determined. By evaluating angular distributions calculated with alignment coefficients, σ , typical for fusion-evaporation reactions, correction factors of 1.09(2) and 0.95(2) for $\Delta I = 0, 2$ and $\Delta I = 1$ transitions, respectively, have been derived. These are included in the values in table 1.

The data from this experiment was incorporated in so-called recoil- $\gamma\gamma$ matrices, which were used to establish coincidences between γ -ray transitions. As the name implies, the $\gamma\gamma$ -matrices are gated by recoils, *i.e.*, they contain only γ -rays observed in coincidence with the detection of an $A = 61$ recoil in the focal plane. Two matrices were constructed; one with R_{13} -values compatible with ${}^{61}\text{Zn}$ and the other compatible with ${}^{61}\text{Cu}$. This restriction aimed to minimise the amount of contaminants. The

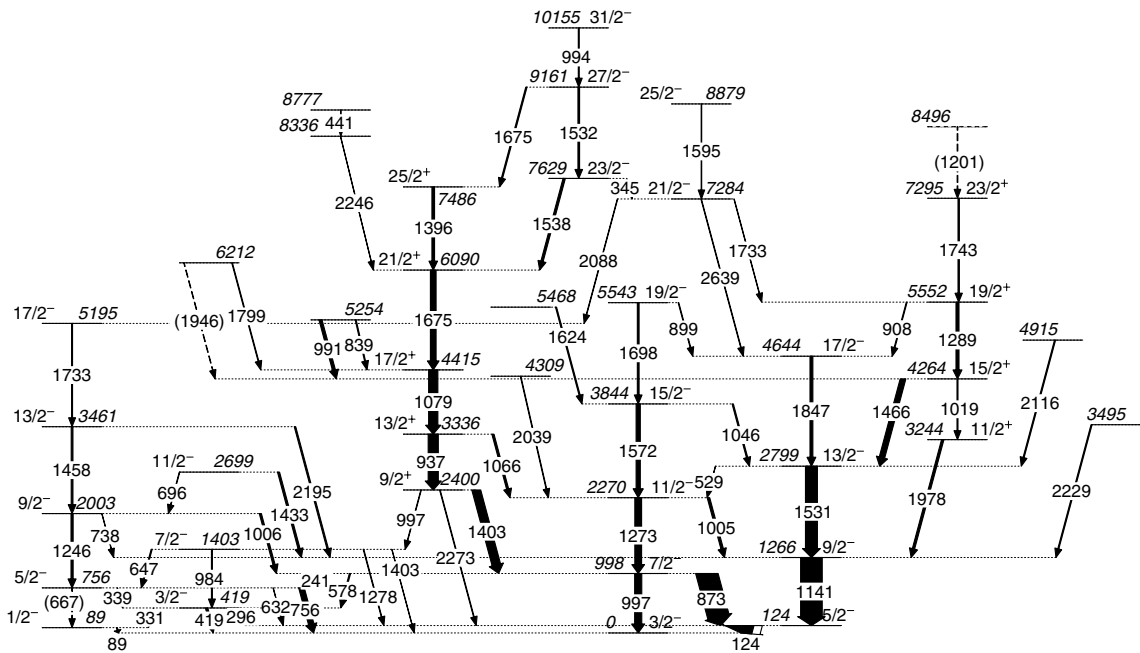


Fig. 2. The decay scheme of ^{61}Zn from the present work. Energy labels are in keV and the intensities of the transitions are here indicated by the relative thicknesses of the arrows. Tentative levels and transitions are dashed.

presence of ^{61}Cu (^{61}Zn) recoils in the ^{61}Zn (^{61}Cu) gated matrix is, however, unavoidable due to the partially overlapping R_{13} -values of the two species. Coincidence spectra obtained by identically selecting a specific transition in the two matrices, can be subtracted from each other in a similar manner as previously described for the spectrum in fig. 1. This results in an “isotopic” $\gamma\gamma$ analysis of the ^{61}Zn transitions.

The careful coincidence analysis using the recoil- $\gamma\gamma$ matrices described above has been carried out for the ^{61}Zn nucleus. Figures 3, 4, and 5 show examples of coincidence spectra, both for intense and weak transitions. As can be seen from the figures, coinciding γ -ray transitions are easily determined from these very clean spectra. The coincidence information has been used to build the comprehensive decay scheme of ^{61}Zn , illustrated in fig. 2. A few transitions, which have not been possible to place into the decay scheme due to lack of statistics, remain unmarked in fig. 1.

Intensity ratios of γ -rays observed in different detector rings in the set-up [5] are also included in table 1. In the current analysis this ratio, R_{154-96} , is determined for the detectors placed at 84° , 96° , with respect to the beam axis, and those placed at 148° , 160° . Due to the dependence of the angular distribution on detector position the latter detectors may be treated as having an average detector position of 154° . The former, due to the symmetry at 90° , must be kept at either of the two positions, since they are placed symmetrically around 90° . Hence, R_{154-96} gives the ratio of yields, Y , between two of the detector rings in CLARION. Ratios for known stretched $\Delta I = 2$ reference transitions amount to $R_{154-96} = Y(154^\circ)/Y(96^\circ) \sim 1.6-1.7$, while stretched dipole transitions have $R_{154-96} \sim 0.7-0.8$. In order to assign both spin and parity to the levels the

previously published assignments from ref. [3], investigated by means of angular correlations (DCO-ratios) and linear polarisations, and ref. [6] have been included. The previous assignments are confirmed by the angular distributions found in the current experiment. Additional levels have been assigned spin and parity based on angular distributions from the current analysis and yrast arguments.

Two things from table 1 are worth extra attention. First note the 124 keV level, which is fed with a total intensity of 160(4) units, but with a total decay of only 100(3) units. The large discrepancy can be explained by the combined effect of internal conversion of the 124 keV γ -ray and a relatively long lifetime of the 124 keV state. In fact, both these effects are coupled to each other via the R_{154-96} value of this transition. The experimentally obtained value is $R_{154-96} = 0.91(4)$. This value indicates either an almost pure $\Delta I = 1$ dipole transition or an almost pure $\Delta I = 1$ quadrupole transition. The conversion coefficients in these two extreme cases are $\alpha = 0.04$ and $\alpha = 0.32$, respectively. Thus, even in the case of a pure quadrupole transition internal conversion can only account for a fraction of the missing yield. The remaining portion of about 30(6) units is attributed to a relatively long lifetime of the 124 keV state, which is estimated in the following.

Arrays of Ge detectors such as CLARION reach their full efficiency only if the γ -rays are emitted at the target position. If the recoiling nuclei γ decay at a position, d , behind the target, only a fraction, $\Omega(d)$, of the maximal solid angle, Ω_0 , is accessible. Clearly, $\Omega(d)$ depends on the detector position, *i.e.* $\Omega(d) = \Omega(d, \theta)$. With a proper calibration isomeric states can be measured via this “shadowing” of the germanium detectors [12]. In this analysis, however, only an estimation of the lifetime can be ob-

tained as there are no calibration points. The function $\Omega(d, \theta)$ has been simulated and then replaced by the approximative assumption

$$\Omega(d, \theta) = \begin{cases} \Omega_0, & d \leq D_0(\theta), \\ 0, & d > D_0(\theta), \end{cases}$$

with $D_0(96^\circ) = 8$ cm, $D_0(132^\circ) = 16$ cm, $D_0(154^\circ) = 22$ cm and $D_0(\bar{\theta}) = 13$ cm. Using the latter, the missing yield, and knowing the average velocity $v/c = 4.26(1)\%$ for the recoils, the lifetime, τ , can be estimated. In case of a pure dipole (quadrupole) transition one obtains $\tau \approx 10$ ns ($\tau \approx 6$ ns). The experimentally obtained intensities of the 124 keV line in the different detector rings hence lack yield due to recoils in the long-lived state moving away from the target position before decaying. Consequently, the experimentally obtained R_{154-96} needs to be corrected. The correction factors obviously depend on τ and, hence, on the multipolarity of the transition. In case of a pure dipole transition the correction factors are 1.2 (154°) and 2.2 (96°), and in case of a quadrupole character they are 1.1 and 1.6, respectively. This results in a corrected R_{154-96} value of about 0.5 (dipole) and 0.6 (quadrupole). Using an average of these values provides some kind of self-consistent estimate for the involved quantities: $R_{154-96} \approx 0.55$ and $\tau \approx 8$ ns gives a $\delta(E2/M1) \approx 1$ mixing of this transition.

The second remark from table 1 concerns the “double doublet” structure of the yrare and yrast 1403 keV and the yrare and yrast 997 keV transitions, which in parallel depopulate the $9/2^+$ level at 2400 keV. The 1403 keV energy level and the transition into the ground state are previously known [6]. First of all, gating on the 997 keV and the 873 keV transitions in the current data set results in a non-equal ratio between the yields of the 1273 keV and the 1403 keV γ -ray transitions, which feed the 998 keV level. In fact, the gate reveals a larger amount of the 1403 keV transition in the 997 keV gate than in the 873 keV gate. This provides first evidence for the two yrare transitions in the “double doublet” structure. The determination is, however, complicated by the energetically close 1396 and 994 keV transitions.

To obtain reasonable values of the relative intensities of the four transitions it is necessary to make indirect measurements. From the spectrum in coincidence with the 1273 keV transition the branching ratio between the yrast 997 keV and the 873 keV transitions could be obtained. The 873 keV γ -ray transition is well established, but difficulties arise from the 994 keV $31/2^- \rightarrow 27/2^-$ transition, which is close in energy to the 997 keV transitions and impossible to separate completely. In a similar way, the branching ratio between the 1273 and the yrast 1403 keV transitions might be obtained from the spectrum in coincidence with the 873 keV transition. Difficulties, however, arise from the energetically close-lying 1396 keV $25/2^+ \rightarrow 21/2^+$ transitions, which can affect the ratio of yields.

While the intensities of the two yrast transitions can be determined reasonably well with the described procedure,

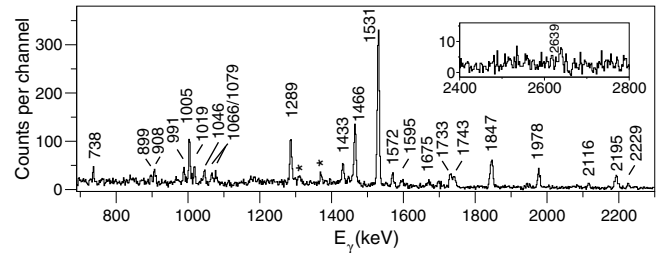


Fig. 3. Recoil- $\gamma\gamma$ spectrum in coincidence with $A = 61$, $Z = 30$ identified in the RMS, and the intense 1141 keV $9/2^- \rightarrow 5/2^-$ yrast transition. All peaks marked with an energy label are placed into the decay scheme of fig. 2, while stars denote minor contaminations from ${}^{61}\text{Cu}$. The spectrum is binned to 2 keV/channel.

it turns out to be basically impossible to obtain meaningful numbers for the yrare transitions from the current data set. However, using information from an independent, early data set taken with the GAMMASPHERE array, the estimates included in table 1 can be derived for the yrare transitions [13].

4 Results

In fig. 3 transitions in coincidence with the intense 1141 keV $9/2^- \rightarrow 5/2^-$ γ -ray are illustrated. The previously known [3] negative-parity yrast sequence 1847, 1531, 1141 keV can easily be seen in the figure via the first two γ -rays. Spin and parity of this sequence are well determined (see ref. [3] and table 1). In fig. 3 the 1743, 1289, and 1019 keV transitions between positive-parity yrast states are illustrated. The spin and parity assignments of the involved energy levels differ between ref. [2] and ref. [3], while the present analysis supports the $11/2$ assignment of the 3244 keV level by the $\Delta I = 2$ 1019 keV and the $\Delta I = 1$ 1466 and 1978 keV transitions. The two sequences mentioned above are connected via three transitions at 1978, 1466, and 908 keV, respectively. Peaks at these energies are also present in fig. 3. The high-lying levels at 8879 and 7284 keV from fig. 2 are established indirectly in the coincidence spectrum of fig. 3, via the 1595 keV transition between them and the 1733 keV transition connecting them to the $19/2^+$ level. Spin and parity of the level at 7284 keV are determined via its connection both to the positive-parity band to the right and the negative-parity band to the far left in fig. 2. The 2088 keV transition can be used as guidance due to its likely $\Delta I = 2$ character. The 1733 keV transition, however, is unreliable due to its doublet structure. The 2639 keV $21/2^- \rightarrow 17/2^-$ transition, visible in fig. 2, is not very intense but can be distinguished in a close-up view of the spectrum.

Figure 4 illustrates the coincidences with the 1675 keV, $21/2^+ \rightarrow 17/2^+$, and $27/2^- \rightarrow 25/2^+$, doublet structure. The two transitions are found to be self-coincident. The lower 1675 keV transition is placed in the clearly visible 937, 1079, 1675, and 1396 keV sequence, present in the figure, while the upper 1675 keV transition is feeding it.

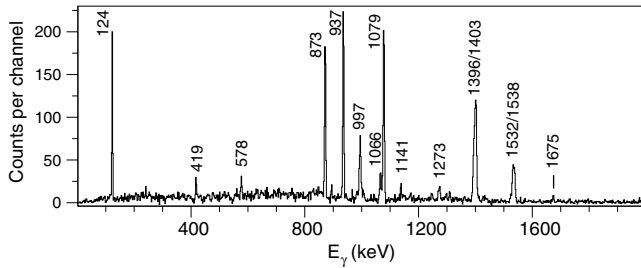


Fig. 4. Same as fig. 3 but in coincidence with the 1675 keV $21/2^+ \rightarrow 17/2^+$ and the 1675 keV $27/2^- \rightarrow 25/2^+$ yrast transitions.

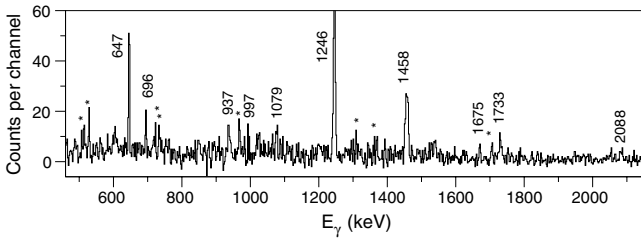


Fig. 5. Same as fig. 3 but in coincidence with the 756 keV $5/2^- \rightarrow 3/2^-$ ground-state transition. The low intensity of this transition in combination with the energetically close 762 keV transition in ^{61}Cu makes the contaminating transitions much more intense than in the previous figures.

The positive parity of the lower 1675 keV transition's band has already been established via the clear $E1$ properties of both the 1403 keV and the 1066 keV transitions [3]. In the same paper the 1538 keV transition has been established, causing the connected energy level at 7629 keV to have spin and parity $23/2^-$. Combining this with the $E2$ character of the 1396 keV transition determines the upper 1675 keV transition to decay from $27/2^-$ down to a $25/2^+$ level. The properties of the 1532 keV transition are not as reliable due to the close placement of the 1531 keV $13/2^- \rightarrow 9/2^-$ doublet transition.

Figure 5 illustrates the γ -rays in coincidence with the 756 keV $5/2^- \rightarrow 3/2^-$ ground-state transition. The spectrum contains more contaminating transitions from ^{61}Cu than previous figures. This is a result of the combined effect of gating on a relatively weak transition in ^{61}Zn and having an energetically close (762 keV) transition in ^{61}Cu . In spite of the contamination of ^{61}Cu in the gate the ^{61}Zn information is clear. Two transitions decay into the 756 keV energy level, the 1246 and 647 keV transitions, both clearly visible in this spectrum. The subsequent 1458, 1733 and 2088 keV transitions are all three also illustrated in the figure. Even the positive-parity yrast sequence of 1675, 1079, 937 keV transitions are indicated in this spectrum, all decaying into the 756 keV energy level via the earlier mentioned, difficult 997 keV γ -ray transition. This weak transition is indirectly established by the presence of these transitions in the coincidence spectrum.

5 Shell model interpretation

The experimental results can be compared with predictions obtained from large-scale shell model calculations using the code ANTOINE [14,15]. In the present paper two calculations have been carried out.

The first calculation involves the $1f_{7/2}$ orbit below the $N = Z = 28$ shell closures and the $2p_{3/2}$, $1f_{5/2}$, and $2p_{1/2}$ orbits above —here referred to as the fp calculation. No positive-parity states will be obtained for ^{61}Zn in this calculation as the configuration space includes only odd- ℓ orbitals. The interaction, GXPF1 [16,17], is adjusted to nuclei beyond the $N = Z = 28$ shell closure. In the current calculation no Coulomb interaction was included and the configuration space was truncated to allow up to three particle excitations from the $1f_{7/2}$ shell into the upper fp shell.

The second calculation uses a ^{56}Ni core and allows only excitations outside the core, *i.e.*, neglecting the $1f_{7/2}$ orbit. On the other hand, it includes the $1g_{9/2}$ orbit, and it is referred to as the $f_{5/2}pg_{9/2}$ calculation in the following. This interaction is derived from the Bonn-C nucleon-nucleon interaction and adjusted for the $Z > 28$, $N < 50$ region [18] in a similar fashion as it was done for GXPF1 within the fp shell [16,17].

In fig. 6 the experimental level energies are compared with the predicted energies from the two calculations. In the middle and on the right-hand side of the figure the negative- and positive-parity yrast states are shown. On the left-hand side the negative-parity yrare states are illustrated. Third states of a given spin-parity combination are not included in the figure because there are essentially no experimentally well-defined states.

The energy levels from the fp calculation agree very well with the experimental states up to spin and parity $19/2^-$. However, at higher spins the levels clearly mismatch. These difficulties are expected, since the influence of the $1g_{9/2}$ orbital becomes more and more important when forming high-spin states in ^{61}Zn [1] due to its high- j nature.

The opposite situation is true for the $f_{5/2}pg_{9/2}$ calculation. The lack of the $1f_{7/2}$ orbital in the calculation may explain difficulties to reproduce low-spin states but a significantly better agreement than for the fp calculation is found at high spins. Figure 6 illustrates this for the negative-parity yrast levels where the predictions improve above spin $19/2$. The $f_{5/2}pg_{9/2}$ calculation also reproduces positive-parity yrast states well.

The Mean Level Deviation (MLD) measures how well the calculated energy levels match the experimental states. Normalising to the ground states, the MLD is here calculated as

$$\text{MLD} = \sqrt{\frac{\sum_i (E_{x_i} - E_{th_i})^2}{n}}, \quad (1)$$

where E_{x_i} and E_{th_i} are the experimentally observed and predicted energies, respectively, and n corresponds to the number of levels included in the MLD calculation.

For the fp calculation the MLD is 1561 keV if all yrare and yrast levels are included. The magnitude of this value

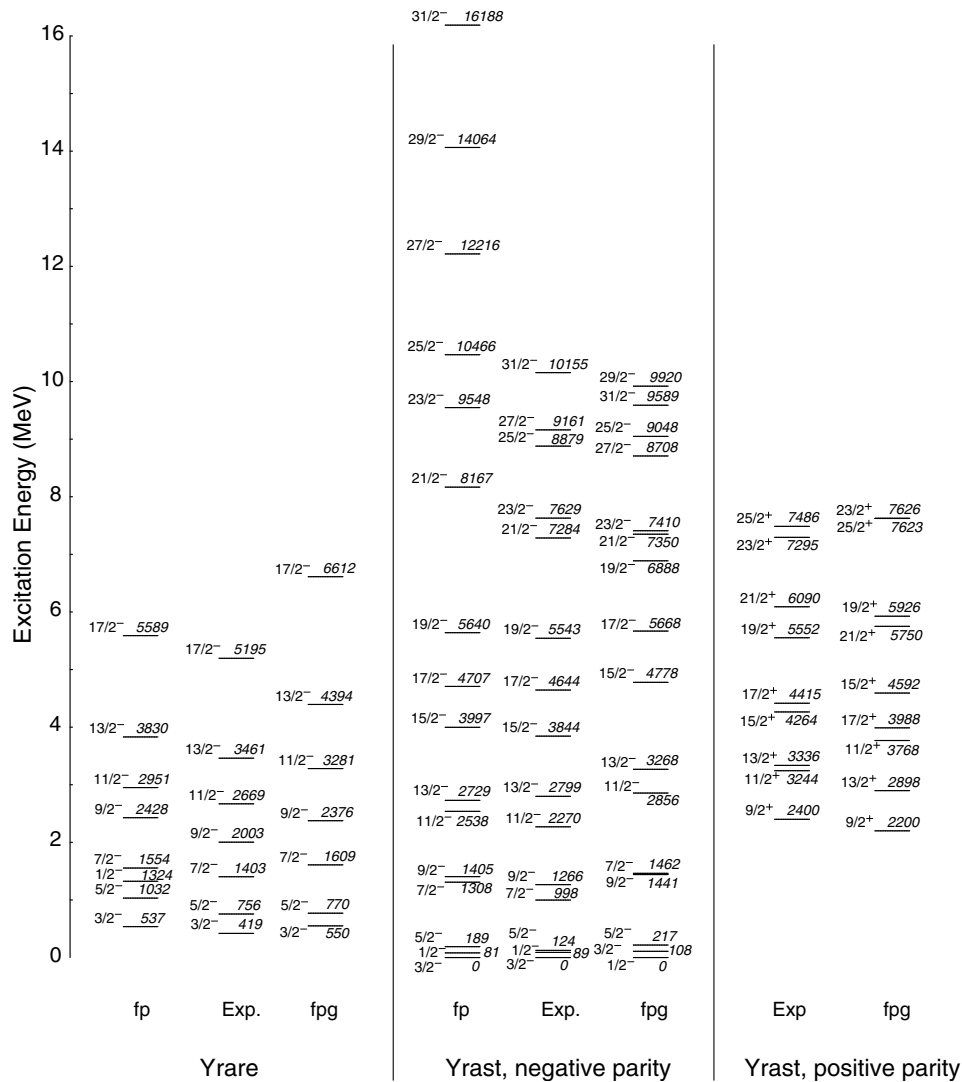


Fig. 6. Comparison between the experimental and calculated levels from the *fp* and *fpg* shell model calculation. The middle section illustrates the negative-parity yrast levels. On the right-hand side are the positive-parity yrast, and on the left-hand side are the negative-parity yrare states. See text for details.

suggests a poor agreement between experiment and theory. If only levels up to spin 19/2 are included the corresponding number drops dramatically to 228 keV, suggesting good agreement. Calculating MLD for only yrast levels up to spin 19/2 results in an even lower value of 153 keV. MLD values for the $f_{5/2}pg_{9/2}$ calculation are 569 keV if all yrast and yrare levels are included and including only yrast levels an MLD of 523 keV is obtained. A calculation of only levels above 19/2 results in a MLD of 307 keV.

Figure 6 illustrates in a simple way that neither of the two calculations used in this analysis are adequate to fully describe ^{61}Zn . Both holes in the $1f_{7/2}$ orbit and particles in the $1g_{9/2}$ orbit seem necessary in order for the calculation to truly reproduce the experimentally obtained nuclear energy levels. Calculations involving both orbitals are, however, impossible to carry out at present, due to the center-of-mass difficulties [4] mentioned earlier.

In the current analysis a more thorough investigation of the wave functions calculated by ANTOINE has been carried out. This analysis involves the electromagnetic decay properties of the nuclear states and is done using the free g -factors and effective charges of $0.5e$ ($1.5e$) for neutrons (protons). Applying the g -factors and the charges via the $B(M1)$ and $B(E2)$ values obtained for each transition enables a study of branching ratios b . Experimentally obtained relative strengths are compared to the calculated branching ratios and the results are illustrated in table 2. Here, all possible transitions, $\Delta I = 0, 1, 2$, have been investigated, including those transitions, which are predicted to be energetically allowed, but which have not been experimentally observed.

Generally, the results from the analysis of the electromagnetic decay properties show good agreement with the experimental data in the *fp* calculation both for the yrast and the yrare states below $I^\pi = 19/2^-$. An example

Table 2. Comparison between experimental and predicted branching ratios, b , of the γ -rays in ^{61}Zn . Two shell model calculations have been compared in this analysis. b_{fp} denotes the branching ratios from the fp calculation and b_{fpg} from the $f_{5/2}pg_{9/2}$ calculation. Transitions written in italic style are experimentally not observed (n.o.). See text for more details.

E_x (keV)	E_γ (keV)	I_i^π	I_f^π	b_{exp}	b_{fp}	b_{fpg}
88.8	89	$1/2_1^-$	$3/2_1^-$	1.0	1.0	1.0
123.9	<i>35</i>	$5/2_1^-$	$1/2_1^-$	n.o.	0.00	0.03
	124		$3/2_1^-$	1.0	1.0	0.97
419.2	296	$3/2_2^-$	$5/2_1^-$	0.06(1)	0.02	0.09
	331		$1/2_1^-$	0.11(1)	0.04	0.43
	419		$3/2_1^-$	0.83(2)	0.94	0.48
756.4	339	$5/2_2^-$	$3/2_2^-$	0.04(1)	0.05	0.01
	632		$5/2_1^-$	0.05(1)	0.07	0.04
	667		$1/2_1^-$	0.08(1)	0.00	0.00
	756		$3/2_1^-$	0.83(2)	0.88	0.95
997.7	241	$7/2_1^-$	$5/2_2^-$	n.o.	0.00	0.00
	578		$3/2_2^-$	0.04(1)	0.11	0.06
	873		$5/2_1^-$	0.70(5)	0.88	0.02
	997		$3/2_1^-$	0.26(5)	0.01	0.91
1266	<i>268</i>	$9/2_1^-$	$7/2_1^-$	n.o.	0.03	0.00
	<i>510</i>		$5/2_2^-$	n.o.	0.00	0.00
	1141		$5/2_1^-$	1.0	0.97	1.0
1403	<i>137</i>	$7/2_2^-$	$9/2_1^-$	n.o.	0.00	0.00
	<i>405</i>		$7/2_1^-$	n.o.	0.00	0.00
	647		$5/2_2^-$	0.24(5)	0.32	0.10
	984		$3/2_2^-$	0.25(7)	0.00	0.45
	1278		$5/2_1^-$	0.14(3)	0.05	0.14
	1403		$3/2_1^-$	0.37(19)	0.63	0.30
2003	<i>600</i>	$9/2_2^-$	$7/2_2^-$	n.o.	0.09	0.01
	738		$9/2_1^-$	0.06(1)	0.33	0.02
	1006		$7/2_1^-$	0.48(4)	0.27	0.02
	1246		$5/2_2^-$	0.46(4)	0.28	0.95
	<i>1879</i>		$5/2_1^-$	n.o.	0.02	0.00
2270	<i>267</i>	$11/2_1^-$	$9/2_2^-$	n.o.	0.00	0.00
	<i>867</i>		$7/2_2^-$	n.o.	0.00	0.03
	1005		$9/2_1^-$	0.27(3)	0.25	0.01
	1273		$7/2_1^-$	0.73(3)	0.75	0.96
2400	997	$9/2_1^+$	$7/2_2^-$	0.10(6)	—	—
	1403		$7/2_1^-$	0.85(15)	—	—
	2273		$5/2_1^-$	0.05(1)	—	—
2699	<i>276</i>	$11/2_2^-$	$7/2_3^-$	n.o.	0.00	—
	<i>429</i>		$11/2_1^-$	n.o.	0.00	0.00
	696		$9/2_2^-$	0.20(1)	0.19	0.01
	1433		$9/2_1^-$	0.80(1)	0.44	0.00
	<i>1296</i>		$7/2_2^-$	n.o.	0.33	0.68
	<i>1701</i>		$7/2_1^-$	n.o.	0.04	0.30
2799	<i>100</i>	$13/2_1^-$	$11/2_2^-$	n.o.	0.00	0.00
	529		$11/2_1^-$	0.02(1)	0.00	0.00
	796		$9/2_2^-$	n.o.	0.00	0.00
	1531		$9/2_1^-$	0.98(1)	1.00	1.00
3244	1978	$11/2_1^+$	$9/2_1^-$	1.0	—	—
3336	937	$13/2_1^+$	$9/2_1^+$	0.85(7)	—	1.00
	1066		$11/2_1^-$	0.15(1)	—	—

Table 2. Continued.

E_x (keV)	E_γ (keV)	I_i^π	I_f^π	b_{exp}	b_{fp}	b_{fpg}
3461	<i>662</i>	$13/2_2^-$	$13/2_1^-$	n.o.	0.03	0.01
	<i>762</i>		$11/2_2^-$	n.o.	0.04	0.01
	<i>820</i>		$9/2_3^-$	n.o.	0.00	—
	<i>1191</i>		$11/2_1^-$	n.o.	0.00	0.00
	1458		$9/2_2^-$	0.55(2)	0.24	0.99
	2195		$9/2_1^-$	0.45(2)	0.69	0.00
3495(3)	<i>34</i>	$11/2_3^-$	$13/2_2^-$	n.o.	0.00	0.00
	<i>696</i>		$13/2_1^-$	n.o.	0.09	0.32
	<i>796</i>		$11/2_2^-$	n.o.	0.02	0.00
	<i>854</i>		$9/2_3^-$	n.o.	0.00	—
	<i>1079</i>		$7/2_3^-$	n.o.	0.00	—
	<i>1225</i>		$11/2_1^-$	n.o.	0.07	0.00
	<i>1492</i>		$9/2_2^-$	n.o.	0.11	—
	<i>2092</i>		$7/2_2^-$	n.o.	0.02	—
	2229(1)		$9/2_1^-$	1.0	0.59	—
	<i>2497</i>		$7/2_1^-$	n.o.	0.08	—
3844	<i>349</i>	$15/2_1^-$	$11/2_3^-$	n.o.	0.00	—
	<i>383</i>		$13/2_2^-$	n.o.	0.00	0.00
	1046		$13/2_1^-$	0.21(1)	0.16	0.00
	<i>1145</i>		$11/2_2^-$	n.o.	0.01	0.00
	1572		$11/2_1^-$	0.79(1)	0.83	1.0
4264	<i>928</i>	$15/2_1^+$	$13/2_1^+$	n.o.	—	0.00
	1019		$11/2_1^+$	0.16(1)	—	1.0
	1466		$13/2_1^-$	0.84(6)	—	—
4309(3)	<i>465</i>	$13/2_3^-$	$15/2_1^-$	n.o.	0.04	—
	<i>814</i>		$11/2_3^-$	n.o.	0.10	—
	<i>848</i>		$13/2_2^-$	n.o.	0.01	—
	<i>1510</i>		$13/2_1^-$	n.o.	0.08	—
	<i>1610</i>		$11/2_2^-$	n.o.	0.01	—
	<i>1668</i>		$9/2_3^-$	n.o.	0.20	—
	2039(1)		$11/2_1^-$	1.0	0.36	—
	<i>2306</i>		$9/2_2^-$	n.o.	0.17	—
	<i>3043</i>		$9/2_1^-$	n.o.	0.04	—
4415	<i>151</i>	$17/2_1^+$	$15/2_1^+$	n.o.	—	0.00
	1079		$13/2_1^+$	1.0	—	1.0
4644	<i>335</i>	$17/2_1^-$	$13/2_3^-$	n.o.	0.00	0.00
	<i>800</i>		$15/2_1^-$	n.o.	0.01	0.00
	<i>1183</i>		$13/2_2^-$	n.o.	0.03	0.00
	1847		$13/2_1^-$	1.0	0.95	1.0
4915(3)	<i>271</i>	$15/2_3^-$	$17/2_1^-$	n.o.	0.00	0.03
	<i>606</i>		$13/2_3^-$	n.o.	0.16	0.05
	<i>1071</i>		$15/2_1^-$	n.o.	0.04	0.00
	<i>1420</i>		$11/2_3^-$	n.o.	0.03	0.85
	<i>1454</i>		$13/2_2^-$	n.o.	0.01	0.00
	2116(1)		$13/2_1^-$	1.0	0.69	0.00
	<i>2216</i>		$11/2_2^-$	n.o.	0.04	0.01
	<i>2645</i>		$11/2_1^-$	n.o.	0.02	0.07
5195	<i>208</i>	$17/2_2^-$	$15/2_3^-$	n.o.	0.01	0.00
	<i>551</i>		$17/2_1^-$	n.o.	0.02	0.27
	<i>886</i>		$13/2_3^-$	n.o.	0.01	0.03
	<i>1351</i>		$15/2_1^-$	n.o.	0.08	0.01
	1733		$13/2_2^-$	1.0	0.64	0.06
	<i>2396</i>		$13/2_1^-$	n.o.	0.25	0.63

Table 2. Continued.

E_x (keV)	E_γ (keV)	I_i^π	I_f^π	b_{exp}	b_{fp}	b_{fpg}
5543	75	$19/2_1^-$	$17/2_3^-$	n.o.	0.00	0.00
	348		$17/2_2^-$	n.o.	0.00	0.00
	628		$15/2_3^-$	n.o.	0.00	0.00
	899		$17/2_1^-$	0.27(7)	0.09	0.00
	1698		$15/2_1^-$	0.73(7)	0.91	1.0
5552	908	$19/2_1^+$	$17/2_1^-$	0.19(2)	—	—
	1289		$15/2_1^+$	0.81(9)	—	1.0
6090	538	$21/2_1^+$	$19/2_1^+$	n.o.	—	0.00
	704		$17/2_2^+$	n.o.	—	0.00
	1675		$17/2_1^+$	1.0	—	1.0
7284	629	$21/2_1^-$	$19/2_2^-$	n.o.	—	0.00
	1733		$19/2_1^+$	0.24(8)	—	—
	1741		$19/2_1^-$	n.o.	—	0.00
	1816		$17/2_3^-$	n.o.	—	1.0
	2088		$17/2_2^-$	0.34(7)	—	0.00
	2639		$17/2_1^-$	0.42(20)	—	0.00
	7295		429	$23/2_1^+$	$21/2_2^+$	n.o.
575		$19/2_2^+$	n.o.		—	0.00
1205		$21/2_1^+$	n.o.		—	0.00
1743		$19/2_1^+$	1.0		—	1.0
7486	620	$25/2_1^+$	$21/2_2^+$	n.o.	—	0.00
	1396		$21/2_1^+$	1.0	—	1.0
7629	152	$23/2_1^-$	$21/2_2^-$	n.o.	—	0.00
	345		$21/2_1^-$	0.04(1)	—	0.02
	974		$19/2_2^-$	n.o.	—	0.98
	1538		$21/2_1^+$	0.96(12)	—	—
8879	2086	$25/2_1^-$	$19/2_1^-$	n.o.	—	0.00
	149		$23/2_2^-$	n.o.	—	0.00
	162		$21/2_3^-$	n.o.	—	0.00
	1250		$23/2_1^-$	n.o.	—	0.00
	1402		$21/2_2^-$	n.o.	—	0.00
	1595		$21/2_1^-$	1.0	—	1.0
9161	194	$27/2_1^-$	$25/2_3^-$	n.o.	—	0.00
	241		$25/2_2^-$	n.o.	—	0.00
	282		$25/2_1^-$	n.o.	—	0.00
	431		$23/2_2^-$	n.o.	—	0.00
	1532		$23/2_1^-$	0.61(14)	—	0.99
	1675		$25/2_1^+$	0.39(21)	—	—
10155	96	$31/2_1^-$	$29/2_1^-$	n.o.	—	0.00
	994		$27/2_1^-$	1.0	—	1.0

is the yrast 2270 keV $11/2^-$ level. Allowing all possible $\Delta I = 1$ and $\Delta I = 2$ transitions to states of lower energy results in four predicted transitions from the calculations. Of these only the 1273 keV and the 1005 keV transitions are experimentally observed and the branching ratios are determined as 0.73(3) and 0.27(3), respectively. Another example is the 756 keV $5/2^-$ yrare state, which experimentally decays via three well-known transitions (339, 632, 756 keV) and a tentative transition (667 keV). The four decays have observed branching ratios of 0.04(1), 0.05(1), 0.83(2), and 0.08(1), respectively. The calculation give the corresponding branching ratios as 0.05, 0.07, 0.88, and 0.00. The calculated results agree with the experimental

ones for all but the tentative transition which is not predicted by the calculation.

One interesting detail noticed only in the analysis of the electromagnetic decay properties is the difficulty in reproducing the branching ratios for the yrast and yrare $3/2^-$ levels in the fp calculation. As can be seen in table 2 there are relatively large discrepancies between the experimental and the calculated results, especially for the $7/2_1^- \rightarrow 3/2_1^-$ transition. Experimentally, this is determined as 0.26(2) but the calculated branching ratio is as low as 0.01. The distinct difference is very surprising, especially when compared with the very good agreement between experimental and calculated branching ratios for all other yrast levels.

If two predicted levels with the same spin and parity are placed close in energy, shell model calculations have problems in correctly describing their electromagnetic decay properties. The problem can usually be solved by afterwards mixing the wave functions of the two states based on the matrix elements of the electromagnetic operators. However, in the current experiment *and* calculation the two $3/2^-$ states are separated by over 400 keV. Considering the MLD value of 228 keV obtained for this calculation—about 50% of the energy difference between the two levels of interest—the two states should be well separated, yet these difficulties persist.

The analysis of the branching ratios may also be used to predict weak transitions and provides a possibility to suggest spin assignments to new levels. One example, where this method can be applied, is the experimental level found at 3495 keV, which decays into the $9/2^-$ level with a γ -ray of 2229 keV. Based on the R_{154-96} value of 1.40(12) this transition is most likely to be of $\Delta I = 2$ character, which hints towards a $13/2$ assignment to the 3495 keV level. Nevertheless, a mixed $\Delta I = 1$ transition cannot be ruled out. Theoretically, the $11/2_3^-$ and $13/2_3^-$ states are predicted at 3796 and 4519 keV. Using a $11/2_3^-$ assignment for the 3495 keV level, the main predicted decay branch (59%) corresponds to the observed 2229 keV γ -ray, while a $13/2_3^-$ at 3495 keV shall decay predominantly (47%) into the $13/2^-$ yrast state, which would be at variance with experiment. In conclusion, we tentatively associate the observed level at 3495 keV with the predicted $11/2_3^-$ state. In a similar way, the predicted $13/2_3^-$ and $15/2_3^-$ states are good candidates to explain the experimentally observed levels at 4309, and 4915 keV, respectively.

Comparing calculated and experimental energy levels, the $f_{5/2}pg_{9/2}$ calculation has already proven not to be equally reliable as the fp calculation. The study of the electromagnetic decay properties shows a similar trend and the values are also presented in table 2. This calculation provides predictions for positive- as well as negative-parity states, though it cannot predict any parity-changing $E1$ transitions. This is due to the fact that $\Delta I \geq 2$ for transitions between odd- ℓ ($2p_{3/2}$, $1f_{5/2}$, $2p_{1/2}$) and even- ℓ ($1g_{9/2}$) orbitals. Moreover, the $f_{5/2}pg_{9/2}$ calculation, due to the lack of the $1f_{7/2}$ orbital in the configuration space, underestimates the branching ratios of the

experimentally established parity-conserving $\Delta I = 1$ transitions. The difficulty originates from the K^2 -dependence of the $B(M1)$ strength (see, *e.g.*, eq. 4-87 in ref. [19]). Excluding the $1f_{7/2}$ orbit will reduce the maximum of this value by almost a factor two. The effect is strikingly seen in the calculated branching ratios of the 1005 and 1273 keV transitions from the 2270 keV $11/2_1^-$ level. As mentioned above, the fp calculation reproduces them with very good precision, while the $f_{5/2}pg_{9/2}$ calculation reduces the $\Delta I = 1$ part to negligible 1%, it amounts to 27(3)% experimentally.

Finally, the experimentally obtained spin and parity assignments of low-lying states based on ref. [3] and the current analysis affect the tentative spin assignments of the superdeformed (SD) band presented in ref. [8]. The SD band will, according to previous analysis, decay into the 6090 and 7629 keV levels in the normally deformed level scheme, which now have fixed spin and parity assignments of $21/2^+$ and $23/2^-$, respectively. In the following, we have to assume that the 1432 keV transition at the bottom of the SD band (cf. ref. [8]) belongs to the band, *i.e.*, that it has $E2$ character. As a result, spin and parity $I^\pi = 23/2^-$ is assigned to the SD band head at 11367 keV, different from the tentative $I = 25/2$ assignment in ref. [8]. The modification of the spin assignment also leads to a change of signature, α , of the SD band in ^{61}Zn . Subsequently, the change of signature from $\alpha = +1/2$ to $\alpha = -1/2$ affects the discussion in ref. [8] in terms of proton and neutron occupancies of the $1g_{9/2}$ orbital for the band.

From the previous paper it is known that the SD occupancies in ^{61}Zn are built on the configuration of the SD band in ^{60}Zn . In ^{60}Zn two protons and two neutrons in the $1g_{9/2}$ orbital form the “doubly-magic” SD core in the mass region [20], and the additional neutron in ^{61}Zn can then occupy the positive-parity, $\alpha = +1/2$ Nilsson orbital [431]3/2, or either of the signatures in the [310]1/2 and the [303]7/2 orbitals. The latter orbital is unlikely since both of the two signature partners would be energetically close and, furthermore, they would be strongly coupled via cross-over $M1$ transitions connecting the levels between the bands (*e.g.*, structure 8 in ref. [1]). Neither of this is seen in the experimental data of ref. [8]. This leaves three possible Nilsson orbitals, two with $\alpha = +1/2$ and one with $\alpha = -1/2$. While the Skyrme-Hartree-Fock calculations in ref. [8] seem to energetically favour the two $\alpha = +1/2$ structures, Cranked Nilsson-Strutinsky (CNS) calculations [21,22] with standard parametrisation [21] predict the three remaining possibilities to be energetically equivalent within the spin regime the SD states are fed. More experimental work is clearly required to confirm that the lowest (11367 keV) level belongs to the SD band and/or that the 1432 keV γ -ray transition has $E2$ character and whether or not more bands exist in the second minimum of ^{61}Zn .

6 Summary

The current analysis of ^{61}Zn provides a firm, extended

decay scheme involving almost 70 transitions with spins ranging up to $I^\pi = 31/2^-$. The experimentally obtained energy levels and branching ratios have been compared with predictions from large-scale shell model calculations involving the upper fp shell and either the $1f_{7/2}$ or the $1g_{9/2}$ orbital. The predictions prove to be in good agreement with the experimental results but neither is adequate to fully describe ^{61}Zn . With its well-known decay pattern and because it is placed in the middle of the upper fp shell ^{61}Zn , provides a good starting point for further developments of the shell model calculations.

The revised spin assignment of the SD band requires a modified analysis in terms of neutron and proton configurations and calls for further experimental investigations of the high-spin excitation scheme of the ^{61}Zn nucleus.

We would like to thank the staff and the accelerator crew at ORNL for the excellent support during the experiment and I. Ragnarsson for helpful discussions concerning the CNS calculations. Our gratitude also goes to E. Caurier for his help with and contribution to the shell model calculations. This research was supported in part by the Swedish Research Council and the U.S. DOE grant DE-AC05-000R22725.

References

1. C. Andreoiu *et al.*, Eur. Phys. J. A **14**, 317 (2002).
2. S.M. Vincent *et al.*, Phys. Rev. C **60**, 064308 (1999).
3. O. Izotova *et al.*, Phys. Rev. C **69**, 037303 (2004).
4. E. Caurier, G. Martínez-Pinedo, F. Nowacki, A. Poves, A.P. Zuker, Rev. Mod. Phys. **77**, 427 (2005).
5. L.-L. Andersson *et al.*, Phys. Rev. C **71**, 011303(R) (2005).
6. M.R. Bhat, Nucl. Data Sheets **88**, 417 (1999).
7. R.B. Schubank, J.A. Cameron, V.P. Janzen, Phys. Rev. C **40**, 2310 (1989).
8. C.-H. Yu *et al.*, Phys. Rev. C **60**, 031305 (1999).
9. www.phy.ornl.gov/hribf/equipment/clarion.
10. C.J. Gross *et al.*, Nucl. Instrum. Methods Phys. Res. A **450**, 12 (2000).
11. T. Yamazaki, At. Data Nucl. Data Tables **3**, 1 (1967).
12. E. Gueorguieva, M. Kaci, C. Schüick, A. Minkova, Ch. Vieu, J.J. Correia, J.S. Dionisio, Nucl. Instrum. Methods Phys. Res. A **474**, 132 (2001).
13. L.-L. Andersson, Licentiate thesis, Lund University, in preparation.
14. E. Caurier, Shell model code ANTOINE, IRES, Strasbourg (1989-2002).
15. E. Caurier, F. Nowacki, Acta Phys. Pol. **30**, 705 (1999).
16. M. Honma, T. Otsuka, B.A. Brown, T. Mizusaki, Phys. Rev. C **69**, 034335 (2004).
17. M. Honma, T. Otsuka, B.A. Brown, T. Mizusaki, Phys. Rev. C **65**, 061301 (2002).
18. E. Caurier, private communication.
19. A. Bohr, B. Mottelson, *Nuclear Structure*, Vol. **II**, ISBN 0-8053-1016-9 (v. 2) (1975).
20. C.E. Svensson *et al.*, Phys. Rev. Lett. **82**, 3400 (1999).
21. T. Bengtsson, I. Ragnarsson, Nucl. Phys. A **436**, 14 (1985).
22. A.V. Afanasjev, D.B. Fossan, G.J. Lane, I. Ragnarsson, Phys. Rep. **322**, 1 (1999).

